LOW ELEVATION TARGET DETECTION AND DIRECTION FINDING

A THESIS SUBMITTED TO
THE GRADUATE SCHOOL OF NATURAL AND APPLIED SCIENCES
OF
MIDDLE EAST TECHNICAL UNIVERSITY

BY

GÖRKEM UYAR

IN PARTIAL FULFILLMENT OF THE REQUIREMENTS
FOR
THE DEGREE OF MASTER OF SCIENCE
IN
ELECTRICAL AND ELECTRONICS ENGINEERING

JANUARY 2012

Approval of the thesis:

LOW ELEVATION TARGET DETECTION AND DIRECTION FINDING

submitted by **GÖRKEM UYAR** in partial fulfillment of the requirements for the degree of **Master of Science in Electrical and Electronics Engineering Department, Middle East Technical University** by,

Prof. Dr. Canan Özgen
Dean, Graduate School of **Natural and Applied Sciences**

Prof. Dr. İsmet Erkmen
Head of Department, **Electrical and Electronics Engineering**

Prof. Dr. Yalçın Tanık
Supervisor, **Electrical and Electronics Eng. Dept., METU**

Prof. Dr. Mustafa Kuzuoğlu
Co-supervisor, **Electrical and Electronics Eng. Dept, METU**

Examining Committee Members:

Prof. Dr. Sencer Koç
Electrical and Electronics Engineering Department, METU

Prof. Dr. Yalçın Tanık
Electrical and Electronics Engineering Department, METU

Prof. Dr. Mustafa Kuzuoğlu
Electrical and Electronics Engineering Department, METU

Assoc. Prof. Dr. Çağatay Candan
Electrical and Electronics Engineering Department, METU

Dr. Ülkü Doyuran
Lead Design Engineer, ASELSAN

Date:

I hereby declare that all information in this document has been obtained and presented in accordance with academic rules and ethical conduct. I also declare that, as required by these rules and conduct, I have fully cited and referenced all material and results that are not original to this work.

Name, Last Name: GÖRKEM UYAR

Signature :

ABSTRACT

LOW ELEVATION TARGET DETECTION AND DIRECTION FINDING

Uyar, Görkem
M.Sc., Department of Electrical and Electronics Engineering
Supervisor : Prof. Dr. Yalçın Tanık
Co-Supervisor : Prof. Dr. Mustafa Kuzuoğlu

January 2012, 79 pages

Ground based radars often experience difficulties in target detection and direction finding (DF) applications due to the interference between the direct and surface reflected signals when the targets fly at low altitudes. In this thesis, the phenomena governing the low angle propagation are overviewed and a multipath signal model including the effects of refraction, specular reflection, diffuse reflection, curvature of the earth and antenna polarization is presented. Then, the model is utilized to develop detection and DF algorithms for the targets at low altitudes.

The target detection algorithm aims to increase signal-to-noise ratio (SNR) to overcome the effects of signal fading caused by surface reflections. The algorithm is based on diversity combining and the combining weight vector is calculated by maximizing average value of SNR. The technique is compared with Maximum Ratio Combining (MRC) algorithm which is optimal in terms of SNR.

In direction finding, it is the height of the target that is explored since the target range information is obtained from the time delay. The target height is estimated by utilizing Maximum Likelihood Estimation (MLE). The performance of our algorithm is compared with that of the technique that is known in the literature as Refined Maximum Likelihood (RML).

Keywords: low altitude target, low angle, multipath, target detection, direction finding

ÖZ

ALÇAK İRTİFA HEDEF TESPİTİ VE YÖN BULMA

Uyar, Görkem
Yüksek Lisans, Elektrik ve Elektronik Mühendisliği Bölümü
Tez Yöneticisi : Prof. Dr. Yalçın Tanık
Ortak Tez Yöneticisi : Prof. Dr. Mustafa Kuzuoğlu

Ocak 2012, 79 sayfa

Yere konumlu radarlar, hedefler düşük irtifada uçtuğu zaman, direk ve yerden yansıyan sinyallerin girişimi nedeniyle hedef algılama ve yön bulma (YB) uygulamalarında sık sık zorluk yaşarlar. Bu tezde, düşük açılı yayılımı belirleyen olaylar özetlenmiştir, ve kırılmanın, ayna yansımasının, dağınık yansımanın, dünyanın yuvarlaklığının ve anten kutuplaşmasının etkilerini içeren bir çok-yollu sinyal modeli sunulmuştur. Ardından, model, alçaktan uçan hedefler için algılama ve YB algoritmaları geliştirilirken kullanılmıştır.

Hedef algılama algoritması yüzey yansımalarından kaynaklanan sinyal solma etkilerinin üstesinden gelmek için sinyalin-gürültüye oranı (SGO)'nı artırmayı hedeflemiştir. Algoritma, çesitliliği birleştirmeye dayanmaktadır ve birleştirme ağırlık vektörü, SGO' nun ortalama değerinin maksimize edilmesiyle hesaplanmıştır. Teknik, SNR açısından en uygun olan Maksimum Oran Birleştirme (MOB) algoritması ile karşılaştırılmıştır.

Yön bulmada, hedef uzaklık bilgisi gecikme süresi ile elde edildiği için bulunmaya çalışılan hedef yüksekliğidir. Hedef yüksekliği, Maksimum Olabilirlik Tahmini (MOT) kullanılarak tahmin edilmiştir. Algoritmanın performansı, literatürde Arıtılmış Maksimum Olabilirlik (AMO) olarak bilinen teknik ile karşılaştırılmıştır.

Anahtar Kelimeler: düşük irtifalı hedef, düşük açılı, çok-yollu, hedef algılama, yön bulma

To my family

ACKNOWLEDGMENTS

I would like to express my deepest gratitude to my supervisor Prof. Dr. Yalçın Tanık for his precious supervision, helpful guidance and frank encouragement at every level of this work.

I would like to express my thanks to Prof. Dr. Mustafa Kuzuoğlu for his precious support.

I would like to also thank to TÜBİTAK for their financial support during my thesis research.

Finally, I would like to thank my family for their infinite love and support. This thesis is dedicated to them.

TABLE OF CONTENTS

CHAPTERS

APPENDICES

LIST OF TABLES

TABLES

LIST OF FIGURES

FIGURES

CHAPTER 1

INTRODUCTION

1.1 Scope and Objective

When a ground based radar illuminates a low altitude target, the problem of multipath propagation arises. The problem is that the radar also receives returns reflected from the earth's surface in addition to the expected direct return from the target as it is seen in Fig. 1.1. The reflected energy consists of *the specular* and *the diffuse* components. The specular component is dominant when the reflecting surface is smooth. It is the result of mirror-like reflection and highly correlated with the direct component. When the surface is rough, both the specular and the diffuse components are observed and the diffuse component is the energy of the microwave signal which is scattered from the irregular surface at various angles in a random fashion. The total response at the receiver is the coherent summation of the direct and reflected signals. Therefore, depending on the phase difference between the direct and reflected signals, this interference fades or enhances the resultant echo energy at the receiver. The situation of strong destructive interference can result in missed detection in target detection applications. Furthermore, the reflected signal may also be treated as arriving at the radar antenna from an image target below the surface. The appearance of multiple targets, in addition to the fading, often produces large errors in direction finding (DF) of targets flying at low altitudes.

It is important to model the multipath environment to propose solutions for both target detection and finding target's direction at low elevations. In the utilized model, an array antenna system is assumed. The model accounts for the polarization of the antenna elements in the array, but the effects of sidelobes in the antenna patterns are excluded. Since the phase difference between the direct and reflected signals is crucial in determining the resultant echo

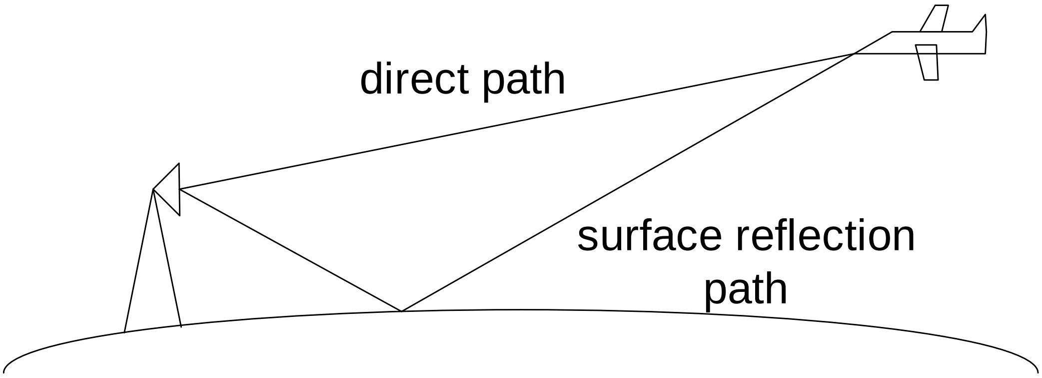

Figure 1.1: The multipath problem

energy at the receiver, the direct and reflected path lengths are formulated more accurately using the spherical earth model rather than through the more common planar earth model. The refraction is also included while calculating the path lengths by assuming a standard refraction gradient. Both the specular and the diffuse reflection coefficients are based on Beard [4]'s experiments. The specular reflection coefficient is assumed to be deterministic and its value is reduced with increasing roughness. The diffuse reflection coefficient is circularly symmetric complex Gaussian distributed. Its mean is zero and its standard deviation is determined by the surface roughness. The lossy reflection due to the curvature of the earth is accounted for by the divergence factor. The diffraction is not included in the model assuming that the target is in the interference region.

In target detection, our aim is to increase Signal-to-Noise-Ratio (SNR) of the receiver by combining the signals received by the elements of the array antenna system and hinder the missed detection due to fading caused by surface reflection. This is called *diversity combining*. In the literature, there are three major combining techniques [18, 19]:

1. *selection combining (SC)*,
2. *maximal ratio combining (MRC)* and
3. *equal gain combining (EGC)*.

In SC, the array element with the greatest SNR is chosen, the others do not contribute to the resulting SNR. This technique is clearly not the optimal solution since the other elements of the array are ignored. However, this combiner is the easiest in terms of required processing. It requires only a measurement of SNR at each element; the phase or the amplitude measurement are not needed [18, 19].

MRC yields the maximum output SNR among other techniques and is optimal in terms of SNR. The output SNR is the sum of SNR at each element. However, it requires accurate measurement of the amplitude and phase to obtain the weights maximizing the output SNR. Also, the magnitude of the weights may fluctuate over several 10s of dB due to fading [18, 19].

EGC overcomes this problem by setting gain of each weight to unity. Therefore, this technique eliminates the need of amplitude measurement and requires only phase measurement. Despite of that, EGC succeeds to achieve an improvement in SNR that is comparable to that of MRC which is optimal [18, 19].

However, these methods require that the received noise-free signal vector is known to the receiver. In our scene, the target height which is one of the parameters determining the noise-free signal is unknown. Therefore, these methods are not applicable to our problem.

In this thesis, we assumed that the value of the target height is uniformly distributed over the range we are looking for the target. Then, we obtain only a single weight vector for all target height values by maximizing the expected value of SNR. Since MRC is optimal in terms of SNR, we compare our combiner at various scenarios with MRC which finds different weight vectors for every target height values. We observe that our combiner shows improvement in SNR that is generally comparable to that of the MRC. However, in some scenarios, it is seen that the deviation of the performance of our method from that of MRC becomes high. We solved this problem by splitting the range of target height values into subintervals and finding separate weight vectors for each subinterval.

In DF, the standard monopulse technique is widely used. The typical monopulse radar processor compares the signals received by the antenna through the sum and difference channels and moves the boresight null upward or downward accordingly. In the closed loop system, the radar directs the boresight null at the target when it reaches the equilibrium. However, when the reflected ray enters the lower main lobe of the difference pattern as seen in Fig. 1.2, this leads to an error signal in the closed loop which drives the boresight axis off target. Depending on the relative phase of this reflected signal, the target can be pointed either above or below the true target direction. Therefore, when more than a single plane wave arrive simultaneously from nearly same directions, as it is in our situation due to the low-angle reflection, large errors can arise for standard monopulse technique [24, 25, 26, 31].

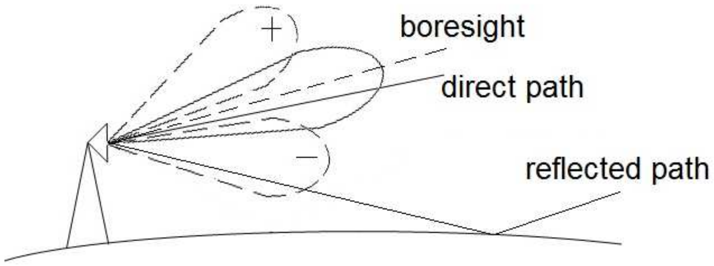

Figure 1.2: The standard monopulse system

Other than the standard monopulse, the techniques proposed to deal with the low-angle DF problem can be separated into three main families [26, 30]:

1. *enhanced monopulse techniques*,
2. *wave number estimation techniques*,
3. *a variety of Maximum Likelihood Estimation (MLE) techniques*.

Two well-known improved monopulse systems are the double-null technique [38] and the complex indicated angle technique [39]. The double-null technique, like the standard monopulse technique, has a main null directed at the target. Its difference from the standard monopulse technique is that it obtains a second auxiliary null in the direction of reflection path. The main approach of the other technique of complex indicated angle is the usage of the component of the difference signal that is in phase quadrature with the sum signal in addition to the in phase component. On the other hand, the conventional monopulse technique uses only the in phase component. The complex indicated angle combines the two components in a quantity named complex indicated angle. These enhanced monopulse techniques do not require a complex antenna system, therefore, are more economical than other techniques. However, these methods suffer from the rough surface reflection and the diffuse multipath [26, 30, 6].

The wave number estimation techniques exploit a phased array architecture. They form a covariance matrix whose terms consist of estimates of the correlation between the signals at the elements of an array antenna and are based on the decomposition of this covariance matrix. However, these techniques, for example multiple signal classification (MUSIC) [40], perform poorly for low elevation targets since the highly correlated nature of the direct and reflected signals causes the covariance matrix to become ill-conditioned [31, 26, 29, 30].

The last group comprises a variety of Maximum Likelihood Estimation (MLE) techniques. In MLE approach, a particular likelihood function is generated for the given radar data and the desired parameters, such as angles-of-arrivals (AOAs), are estimated by maximizing the likelihood function. In general, these algorithms usually offer better performance for low-angle DF since they are much less sensitive to signal coherence [31, 30]. Therefore, in this thesis, the MLE is chosen for DF of the low altitude targets.

The use of MLE for angle of arrival estimation has been studied in a large number of papers. Some of the principal studies are [32, 38, 36, 33, 34] and [35]. However, [37] concluded that these different approaches are in fact equivalent. All of MLE implementation proposed in [32, 38, 36, 33, 34] use the AOA model. The AOA model includes the direct and reflected signals by two superimposed plane waves having unknown AOAs, unknown amplitudes and unknown phases yielding six parameters which must be estimated. The unknown amplitudes and phases can be eliminated mathematically in the preliminary operations for maximizing the likelihood function, therefore, a two-dimensional search over two unknown AOAs is then implemented to maximize the likelihood function.

A better model called ”refined model” (RM) is used while calculating the likelihood function in [26, 27, 28] leading to a refined maximum likelihood (RML) technique. Here, ’refined’ refers to the use of a priori information of target range, radar height and surface roughness. In addition, only specular reflection is considered and the specular reflection coefficient is modeled as a steady and nonfluctuating parameter whose value is reduced according to the surface roughness. In RM, geometric information combined with a prior knowledge allows to represent the four unknowns of amplitudes and phases of direct and reflected signals by two unknowns of an amplitude and a phase. Also, since the target range is a priori information, the two unknowns of the AOAs of direct and reflected signals can be derived from the target height by utilizing the geometric information. Therefore, the six unknowns in AOA model reduces to three unknowns in RM: a signal amplitude, a signal phase and the target height. In RML, the unknown amplitude and phase are eliminated mathematically in the preliminary operations for maximizing the likelihood function and a one-dimensional search over the target height is executed. The use of the priori information has a beneficial effect on precision and results in a lower variance in target height estimation compared with that of the AOA model [26, 27]. Moreover, reduced number of unknowns significantly reduces the computational load. However, since the separation of the radar antenna and its image is many wavelengths, a height ambiguity problem arises in RML. This problem can be solved by using an array radar with sufficient bandwidth and at least two different frequencies [26, 27, 28].

Another model is introduced in [26]. In this model, a quadrature correction term is added to RML to account for the diffuse reflection and therefore, it is named QRML. In [26], it is demonstrated by computer simulations and experimental results that the RML algorithm works better than the QRML algorithm for both smooth and rough surfaces and gives better accuracy compared to QRML. In addition, QRML shows much greater sensitivity to calibration errors in comparison with RML. Therefore, in this thesis, we have chosen RML algorithm to compare with the MLE method we proposed for target height estimation.

In this thesis, we included the diffuse multipath in addition to the specular multipath while estimating the target height with MLE and named the algorithm as RML with Diffuse (RML-D). Then, we compared the performance of our implementation with the performance of the RML by using simulations.

1.2 Outline of the Thesis

The thesis is organized as follows:

- Chapter 2 describes the low-angle propagation and puts forward the model that is used in the simulations of detection and DF algorithms.
- Chapter 3 explains the SNR increment method we proposed and presents the comparison between the proposed method and MRC via simulations.
- Chapter 4 explains RML-D algorithm we proposed and compares it with RML algorithm by utilizing simulations.
- Chapter 5 presents general conclusions drawn from this work and some future work proposals.

We use the following notation: matrices are represented by bold upper-case letters, vectors by bold lower-case letter, scalars by both upper and lower italic letters. The superscripts, *,^{T} ,^{H} , $\|\ \|$ denote conjugation, transposition, conjugate transposition, and vector norm, respectively. Also, $\mathbf{C}^{MxN}$ signifies an M x N complex matrix.

CHAPTER 2

MULTIPATH SIGNAL MODEL

Our propagation model depicted in Fig. 2.1 can be classified as SIMO (Single Input Multiple Output) since there is a transmitting antenna sending the radio waves and a vertically distributed antenna array receiving the echo energy. The antenna array is formed by identical elements. Our scenario is that a ground based radar illuminates a low altitude target. Due to the target being at low altitudes, a direct path, rd, and an indirect path, $r1+r2$, produced by the earth surface reflection exist between the radar and the target for one-way propagation. However, as seen in Fig. 2.1, the propagation is two-way and this means that four distinct paths occur from the transmitter antenna to the target and back to the m^{th} element of the receiver array:

1. radar to target through rd_{tr} and target to radar through rd_m,
2. radar to target through rd_{tr} and target to radar via reflection through $r2_m$ and $r1_m$,
3. radar to target via reflection through $r1_{tr}$ and $r2_{tr}$ and target to radar through rd_m,
4. radar to target via reflection through $r1_{tr}$ and $r2_{tr}$ and target to radar via reflection through $r2_m$ and $r1_m$.

In our model, due to low-angle propagation:

- *The grazing angle*, ψ, that the incident ray makes with the horizontal reflecting surface is low. Therefore, the effects of *the antenna pattern* are not taken into account due to the small angles compared with a beamwidth.

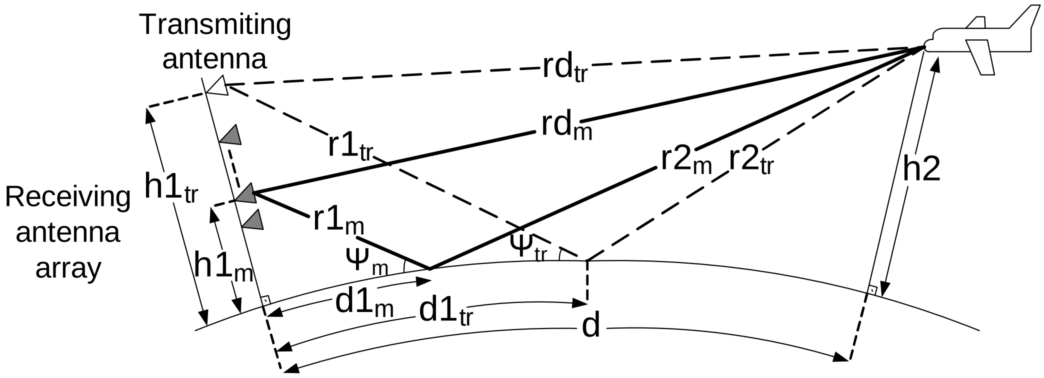

Figure 2.1: The array antenna configuration in the presence of multipath

- The group delay difference between the direct and reflected components are neglected and the signals reflected from the target are assumed to arrive at the antennas at the same time.
- The difference between the Doppler shifts of direct and reflected components are neglected.
- The propagation losses experienced by the direct and reflected components are assumed to be identical.

Generally, the radar cross section (RCS) of the target depends on both the target shape and its orientation. Since both are unknown here, it is assumed that isotropic scattering occurs from the target (point target).

As a result, assuming that the target is located at such a distance from the receiving antenna that the arriving waves can be considered as being planar, the vector superposition of four waves arriving at the m^{th} element of the array without noise can be expressed by

$$
\begin{aligned}
v_m = & \left[exp\{-j\,k\,rd_{tr}\} + \rho\, exp\{-j\,k\,(r1_{tr} + r2_{tr})\}\right] \times \\
& \left[exp\{-j\,k\,rd_m\} + \rho\, exp\{-j\,k\,(r1_m + r2_m)\}\right]
\end{aligned}
\tag{2.1}
$$

where k is *the wave number* and is given by

$$
k = \frac{2\pi}{\lambda}, \tag{2.2}
$$

and ρ is *the reflection coefficient*.

If the number of array elements is defined as M, the noise free observation vector, $\mathbf{v}$, is a column vector of length M and is given by

$$\mathbf{v} = \begin{pmatrix} v_1 \\ v_2 \\ \vdots \\ v_M \end{pmatrix}. \tag{2.3}$$

The noise free observation vector, $\mathbf{v}$, can be calculated with the use of matrix, $\mathbf{A}$, which is M-by-2 and is given by

$$\mathbf{A} = \begin{pmatrix} exp\{-jk\,rd_1\} & \rho\, exp\{-jk\,(r1_1 + r2_1)\} \\ exp\{-jk\,rd_2\} & \rho\, exp\{-jk\,(r1_2 + r2_2)\} \\ \vdots & \vdots \\ exp\{-jk\,rd_M\} & \rho\, exp\{-jk\,(r1_M + r2_M)\} \end{pmatrix}. \tag{2.4}$$

Then, the noise free observation vector, $\mathbf{v}$, is calculated in terms of $\mathbf{A}$ as

$$\mathbf{v} = \mathbf{A} \begin{pmatrix} 1 & 1 \\ 1 & 1 \end{pmatrix} \begin{pmatrix} exp\{-jk\,rd_{tr}\} \\ \rho\, exp\{-jk\,(r1_{tr} + r2_{tr})\} \end{pmatrix}. \tag{2.5}$$

As a result, the total observation vector, $\mathbf{s}$, is represented as

$$\mathbf{s} = \mathbf{v} + \mathbf{n} \tag{2.6}$$

Here, it is assumed that the additive noise vector, $\mathbf{n}$, has components that are zero-mean, circularly symmetric complex Gaussian, independent but assumed to be distributed identically with same variances, σ_n^2.

As can be observed from Eq. 2.1, the accuracy in determining the lengths of direct path, rd, and reflected path, $r1 + r2$, is critical. The curvature of the signal path due to *the refraction* in the troposphere in addition to the curvature of the earth must be considered while calculating these path lengths. *The reflection* is another factor affecting low angle propagation as Eq. 2.1 indicates. Therefore, in Sec. 2.1 and in Sec. 2.2, the refraction and the reflection phenomena will be discussed and, the path lengths and the reflection coefficient will be formulated. *The diffraction* also affects the low angle propagation, however, it is neglected in our model as discussed in Sec. 2.3.

2.1 The Refraction

The term refraction indicates the property of a medium to bend an electromagnetic wave as it passes through the medium. The refraction relies on the variations of the *refractive index*, n, and the value of n for the atmosphere near the Earth's surface varies generally between 1.00025 and 1.00040. Since the index of refraction is not a convenient number for studies of propagation, *refractivity*, N, has been defined by scaling n. The relationship between the refractive index, n, and the refractivity, N, is given as [1, 2]

$$n = 1 + N \times 10^{-6}. \tag{2.7}$$

Thus, the refractivity of the atmosphere near the surface of the earth generally varies between 250 and 400 N units.

The refractivity, N, is a function of the *atmospheric pressure* P (millibars), the *temperature* T (Kelvin) and the *partial pressure of water vapor* e (millibars) ,and is given by the following equation [1, 2]

$$N = 77.6\,(P/T) + 3.73 \times 10^{5}\,(e/T^{2}). \tag{2.8}$$

The quantities P and T can be measured directly, however, e is generally obtained indirectly. First, the relative humidity is measured and then, the measured quantity is converted to the water vapor content, e, by utilizing the *saturated vapor pressure*. The saturated vapor pressure is the quantity that governs the behavior of water vapor content, e. It is a kind of upper limit for e and is directly proportional with the temperature. Therefore, the relative humidity has nearly no influence on the radio refractivity for cold air as observed in Fig. 2.2 since the saturated vapor pressure is low. But for warm air, the saturated vapor pressure is high, therefore, the relative humidity has a strong effect on the value of N. In other words, it is seen that the water vapor component of refractivity increases exponentially with rising temperature for high values of relative humidity, however, the contribution of e to N is nearly zero when the temperature is low independent of the amount of relative humidity [1].

The temporal variations of the environmental conditions occur on relatively large time scales (hours, days, etc.) while in many radar applications the observations take place on smaller time scales (minutes, seconds, etc.). Therefore, the temporal stability of refractivity can be

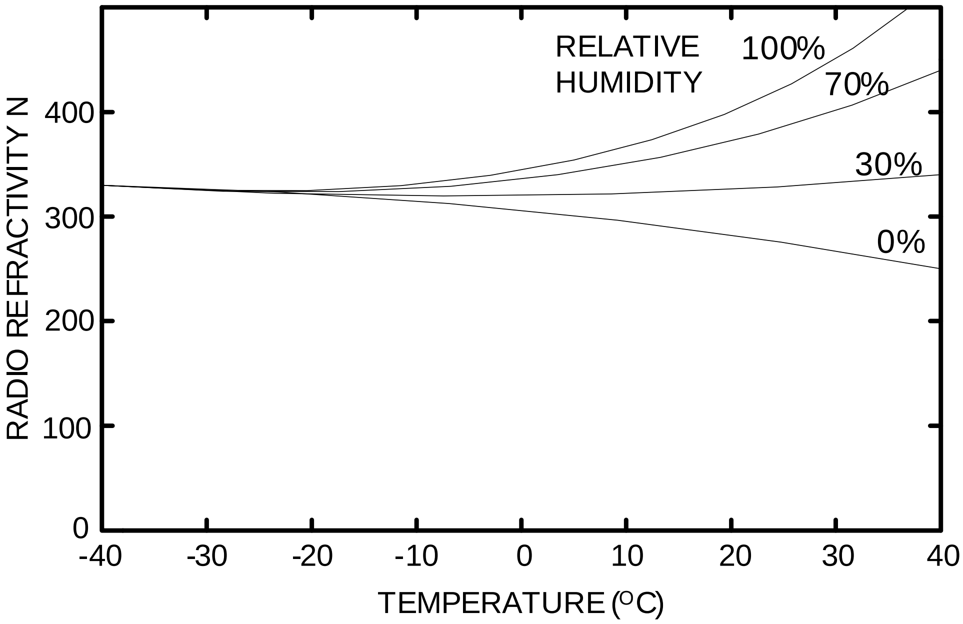

Figure 2.2: The variation of radio refractivity of air with temperature at an atmospheric pressure for four values of relative humidity

assumed and N can be considered to be constant during a sensor's coherent processing interval (CPI). Moreover, the refractivity generally varies larger with altitude than range. In most cases, the range variation of N can be neglected and the spatial variation of N can be assumed to be only in vertical direction [1, 21]. Therefore, the altitude variation of the pressure, P, the temperature, T, and the water vapor content, e, determines the refractivity profile of the atmosphere.

If the atmosphere is well mixed and stable, then the variation in P and T can be conveniently expressed with height. When the variation of refractivity with height in well mixed atmosphere for several values of specific humidity is examined, it is observed that the refractivity decreases with increasing altitude and the slope, dN/dh, known as the *refractivity gradient*, is constant for all humidity values as shown in Fig. 2.3. In practice, refractivity vs. height curves are not quite straight lines, but refractivity varies exponentially with altitude. However, low-altitude (up to 1-2 km) variation of N can be assumed to be linear [1, 2, 21].

Since the refractivity N decreases with elevation, the effect of refraction will be to bend horizontal rays downward as Snell's law predicts. It will have a *radius of curvature*, ξ, given by

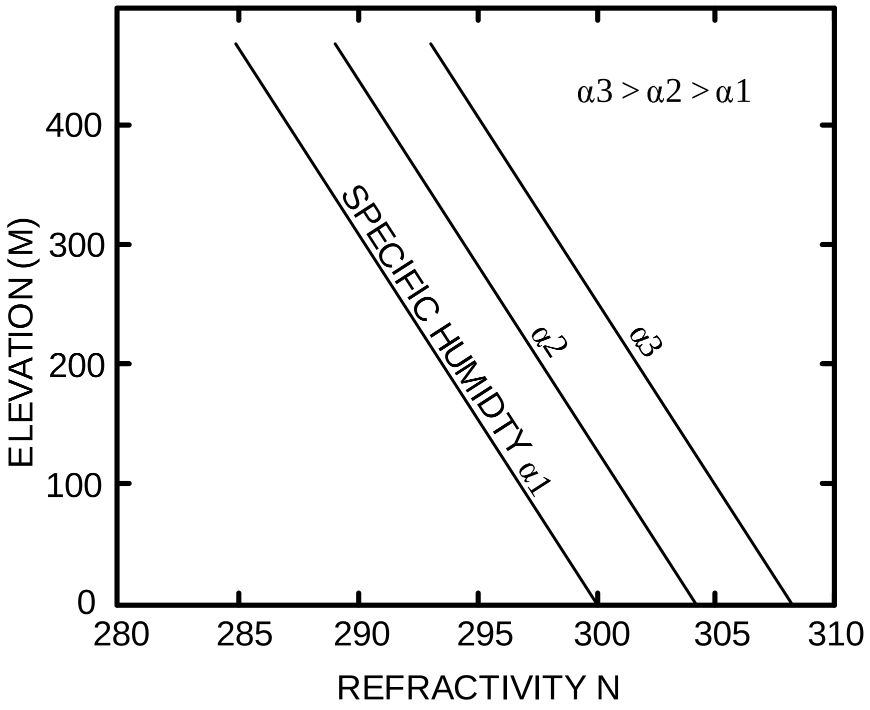

Figure 2.3: Refractivity N for values of specific humidity in a stable well-mixed atmosphere

[1]

$$\xi = \frac{n}{-\frac{dn}{dh} cos\psi}, \tag{2.9}$$

where ψ is the grazing angle and n is refractive index. Since $-dN/dh$ is nearly constant in a well-mixed atmosphere, $-dn/dh$ is constant from Eq. 2.7. n of air is very close to unity, typically 1.0003 (at sea level). Therefore, the radius of curvature, ξ, must be constant for the rays which satisfies $\cos\psi \approx 1$ (for the rays close enough to the horizontal). This allows us to apply a geometrical transformation to make it possible to represent the refracted rays as straight lines rather than curves. The actual radius of earth, $R_{earth}(\approx 6370km)$, is replaced by an equivalent radius, R_{eq}, given by

$$R_{eq} = K * R_{earth}, \tag{2.10}$$

where K is *the earth radius factor* and is given by [1, 31]

$$K = \left(1 + 10^{-6} R_{earth} \frac{dN}{dh}\right)^{-1}. \tag{2.11}$$

For a well mixed and stable atmosphere, the slope dN/dh is about -27 N/km and as a result of this, K is equal to 6/5 from Eq. 2.11. However, it is generally adopted to use $K = 4/3$ ($dN/dh \approx -39N/km$) as a standard working value. Therefore, the corresponding earth's equivalent radius is assumed to be $R_{eq} \approx 8500$ km [1, 2, 31, 20, 13, 21, 25, 23].

However, in practice, there are also cases in which the refractivity gradient is not constant. The pressure tends to be quickly restored to an equilibrium by winds, but the temperature inversions and humidity variations may occur and produce highly variable refractivity profiles. The refractivity gradients and their corresponding refractive conditions are shown in Fig. 2.4 [1, 2].

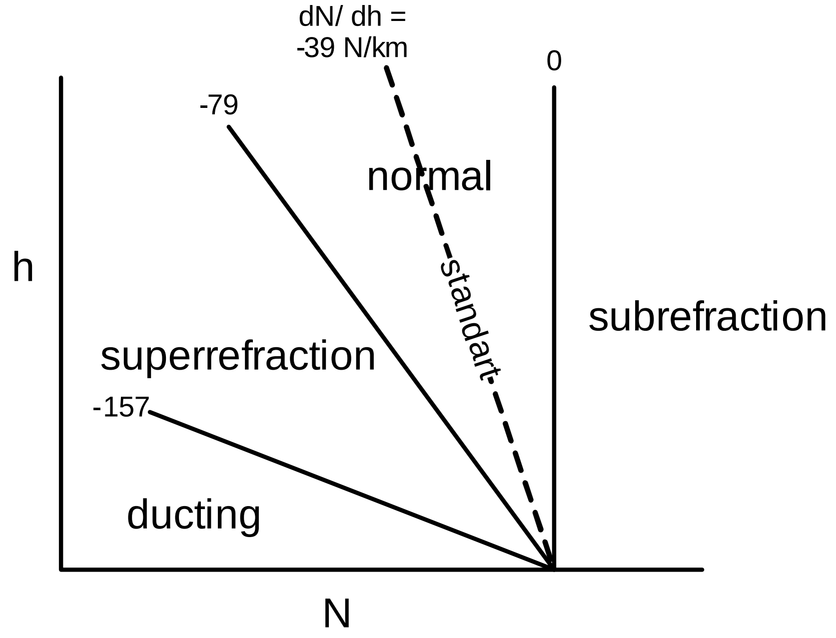

Figure 2.4: Refractivity gradients and associated conditions

The propagation in the refractive conditions of subrefraction, superrefraction and ducting is called the *anomalous propagation*. Trans-horizon and decreased horizon paths are caused by these nonstandard refractive conditions.

2.1.1 Normal/Standard Refraction

The constant refractivity gradient value of -39 N/km is the *standard gradient*. A standard gradient will make the waves bend downwards from a straight line as it is mentioned before.

Gradients that affect the propagation similar to the standard gradient but vary between 0 and -79 N/km are known as *normal gradients* [2].

2.1.2 Subrefraction

When the distribution of the temperature and the humidity in the atmosphere generates an increasing value of N with height, the propagating wave in this medium will be bent upward away from the earth. This is termed *subrefraction*. The subrefraction leads to the detection range to be reduced since the propagating energy decreases due to traveling away from the earth [2].

The situation of subrefraction occurs infrequently in nature[2].

2.1.3 Superrefraction

When the temperature, T, increases with height (temperature inversion) and/or the water vapor content,e, decreases rapidly with height, the refractivity gradient will decrease to a value below the normal refraction region. Therefore, the propagating waves will be bent downward more than normal. As the decrease in refractivity gradient keeps on, the radius of curvature of the wave will approach to the radius of curvature of the earth. The refractivity gradient at which these radius of curvatures are equal is called *critical gradient*. At critical gradient, the wave will travel at a fixed height above the earth. The refraction between the normal and critical gradients is referred to as the *superrefraction* [2].

This region is the transition region between normal and ducting gradients. Superrefraction has the same effect of bending the waves downward and increased detection range as normal refraction but superrefraction bends more than normal and the assumption of linear refractivity profile at low altitudes is not valid in superrefraction.

2.1.4 Ducting

In this case, the refractivity gradient reduces beyond the critical gradient. The propagating waves are bent downward with a radius smaller than the earth's. They may reach the earth's surface and undergo surface reflection. However, if the waves try to pass from a medium having comparatively high refractivity to the one with lower refractivity, they may be reflected from the boundary of the two media and they may reenter the area with high refractivity. This is what we call *ducting*. The wave is trapped to a narrow region of the atmosphere where the refractivity is high compared to the above and/or below layers, so the radiowaves propagate much further than normal. For the wave to couple into and remain in a duct, the angle of incidence to the duct made by the wave must be small, typically less than 1^o. Therefore, both the vertical distribution of refractivity and the geometrical relationship of the transmitter and the receiver to the duct must be considered in order to estimate the effect of the ducting at any particular frequency [1, 2].

The major causes of ducting are temperature inversions and humidity lapses. Ducts can occur either at ground level, *the surface ducts*, or be elevated, *the elevated ducts*. They can lead to extended radar detection ranges. Also, an air target would be missed if the radar signal is trapped into the duct and the target is just above the duct [2]. The wave propagation in a duct is illustrated in Fig. 2.5 [1, 2, 21].

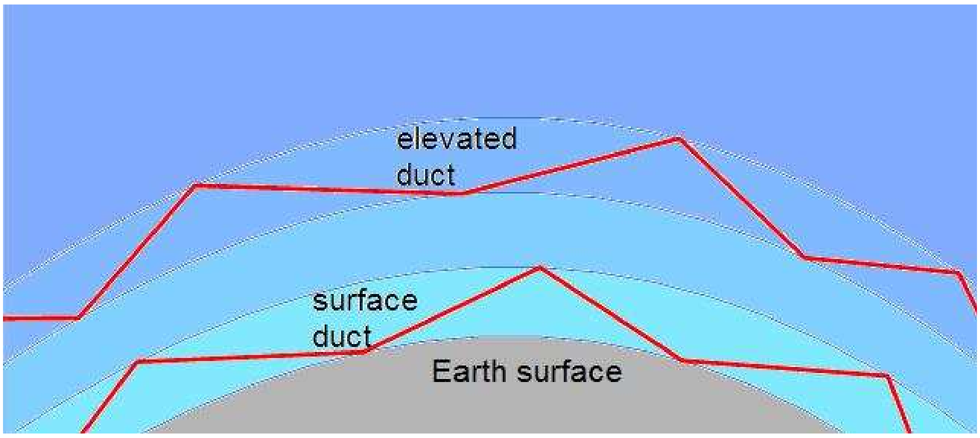

Figure 2.5: Surface and elevated ducts

In the case of ducting, the atmosphere is not well mixed and stable any more due to temperature and humidity variations, and the linear refractivity profile is not valid. Instead, the simple trilinear profile approximations shown in Fig. 2.6 can be used [2, 21].

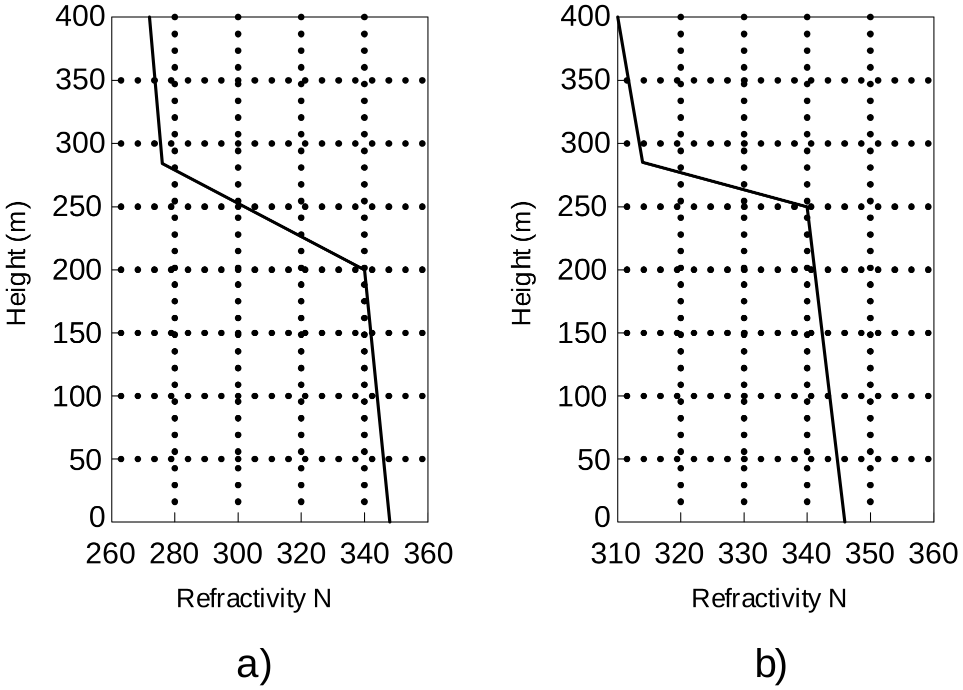

Figure 2.6: Simple refractivity profiles a)Surface duct b)Elevated duct

2.1.4.1 Surface Duct

The surface duct has its base at the Earth's surface. It is most commonly observed above the sea surface due to evaporation and this kind of surface duct has a specific name as *evaporation duct*. The evaporation at low altitudes leads to comparatively large values of humidity in a shallow layer near the sea surface and the evaporation duct is formed. From Fig. 2.2, it can be understood how this sharp increase in humidity may produce large values of N near the surface. Of course, for the humidity to play such an important role, the temperature must be high enough as mentioned before [1, 2, 21].

Surface duct can also be expected over land masses. The evaporation of the water on the ground after rain can lead to an over-land evaporation duct. Also, on clear nights over deserts or snow-covered terrain, when there is no wind to mix the air, radiational cooling at the surface can cause a strong temperature inversion near the ground. As a result of this, the surface duct can take place. However, ducting at the ground level over land is seldom encountered except over areas of desert or snow cover since both diffuse scattering and absorption by land surface tend to extract energy from the duct [1].

2.1.4.2 Elevated Duct

The meteorological conditions resulting in an elevated duct are the same as those for a surface duct. The only difference is that the elevated duct has its base above the Earth's surface. Elevated ducts may vary from a few hundred meters above the surface to several thousand meters [2].

The widely accepted procedure for characterizing the refractivity profile of the propagating medium is to use radiosonde measurements and estimate the change in refractivity between the ground and the altitude of propagation. Although this method does not give exact low altitude measurements, it gives some insight into the behavior of refractivity [1].

In our model, it is assumed that

- the atmosphere is well mixed and stable,
- therefore, the refractivity profile is linear and
- K is equal to 4/3.

Since K is equal to 4/3, $R_{eq} = 8500$ km is used as the earth radius to include the refraction effect while calculating the path lengths below. If a radar antenna, at an altitude $h1$, is separated from the target, at an altitude of $h2$, by a distance d above the spherical earth of equivalent radius R_{eq} (8500 km), the distance from the radar to the specular reflection point $d1$ is calculated by [13]

$$d1 = \frac{d}{2} + p\,cos\left(\frac{\Omega + \pi}{3}\right) \tag{2.12}$$

where

$$p = \frac{2}{\sqrt{3}}\sqrt{R_{eq}(h1 + h2) + \left(\frac{d}{2}\right)^2}. \tag{2.13}$$

$$\Omega = cos^{-1}\left[\frac{2R_{eq}(h1 - h2)\,d}{p^3}\right] \tag{2.14}$$

provided R_{eq} is much greater than d. The path lengths of direct and reflected rays are given as [13]

$$r1 = \left[R_{eq}^2 + (R_{eq} + h1)^2 - 2R_{eq}\,(R_{eq} + h1)\,cos\left(\frac{d1}{R_{eq}}\right)\right]^{1/2}. \tag{2.15}$$

$$r2 = \left[R_{eq}^2 + (R_{eq} + h2)^2 - 2R_{eq}\,(R_{eq} + h2)\,cos\left(\frac{d - d1}{R_{eq}} \right) \right]^{1/2} \tag{2.16}$$

$$rd = [r1^2 + r2^2 + 2r1\,r2\,cos(2\psi)]^{1/2} \tag{2.17}$$

where the grazing angle, ψ, is given by

$$\psi = cos^{-1}\left[\left(\frac{R_{eq} + h1}{r1} \right) sin\left(\frac{d1}{R_{eq}} \right) \right] \tag{2.18}$$

There are also the absorption effects of rain and atmospheric gases on propagation. However, they may not be included since measurable rainfall is observed less than 5% of the time except in coastal areas and absorption by atmospheric gases is negligible at frequencies below about 10 GHz in low altitude [1].

2.2 The Reflection

When the propagating wave reaches the ground, it undergoes surface reflection. The reflected energy consists of *the specular* and *the diffuse* components. When the surface is smooth, only the specular component exists. The specular component is highly correlated with the direct component and is usually referred to as the coherent part of the reflected signal. However, the Earth's surface is rough. In the case of rough surface reflection, the energy of the microwave signal which is not absorbed or reflected specularly will be scattered from the irregular surface at various angles in a random fashion. This is the diffuse component and is known as the incoherent part of the reflected signal. For simplicity, first, the reflection from smooth surface will be discussed, then the rough surface reflection will be explained.

The clutter is the backscattered radar signal. Since the clutter can essentially be eliminated with Doppler processing, only the forward scattering will be taken into account.

2.2.1 Reflection from Smooth Surfaces

Only the specular reflection exits and the point of reflection is called *smooth specular reflection point*. In specular reflection, the angle at which the wave is incident on the surface is equal to the angle at which it is reflected as seen in Fig. 2.7.

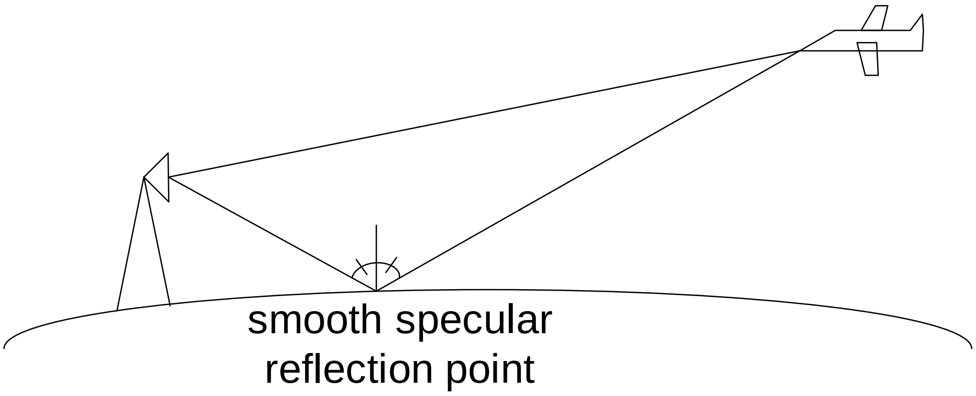

Figure 2.7: Smooth surface specular reflection

The smooth surface reflection coefficient, ρ_0, is given by [31, 21, 20, 13]

$$\rho_0 = \Gamma D. \tag{2.19}$$

where Γ is *the Fresnel reflection coefficient* and D is *the divergence factor*.

The divergence factor, D, is due to the earth's spherical surface. The parallel incident waves diverge after reflection since each has a slightly different angle of incidence. This divergence leads to the rays to be defocused and the power density to be reduced. The reduction in power density is accounted for by the divergence factor ($D \prec 1$) and it is given by

$$D = \frac{r1 + r2}{r1} \sqrt{\frac{\tau_1 \, \tau_2}{(\tau_1 + r2)(\tau_2 + r2)}} \tag{2.20}$$

where

$$\frac{1}{\tau_1} = \frac{1}{r1} + \frac{1}{\tau \, sin\psi} + \sqrt{\frac{1}{(\tau \, sin\psi)^2} - \frac{4}{R_{eq}^2}} \tag{2.21a}$$

$$\frac{1}{\tau_2} = \frac{1}{r1} + \frac{1}{\tau \, sin\psi} - \sqrt{\frac{1}{(\tau \, sin\psi)^2} - \frac{4}{R_{eq}^2}} \tag{2.21b}$$

$$\tau = \frac{R_{eq}}{1 + sin^2\psi}. \tag{2.21c}$$

The Fresnel reflection coefficient for vertical and horizontal polarizations are given respectively by

$$\Gamma_v = \frac{\epsilon_r \, sin\,\psi - \sqrt{\epsilon_r - cos^2\,\psi}}{\epsilon_r \, sin\,\psi + \sqrt{\epsilon_r - cos^2\,\psi}} \tag{2.22a}$$

$$\Gamma_h = \frac{sin\,\psi - \sqrt{\epsilon_r - cos^2\,\psi}}{sin\,\psi + \sqrt{\epsilon_r - cos^2\,\psi}} \tag{2.22b}$$

Here, ϵ_r is *the relative dielectric constant* of the surface and ψ is the grazing angle. The relative dielectric constant is the ratio of the dielectric constant of the surface material to the dielectric constant of a vacuum. It is a complex constant and represented by [1, 31]

$$\epsilon_r = \epsilon_{1r} - j\,\epsilon_{2r} \tag{2.23}$$

ϵ_{2r} indicates the loss in the material. When ϵ_{2r} is zero, it means that the material is lossless. It is given by [1, 31]

$$\epsilon_{2r} = 60\,\lambda\,\sigma \tag{2.24}$$

where λ is *the wavelength* and σ is *the conductivity.*

ϵ_{1r} and σ are both functions of frequency and temperature in general, and must be determined by laboratory measurements [1].

For soil, the major parameters determining the dielectric constant are moisture content and frequency. In Tab. 2.1, the values of ϵ_{1r} and ϵ_{2r} of soil at a representative set of frequencies for moisture contents from 0.3 to 30% by volume are given [1].

Table 2.1: Electromagnetic Properties of Soil

Frequency (GHz)	Moisture Content by Volume										
	0.3%			10%			20%			30%	
	ϵ_{1r}	ϵ_{2r}		ϵ_{1r}	ϵ_{2r}		ϵ_{1r}	ϵ_{2r}		ϵ_{1r}	ϵ_{2r}
0.3	2.9	0.071		6.0	0.45		10.5	0.75		16.7	1.2
3.0	2.9	0.027		6.0	0.40		10.5	1.1		16.7	2.0
8.0	2.8	0.032		5.8	0.87		10.3	2.5		15.3	4.1
14.0	2.8	0.035		5.6	1.14		9.4	3.7		12.6	6.3
24.0	2.6	0.030		4.9	1.15		7.7	4.8		9.6	8.5

For better understanding the behavior of the reflection coefficient, the frequency of 8.0 GHz is picked from the table 2.1 and, the magnitude and the phase of the Fresnel reflection coefficient with respect to grazing angle is drawn at specific moisture contents of soil for both vertical and horizontal polarizations in Fig. 2.8.

The electromagnetic properties of snow, ice and water are not the same as expected. The dielectric constant of snow depends on its density in addition to the frequency and temperature ,and the dielectric constant of ice is roughly equal to that of dry soil (desert). The dielectric

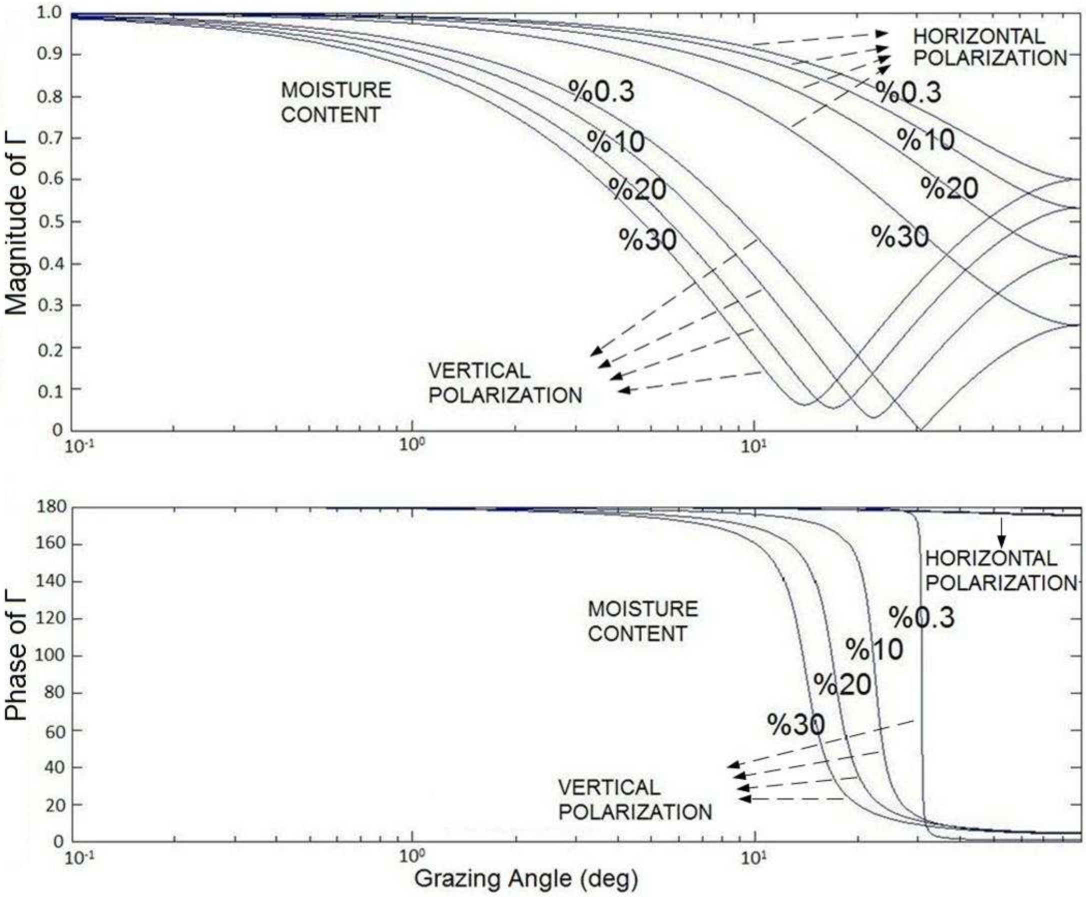

Figure 2.8: The magnitude and the phase of the Fresnel reflection coefficient as a function of grazing angle for different moisture contents at a frequency 8 GHz

properties of water depend on frequency, temperature and the impurity level. To sum up, the electromagnetic properties of different kinds of reflecting surfaces are different and they must be determined by laboratory measurements. However, the behavior of the reflection coefficient is similar for all of them. Therefore, the characteristics of the reflected waves can be summarized from Fig. 2.8 [1]

- The magnitude of the reflection coefficient for horizontal polarization is equal to 1 at very small grazing angles and diminishes monotonically as the grazing angle increases. On the other hand, the magnitude of the reflection coefficient has a single minimum for vertical polarization and the minimum value is equal to 0 provided $\sigma = 0$.

- The reflection coefficients for horizontal and vertical polarization at a grazing angle of

90^o are the same and equal to

$$\Gamma = \frac{1 - \sqrt{\epsilon_r}}{1 + \sqrt{\epsilon_r}} \tag{2.25}$$

- For horizontal polarization, the phase lag is nearly equal to π for all values of grazing angle (In Fig. 2.8, the phase lag lines for horizontal polarization as a function of grazing angle at the indicated moisture contents are drawn, but they are all nearly equal to π. The lines overlap and cannot be distinguished from each other in the figure.). However, for vertical polarization, the phase lag is equal to π at small grazing angles (for the grazing angles smaller than nearly 8^o) and goes to 0 at large grazing angles (for the grazing angles greater than nearly 45^o).

- For very low grazing angles (in the neighborhood of 1^o or less), the reflection coefficients for horizontal and vertical polarizations are equal, i.e., $\rho_h = \rho_v \approx 1$ and $\phi_h = \phi_v \approx \pi$. It means that the reflection properties will be similar for horizontal and vertical polarizations at very low grazing angles.

The reflection coefficient analysis so far assumed a smooth surface reflection, and can be used for ocean or lake surfaces with negligible wave disturbance, flat desert surfaces and snow-covered terrains. However, the ground is not smooth generally under realistic conditions, and the effect of the surface roughness must be taken into account.

2.2.2 Reflection from Rough Surfaces

In practice, the terrain can be considered as a large collection of scatterers distributed over the area. As a result of rough surface reflection from these scatterers, both specular and diffuse reflection take place as discussed before. Then, the reflection coefficient, ρ becomes

$$\rho = \rho_s + \rho_d, \tag{2.26}$$

where ρ_s is *the rough specular reflection coefficient* and ρ_d is *the rough diffuse reflection coefficient.* ρ in Eq. 2.26 is the reflection coefficient that is used in our model.

2.2.2.1 Rough Specular Reflection

The rough specular reflection mechanism from the scatterers over the area tends to concentrate energy about the smooth specular reflection point. However, the magnitude of the smooth surface reflection coefficient is reduced proportional to the surface roughness. Then, the rough specular reflection coefficient, ρ_s, becomes

$$\rho_s = \rho_0 R_s = \Gamma_{v,h} D R_s \tag{2.27}$$

where R_s is *the Root Mean Square (RMS) of the rough specular scattering coefficient*. The RMS value is used due to the randomness of the terrain.

Assuming that the rough surface is modeled as Gaussian, a simple model was developed by Ament [3] and R_s is given as [3]

$$R_s = exp\left[-8\pi^2\{\delta\}^2 \right] \tag{2.28}$$

where δ is *the roughness factor* and is given by

$$\delta = \frac{\sigma_h \, sin(\psi)}{\lambda} \tag{2.29}$$

Here, σ_h is *the standard deviation of the normally distributed surface heights* and is the only quantity representing the surface irregularity. λ is the electromagnetic wavelength and ψ is the grazing angle.

This model predicts a too rapid asymptotic decay in ρ_0. In 1961, larger experimental values of the coherent reflected field was found for roughness factor greater than 0.1 by Beard [4]. Therefore, the variations of Eq. 2.28 are used in the literature to improve this rapid decaying behavior [14, 15, 20, 31, 24]. An equation that best fits to the Beard's experiment was first obtained by Brown and Miller [10] in 1974 by adding a factor to the right side of Eq. 2.28 and is given by [10, 11, 12, 13]

$$R_s = exp\left[-8\pi^2\{\delta\}^2 \right] \times I_0 \left[8\pi^2\{\delta\}^2 \right], \tag{2.30}$$

where $I_0(z)$ is the modified Bessel function.

The behaviors of Eq. 2.28 and Eq. 2.30 are compared in Fig. 2.9.

As the RMS of the rough specular scattering coefficient, Eq. 2.30 is used in our model since it is the best in terms of fitting to the Beard's experimental results.

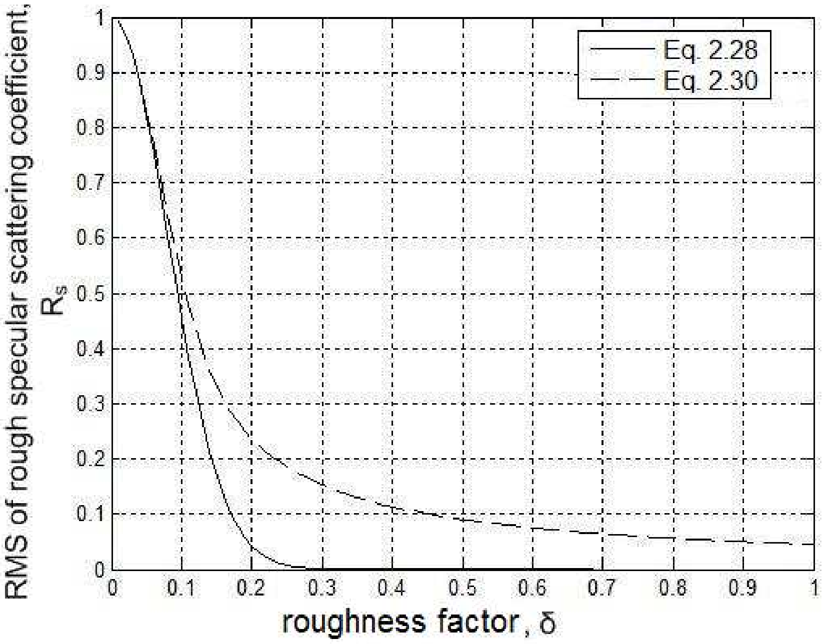

Figure 2.9: The behaviors of Eq. 2.28 and Eq. 2.30

2.2.2.2 Rough Diffuse Reflection

Prediction of the diffuse multipath component is difficult since no rigorous theory exits. In [16, 14, 21, 25, 17], the diffuse reflection is omitted and in [31, 20], the diffuse component is treated as noise and is combined with the receiver noise. Although there appears to be a shortage of data for evaluating the rough diffuse reflection, there are some existing, more detailed models representing the diffuse returns to the radar.

In 1961, Beard [4] has found that the incoherent field rises from zero and reaches a peak at the roughness factor ≈ 0.1. Then, it decreases gradually with increasing roughness factor further from 0.1. He also observed that most of the diffused power is peaked in the specular direction. The experimental data of Beard is used in the diffuse models in [24] and in [13]. According to these models, the amplitude of the diffuse reflection coefficient is expressed by a Rayleigh distributed probability function while its phase is uniformly distributed over $[0, 2\pi]$. That is what we also assume in our model. We also assumed that the diffuse power arrives at the receiver antenna from the specular direction with no spread in angle as Beard found in his experimental work.

The Rayleigh parameter, σ_d, in [24] is used since the Rayleigh parameter in [13] diminishes to zero after the roughness factor nearly 1.4 which is unrealistic. The Rayleigh parameter, σ_d, is given by [24]

$$\sigma_d = \begin{cases} \sqrt{2}\,3.68\,\delta, & 0 \leq \delta < 0.1 \\ \sqrt{2}\,(0.454 - 0.858\,\delta), & 0.1 \leq \delta < 0.5 \\ \sqrt{2}\,0.025, & 0.5 \leq \delta \end{cases} \tag{2.31}$$

This corresponds to *the rough diffuse scattering coefficient*, R_d, that is circularly symmetric complex Gaussian distributed and it is given by

$$R_d = R_{dx} + jR_{dy} \tag{2.32}$$

where $R_{dx} \sim N(0, \sigma_d^2)$ and $R_{dy} \sim N(0, \sigma_d^2)$, and they are independent.

Then, the rough diffuse reflection coefficient becomes

$$\rho_d = \rho_0\, R_d = \Gamma_{v,h}\, D\, R_d = \Gamma_{v,h}\, D\, (R_{dx} + jR_{dy}) \tag{2.33}$$

In Fig. 2.10, the magnitude of the RMS of the specular scattering coefficient and the mean of the magnitude of the diffuse scattering reflection coefficient can be observed. This plot is very close to what Beard [4] states.

Another model was developed by Beckmann and Spizzichino [5] in 1963. The model states that the rough surface consists of elementary mirrors (facets) and the slopes of the mirrors are described by any statistical distribution with maximum probability density at 0, and decreasing monotonously with increasing slope, β. Generally, normal distribution is used in the literature to define the slopes. The power can be reflected to the receiver from the region with facets having slope less than or equal to the rms slope of small surface facets, β_0. This region from where most of the diffuse power comes is defined as *the glistening surface*.

According to the glistening surface theory, the field formed by the diffuse scattering was entirely random and the diffuse scattering coefficient is found by integrating the contribution of a small element of the surface, dS, to the diffuse scattering coefficient over the glistening surface. The small element contribution is given by [5]

$$dp_d^2 = \left(\frac{R}{R_1 R_2}\right)^2 \frac{\sigma^0}{4\pi}\, dS \tag{2.34}$$

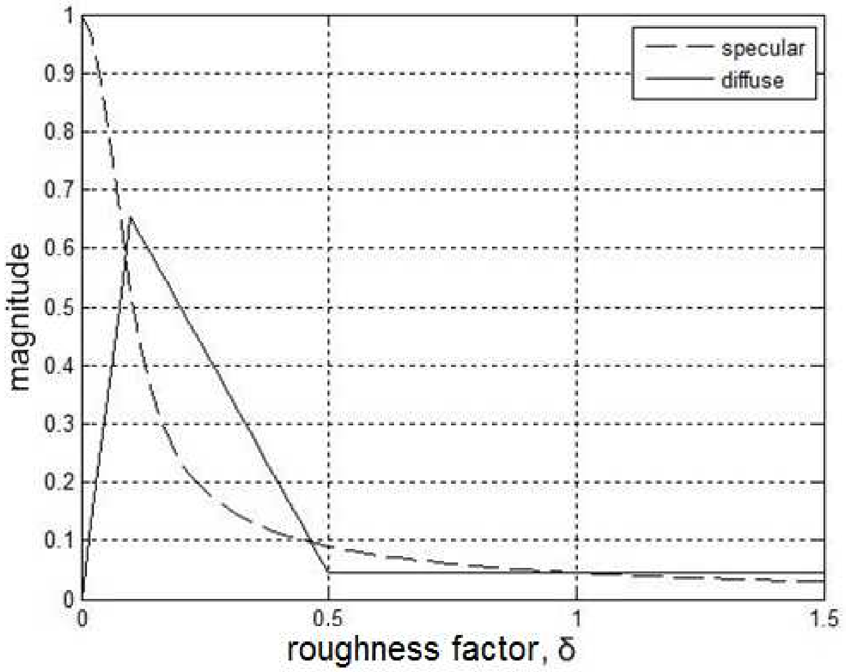

Figure 2.10: The magnitude of specular scattering coefficient and the mean of the magnitude of the diffuse scattering reflection coefficient

where R is the target range, R_1 and R_2 are the reflected field path lengths and σ^0 is *the bistatic scattering coefficient*.

However, in 1974, Barton [6] claimed that the incident power upon a diffuse facet was not entirely random and a portion of it will be scattered specularly. Therefore, he introduced additional weights, F_{d1} and F_{d2} to Eq. 2.34 to account for specular energy scattered by the diffuse facet. F_{d1} and F_{d2} depends on the local grazing angles from the radar antenna and the target, the wavelength and the standard deviation of the surface heights. In 1977, Barton [7] added another correction factor, Z, to address the problems of shadowing, multiple scattering and conservation of incident power. Then, the expression for the diffuse reflection contribution of a surface region dS with Gaussian distribution of slopes is given by

$$dp_d^2 = \left(\frac{R}{R_1 R_2}\right)^2 \frac{\sigma^0}{4\pi} F_{d1}\, F_{d2}\, Z\, dS \tag{2.35}$$

where the bistatic scattering coefficient, σ^0, for a normally distributed surface is given by [6, 7, 9]

$$\sigma^0 = \frac{1}{\beta_0^2}\, exp\Big(-\frac{\beta^2}{\beta_0^2}\Big). \tag{2.36}$$

Although the bistatic scattering coefficient, σ^0, is formulated by Barton in Eq. 2.36, the functional behavior of σ^0 is uncertain. Ideally, this behavior would be based on a combination of theory and experimental data, and, unfortunately, neither theory nor experimental data are adequate to do this [8]. Therefore, the diffuse model in our study will be based on Beard's [4] experiments.

In our model, the reflection coefficient, ρ, is assumed to be the same for every antenna element since they are very close to each other.

2.3 The Diffraction

Diffraction is the bending of waves around obstacles. It plays a significant role in the propagation of radio waves at low grazing angles over the ground. The geographical shapes like hills and ridges diffract energy into the shadow zone and provide radio communication and radar target detection within these zones. The diffraction can be classified into two groups: *diffraction by a knife-edge* and *diffraction by cylinders* [1].

2.3.1 Diffraction by a Knife-Edge

The geometry of the problem is illustrated in Fig. 2.11. As it can be seen, the propagation from T to R is affected by the knife-edge at O. In Fig. 2.11, d_T is the distance from transmitter to the knife-edge and d_R is the distance from the receiver (target) to the knife-edge. An important parameter is *the clearance*, Δ, the distance from O to TR.

When the clearance, Δ, is equal to the value of Δ_0 such that

$$\Delta_0 = \sqrt{\lambda\, d_T\, d_R/(d_T + d_R)} \tag{2.37}$$

then the path length TOR is longer than the direct path TR by an amount of $\lambda/2$.

By looking at *the normalized clearance*, Δ/Δ_0, for a given terrain profile, the effect of the diffraction can be estimated. In Fig. 2.12, the propagation over a knife-edge as a function of the normalized clearance is plotted. This figure is drawn roughly without any available data and only aimed to indicate the relationship between the normalized clearance and the diffraction.

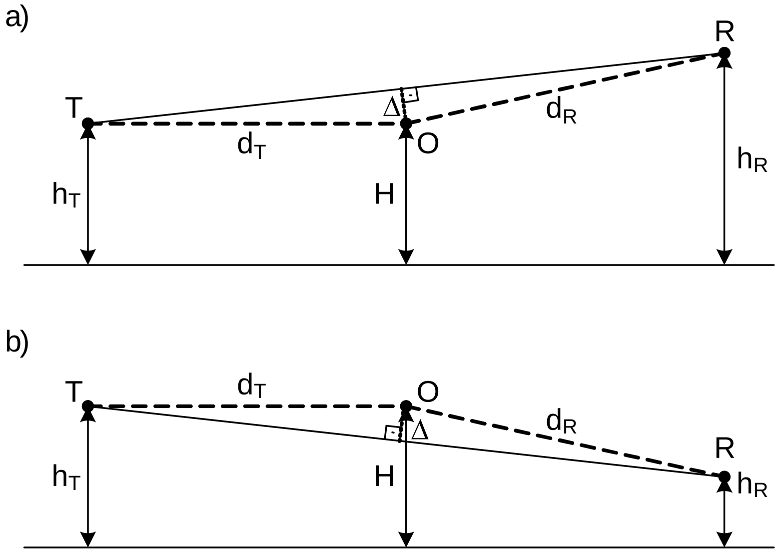

Figure 2.11: The geometry of the diffraction problem a) an example of positive clearance b) negative clearance

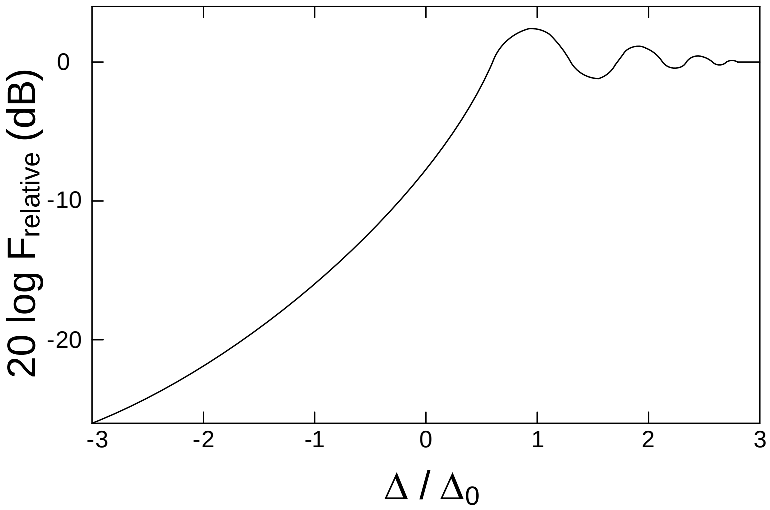

Figure 2.12: The propagation from T to R relative to free space propagation

As it can be observed from Fig. 2.12, the effect of the diffraction decreases with increasing normalized clearance. Therefore, in the design of the microwave links, the normalized clearance must be calculated carefully to include the effects of the diffraction properly. In [1], it is stated that the knife-edge diffraction can be neglected for the cases in which $\Delta/\Delta_0 \geq 0.6$.

2.3.2 Diffraction by Cylinders

In some situations, diffraction by a hill or ridge can be modeled more appropriately by the case of diffraction by a cylinder. In this case, a dimensionless parameter ζ is defined to characterize the effect of the finite radius of curvature of the cylinder. It is defined as [1]

$$\zeta = \left(\frac{\lambda\, r^2}{\pi}\right)^{1/6} \sqrt{\frac{d_T + d_R}{d_T\, d_R}} \tag{2.38}$$

where r is *the radius of the curvature* of the cylinder, and λ is the wavelength.

The diffraction loss varies with the radius of the curvature of the cylinder and the normalized clearance. The radius of the curvature $r = 0$ corresponds to the previous case of knife-edge diffraction [1].

The propagation over the spherical earth can be considered in three separate regions as shown in Fig. 2.13. The *diffraction region* is accepted as the region in the shadow well below the lowest line of sight and in this region, the diffraction effects must be included. The *interference region* includes almost all target locations where an unbroken line of sight exists between the radar antenna and the target except for the locations $\Delta/\Delta_0 < 0.6$. In this region, the diffraction is insignificant and can be neglected. The region between the interference and diffraction regions is the *intermediate region* [1].

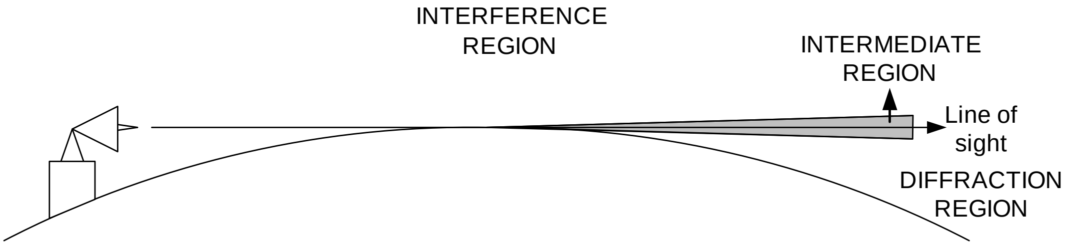

Figure 2.13: The propagation regions over the spherical earth

This thesis considers explicitly the interference region and neglects the effects of the diffraction.

CHAPTER 3

TARGET DETECTION

In Chapter 2, the arriving signals at each antenna element was modeled as in Eq. 2.1. In our model, M antennas receive different versions of the same signal and SNR they experience are different. Setting E$\{|n_m|^2\}$ to σ^2, we get the SNR at the m^{th} element to be

$$\gamma_m = \frac{|x_m|^2}{\sigma^2}. \tag{3.1}$$

Our goal here is to combine these samples as seen in Fig. 3.1 and improve the receiver system in terms of SNR. This is what we call *diversity combining* as we receive replicas of the same signal.

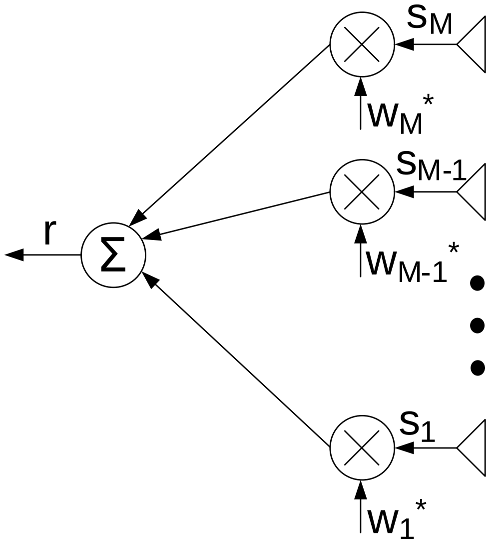

Figure 3.1: The diversity combining system

As seen from Fig. 3.1, the resultant signal, r, is

$$r = \mathbf{w^H} \mathbf{s} = \mathbf{w^H} \mathbf{v} + \mathbf{w^H} \mathbf{n} \tag{3.2}$$

and what we try to find is the weight vector, $\mathbf{w}$, maximizing the SNR of r.

There are some available methods in the literature: *the selection combining (SC)*, *the maximal ratio combining (MRC)* and *the equal gain combining (EGC)*. These combining techniques improve the SNR by calculating different weight vectors, $\mathbf{w}$, for every different noise-free vector, $\mathbf{v}$, assuming $\mathbf{v}$ is known to the receiver. However, the situation in our model is that the target height, $h2$, is the only unknown parameter assuming the target range information is obtained from time delay. The rough diffuse reflection coefficient, ρ_d, and RCS of the target are also unknown. However, the effects of the diffuse reflection and target RCS are omitted here, since the effects of the diffuse component on the detection performance is negligible [1] and isotropic scattering from the target is assumed in our model and thus RCS is deterministic. Since the target height is unknown, the noise-free vector, $\mathbf{v}$, is also unknown, therefore, these methods are not applicable to our model.

What we need is that to find a single weight vector, $\mathbf{w}$, for all $h2$ values we are interested in and obtain an SNR improvement performance that is comparable with MRC. We assume that $h2$ is a discrete random variable uniformly distributed over an interval. Then, we calculate a single weight vector, $\mathbf{w}$, by maximizing the average value of SNR of r over this interval of $h2$.

In the following sections, first, the three methods will be described in detail, then, the technique we proposed will be put forward. Finally, we will compare the performance of our method with MRC since it is optimal in terms of SNR when $\mathbf{v}$ is known. The comparison will be performed for various scenarios. Generally, our method is very close to the performance of MRC. However, in some scenarios, the deviation of the performance of our method from that of MRC increases. We solve this problem by splitting $h2$ range into subintervals and finding separate weight vectors for each subinterval.

3.1 Selection Combining

In this technique, the element with the greatest SNR is chosen. Therefore, the resultant SNR becomes

$$\gamma = max_m\{\gamma_m\}, \qquad m = 1, 2, ..., M \tag{3.3}$$

and

$$w_m = \begin{cases} 1 & \gamma_m = max_k\{\gamma_k\} \\ 0 & \text{otherwise} \end{cases}. \tag{3.4}$$

It is obvious that SC is not the optimal solution since the (M - 1) elements of the array are ignored.

3.2 Maximal Ratio Combining

Maximal Ratio Combining (MRC) determines the weight vector, **w**, that maximizes the output SNR and it is the optimal solution.

From Eq. 3.2, the SNR after beamforming becomes

$$\gamma = \frac{|\mathbf{w}^H\mathbf{v}|^2}{E\{|\mathbf{w}^H\mathbf{n}|^2\}}. \tag{3.5}$$

The noise power in the denominator is calculated as

$$\begin{aligned} P_n &= E\{|\mathbf{w}^H\mathbf{n}|^2\} = E\{|\mathbf{w}^H\mathbf{n}\mathbf{n}^H\mathbf{w}|\} = \mathbf{w}^H E\{|\mathbf{n}\mathbf{n}^H|\}\mathbf{w} \\ &= \sigma^2\, \mathbf{w}^H\, \mathbf{I}_M\, \mathbf{w} = \sigma^2\, \mathbf{w}^H\, \mathbf{w} = \sigma^2\, ||\mathbf{w}||^2, \end{aligned} \tag{3.6}$$

where $\mathbf{I}_M$ represents an MxM identity matrix. The weight vector, **w**, can always be scaled such that $||\mathbf{w}|| = 1$ since the filter gain is not important at all. Then, the resultant SNR becomes $\gamma = |\mathbf{w}^H\mathbf{v}|^2/\sigma^2$. By the Cauchy-Schwarz inequality, this has a maximum when **w** is linearly proportional to **v**, i.e.,

$$\mathbf{w} = \mathbf{v}. \tag{3.7}$$

Therefore, the resultant SNR is represented by

$$\gamma = \frac{|\mathbf{v}^H\mathbf{v}|^2}{\sigma^2\, \mathbf{v}^H\, \mathbf{v}} = \frac{\mathbf{v}^H\mathbf{v}}{\sigma^2} = \sum_{m=1}^{M} \frac{|v_m|^2}{\sigma^2} = \sum_{m=1}^{M} \gamma_m. \tag{3.8}$$

As the Eq. 3.8 indicates, the output SNR is the sum of the SNR at each element and MRC is optimal in terms of SNR.

3.3 Equal Gain Combining

The Equal Gain Combiner, as the name implies, uses the same magnitude for the weights, but only aligns the phases of the sensors. In the EGC,

$$\mathbf{w} = exp\{j\,\angle\mathbf{v}\}. \tag{3.9}$$

Therefore, the SNR after combining becomes

$$\gamma = \frac{|\mathbf{w}^H\mathbf{v}|^2}{\sigma^2\,\mathbf{w}^H\,\mathbf{w}} = \frac{1}{M}\,\frac{\sum_{m=1}^{M}|v_m|^2}{\sigma^2}, \tag{3.10}$$

which is the average of array sensor SNRs.

3.4 The Proposed Combiner

As discussed before, our aim is to find only one weight vector, **w**, by maximizing the average value of SNR over the $h2$ values we are interested in. Assume that $h2$ is uniformly distributed over these N number of values. Then, the average value of the SNR becomes

$$E\{\gamma\} = \frac{1}{N}\sum_{n=1}^{N}\frac{|\mathbf{w}^H\ \mathbf{v}(h2_n)|^2}{\sigma^2\,\mathbf{w}^H\,\mathbf{w}} = \frac{1}{N}\sum_{n=1}^{N}\frac{\mathbf{w}^H\ \mathbf{v}(h2_n)\ \mathbf{v}(h2_n)^H\ \mathbf{w}}{\sigma^2\,\mathbf{w}^H\,\mathbf{w}}. \tag{3.11}$$

Assume also that the weight vector, **w**, has the constraint of $||\mathbf{w}|| = 1$. Then, the average value of the SNR is

$$E\{\gamma\} = \frac{1}{N}\sum_{n=1}^{N}\frac{\mathbf{w}^H\ \mathbf{v}(h2_n)\ \mathbf{v}(h2_n)^H\ \mathbf{w}}{\sigma^2} = \frac{1}{N\,\sigma^2}\,\mathbf{w}^H\,\mathbf{V}\,\mathbf{w}, \tag{3.12}$$

where **V** is equal to

$$\mathbf{V} = \sum_{n=1}^{N}\mathbf{v}(h2_n)\ \mathbf{v}(h2_n)^H. \tag{3.13}$$

Hermitian matrix, **H**, is a square matrix with complex entries that is equal to its own conjugate transpose, i.e., $\mathbf{H} = \mathbf{H}^H$. It is obvious that the matrix, **V**, in Eq. 3.13 is hermitian. It is known that all eigenvalues of a hermitian matrix are real and an N-by-N hermitian matrix has N number of linearly independent eigenvectors. Moreover, it is possible to find an orthonormal basis of C^N consisting of N eigenvectors of this N-by-N hermitian matrix. Then, if the eigenvalues of **V** are $\lambda_1 > \lambda_2 > ... > \lambda_N$ and the corresponding orthonormal eigenvectors are $\mathbf{e_1}, \mathbf{e_2}, ..., \mathbf{e_N}$, the matrix, **V**, can be represented as

$$\mathbf{V} = \sum_{n=1}^{N}\lambda_n\,\mathbf{e_n}\,\mathbf{e_n}^H. \tag{3.14}$$

Moreover, since $[\mathbf{e_1}, \mathbf{e_2}, ..., \mathbf{e_N}]$ is an orthonormal basis of C^N, the weight vector, $\mathbf{w}$, can represented as

$$\mathbf{w} = \sum_{n=1}^{N} \alpha_n \, \mathbf{e_n}, \tag{3.15}$$

where $\alpha_n \leq 1$ for n = 1, 2, ... N since $||\mathbf{w}|| = 1$. By using Eq. 3.14 and 3.15, Eq. 3.12 showing the average value of SNR over $h2$ values becomes

$$E\{\gamma\} = \frac{1}{N\,\sigma^2} \sum_{l=1}^{N} \alpha_l^* \, \mathbf{e_l}^H \sum_{k=1}^{N} \lambda_k \, \mathbf{e_k} \, \mathbf{e_k}^H \sum_{n=1}^{N} \alpha_n \, \mathbf{e_n}. \tag{3.16}$$

Since the eigenvectors, $\mathbf{e_1}, \mathbf{e_2}, ..., \mathbf{e_N}$, are orthonormal,

$$\mathbf{e_k}^H \, \mathbf{e_n} = \begin{cases} 1 & , k = n \\ 0 & , \text{otherwise} \end{cases} . \tag{3.17}$$

Using Eq. 3.17, Eq. 3.16 becomes

$$E\{\gamma\} = \frac{1}{N\,\sigma^2} \sum_{n=1}^{N} \alpha_n^* \, \lambda_n \, \alpha_n. \tag{3.18}$$

This is maximum when

$$\alpha_n = \begin{cases} 1 & , n = 1 \\ 0 & , \text{otherwise} \end{cases} . \tag{3.19}$$

From Eq. 3.15 and Eq. 3.19, the weight vector, $\mathbf{w}$, is found to be

$$\mathbf{w} = \mathbf{e_1}, \tag{3.20}$$

which is the eigenvector of $\mathbf{V}$ having the largest eigenvalue.

As discussed before, the weight vector, $\mathbf{w}$, is calculated without including the diffuse reflection,i.e., $\rho_d = 0$, since the effect of the diffuse reflection on the detection performance is negligible [1].

3.5 Simulation Results

In this section, in all simulations, the center frequency, f, is 10 GHz, the height of the 1st antenna, $h1_1$, is 6 m and other antennas are placed with $\lambda/2$ spacing above the first antenna. All antennas are vertically polarized. The equivalent earth radius is 8500 km (K = 4/3) to account for atmospheric refraction. The electromagnetic properties of the ground are σ =

1e-3 S/m and $\epsilon_{1r} = 4$. The target height, $h2$, is assumed to be a discrete random variable and uniformly distributed over 40 m to 1000 m.

In Fig. 3.2 - 3.4, the target range, d, is set to 10 km and the standard deviation of normally distributed surface heights, σ_h, is set to 1.0 m ,and our combiner is compared with the MRC in terms of instantaneous SNR for different numbers of antennas. If there were no reflection, a straight line at 0 dB would be seen for the 1st antenna. This 0 dB line is the reference for all SNR figures below and the figures indicate the gain in SNR relative to this 0 dB line. As it can be seen in Fig. 3.2 - 3.4, the instantaneous SNR of the 1st antenna fades or enhances due to reflection. This is the main problem of low angle propagation we mentioned. Since the magnitude of the reflection coefficient decreases with increasing target height, the amplitude of the oscillations gets smaller as the target height is increased.

It can also be observed from Fig. 3.2 that when the number of antennas, M, is 5, the SNR gain achieved by MRC is 7 dB. This is what we expected since the MRC improves the SNR by the factor of number of antennas, M, and $10\log(M = 5)$ is nearly equal to 7. It is seen that the performance of our combiner is very close to the MRC for this case. In Fig. 3.3 and 3.4, the numbers of antennas are 10 and 20 respectively. In these figures, it is seen that the deviation of our combiner from the MRC increases with increasing the number of antenna elements in the receiver array and reaches to 3 dB for $M = 20$. This is what is expected since increasing the number of antenna elements means increasing the signals to be combined. The received signals by the added antenna elements differ more from that of the first antenna element since the antennas are added to the upper part of the array. So, the performance of the method which combines the signals with only one weight vector for all target height values deviates more from the performance of the MRC for larger number of antenna elements.

In Fig. 3.5, the average value of the SNR over mentioned target height values for the MRC and our combiner are compared for different number of antennas. It is seen that the average value of the SNR increases linearly with the number of the antenna elements in the receiver array for the MRC. Our average value maximization based combining method works also close to the MRC. However, it is again observed that as the number of antenna elements increases, the deviation of our combiner from the MRC increases.

In Fig. 3.6 - 3.8, the number of antennas, M, is set to 20 and the standard deviation of normally distributed surface heights, σ_h, is set to 1.0 m ,and our combiner is compared with the MRC in terms of the SNR for different target range, d, values. In Fig. 3.6, the target range, d, is 20 km and the performance of our combiner is very close to the MRC. In Fig. 3.7, the target range, d, is set to 10 km. In this case, the maximum deviation of our combiner from the MRC becomes nearly 3 dB. The maximum deviation increases to nearly 11 dB when the target range, d, is 5 km as seen in Fig. 3.8. Then, it is clear that the deviation of our combiner from MRC increases with the decreasing target range. This is due to the fact that the noise free vector, v, varies with target height more at smaller ranges and our combining method deviates from the MRC more at nearer regions.

In Fig. 3.9, the average SNR over mentioned target height values for the MRC and our combiner are compared for different target range values. In this figure, it is also seen that as the target range decreases, the deviation of our combiner from MRC increases.

In Fig. 3.10 - 3.13, the antenna number, M, is set to 20 and the target range, d, is set to 10 km, and our combiner is compared with the MRC in terms of the SNR for different standard deviation of normally distributed surface heights, σ_h, values. In Fig. 3.10, σ_h is 0.05 m and the amplitude of the oscillations are high due to the low σ_h value. It can be observed from the figure that our combiner is very close to the performance of the MRC at lower altitudes since our combiner benefits more from oscillations with high amplitude to maximize the average value of the SNR. At higher elevations, the deviation of our method from the MRC reaches to nearly 9 dB. In Fig. 3.11, σ_h is 0.2 m and the amplitude of the oscillations decreases due to the higher σ_h value. The performance of our combiner at lower altitudes is very close to the MRC as in the previous case, but, the maximum deviation decreases to nearly 6 dB since the amplitude of the oscillations decreases. In Fig. 3.12, σ_h is 0.5 m and the maximum deviation decreases to nearly 3 dB due to lower amplitude oscillations similar to the previous cases. In Fig. 3.13, σ_h is 1.0 m. The performance of our method almost did not change and the maximum deviation is nearly 3 dB again since the roughness (which depends on σ_h) does not affect the reflection coefficient significantly after this point (see Fig. 2.10).

In Fig. 3.14, the expected value of SNR for the MRC and our combiner are compared for different σ_h values. In this figure, it is seen that as σ_h varies, the deviation of our combiner from MRC in terms of the average value of the SNR does not change. However, both the performances of the MRC and our method decrease with increasing σ_h and after a value, σ_h has nearly no influence on both of them.

The simulations show that the proposed combining method should be improved which is the subject of the next section.

3.6 Improving the Performance by Using Narrower Height Intervals

The maximum deviation of our combining method from the MRC can reach to 11 dB as can be observed in Fig. 3.8. We solve this problem by dividing the target height, $h2$, interval, 40 m to 1000m, into equal pieces and exploring different weight vectors for each subinterval. The number of divisions is decided according to the desired maximum deviation from the MRC.

When the situation in Fig. 3.8 is simulated again using the improved algorithm with allowed maximum deviation of 1 dB, Fig. 3.15 is obtained.

The beams formed by our combining method before and after the improvement can be observed in Fig. 3.16. It is seen that there are four lobes for the beam after improvement corresponding to the division by four and the gain is increased significantly.

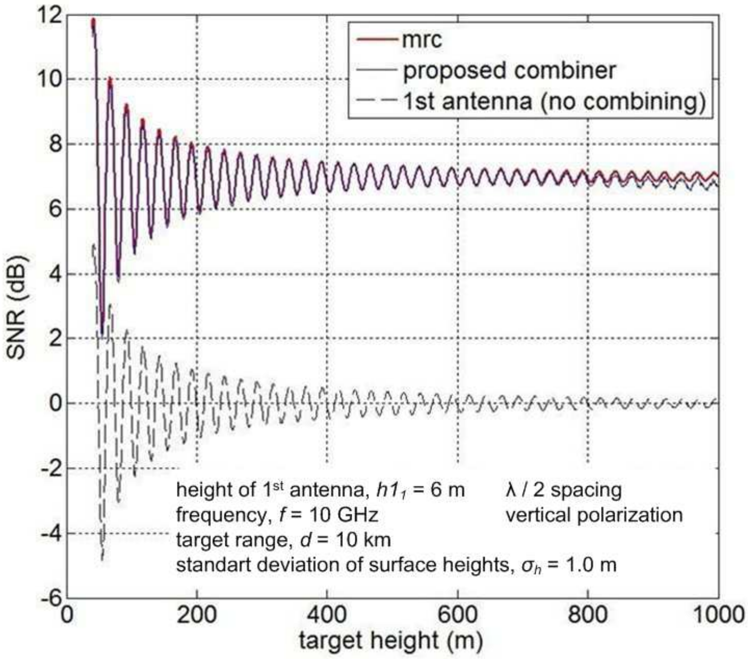

Figure 3.2: SNR versus target height for MRC, proposed combiner and 1st antenna when M(number of antennas) = 5

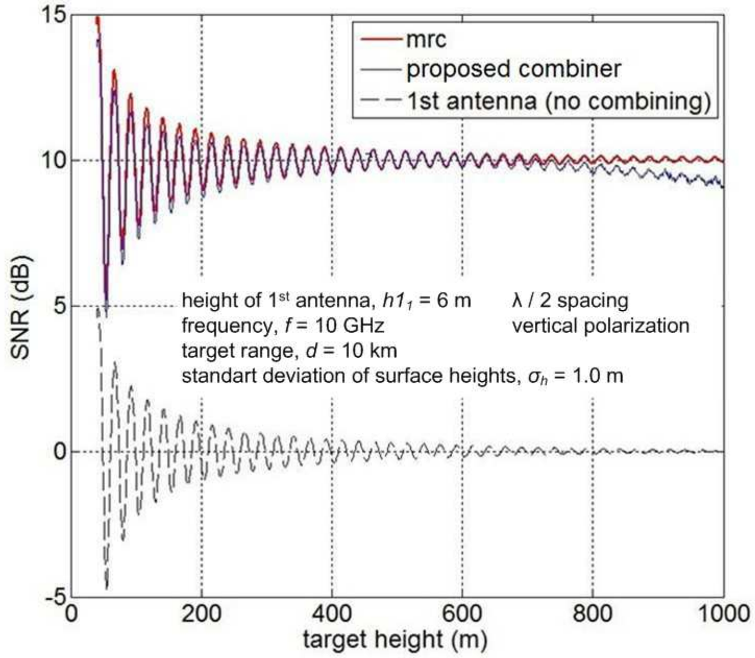

Figure 3.3: SNR versus target height for MRC, proposed combiner and 1st antenna when M(number of antennas) = 10

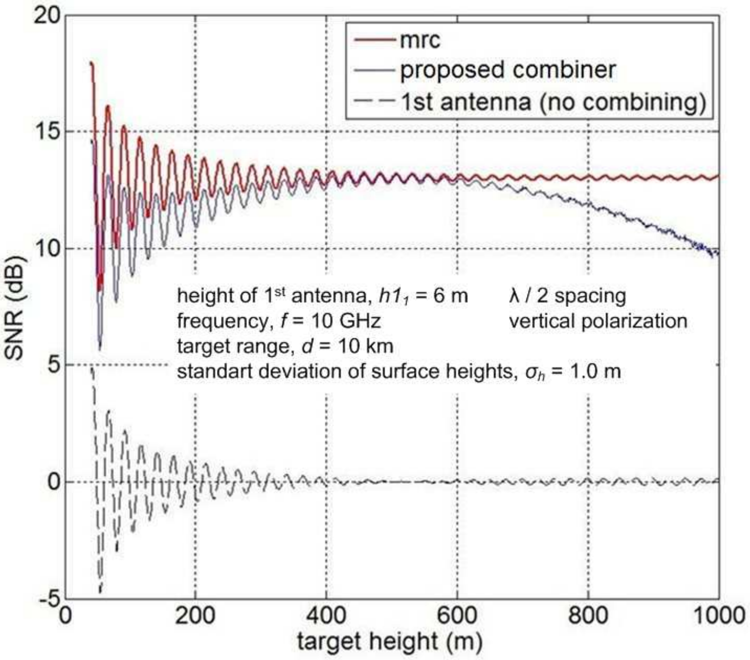

Figure 3.4: SNR versus target height for MRC, proposed combiner and 1st antenna when M(number of antennas) = 20

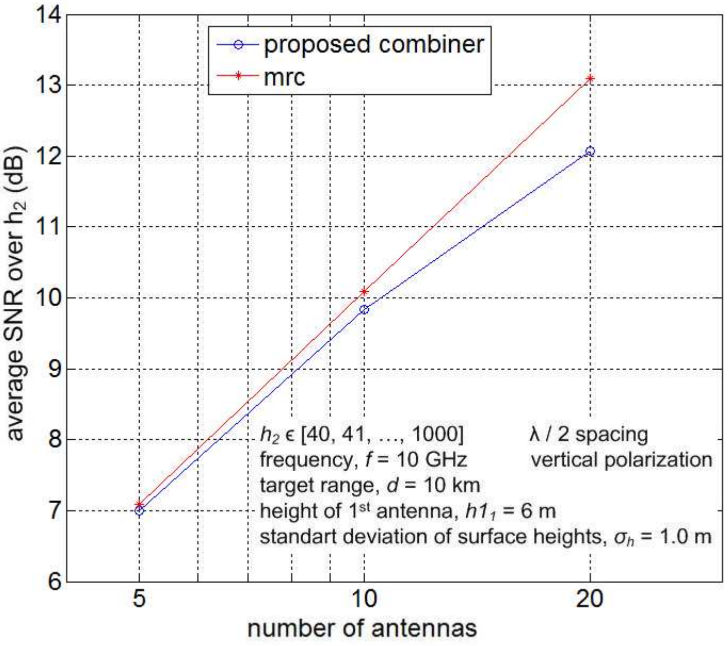

Figure 3.5: The average value of SNR versus number of antennas for MRC and proposed combiner

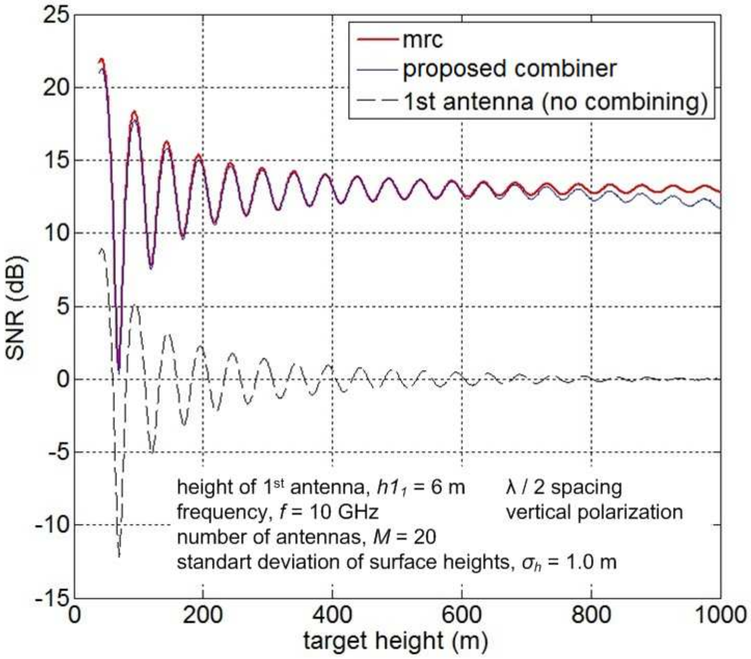

Figure 3.6: SNR versus target height for MRC, proposed combiner and 1st antenna when *d*(target range) = 20 km

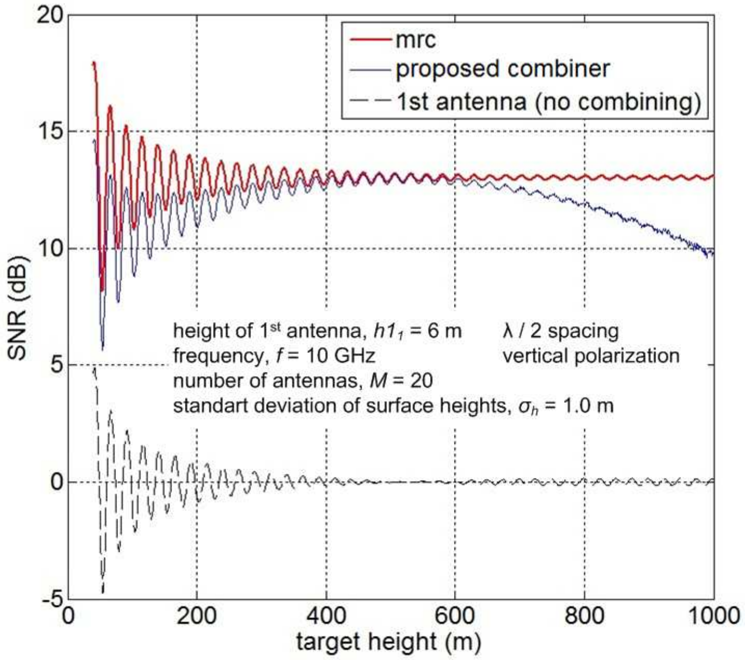

Figure 3.7: SNR versus target height for MRC, proposed combiner and 1st antenna when d(target range) = 10 km

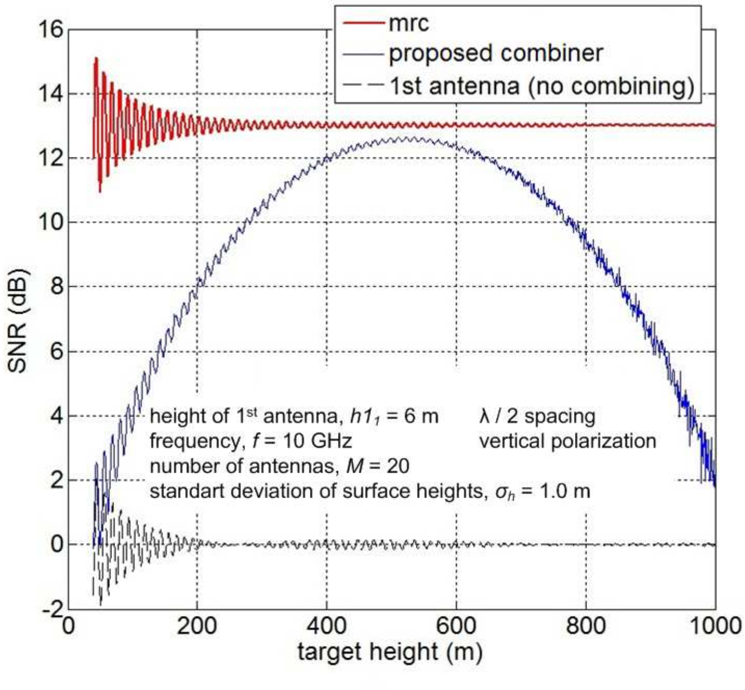

Figure 3.8: SNR versus target height for MRC, proposed combiner and 1st antenna when d(target range) = 5 km

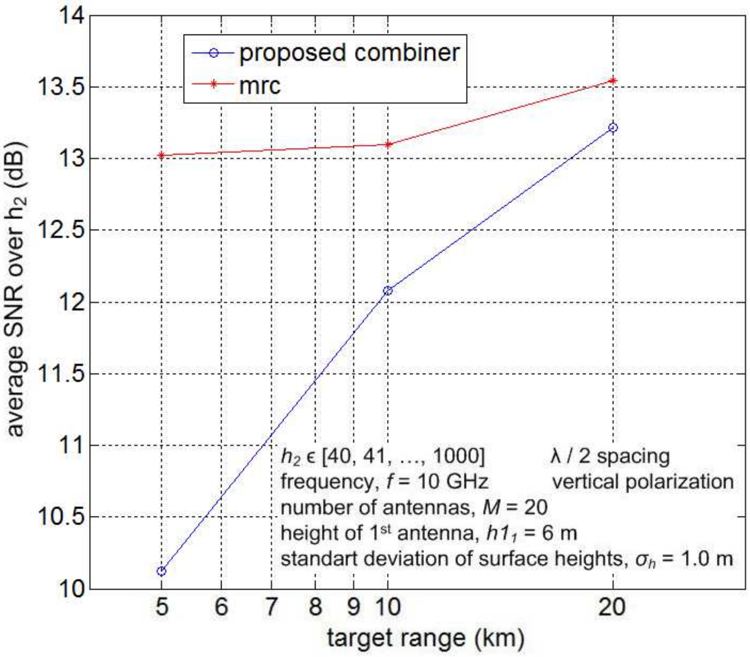

Figure 3.9: The average value of SNR versus target range for MRC and proposed combiner

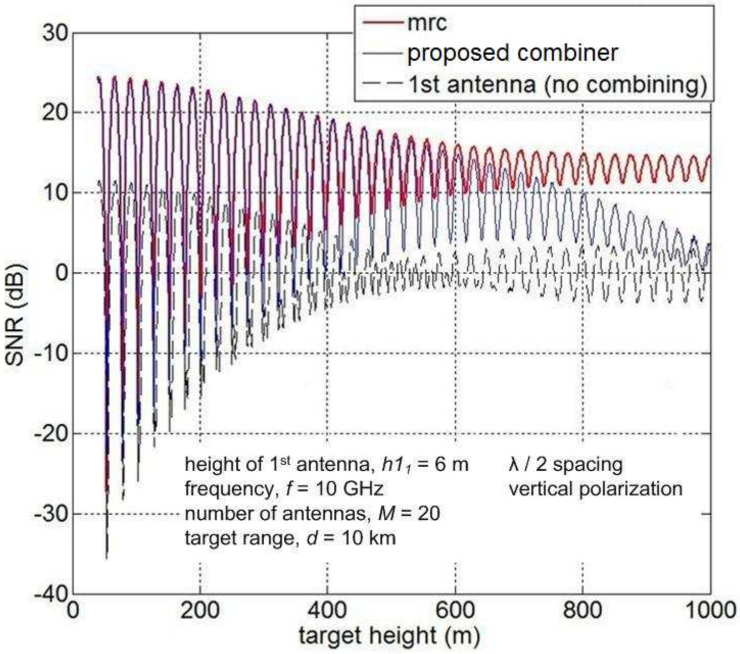

Figure 3.10: SNR versus target height for MRC, proposed combiner and 1st antenna when σ_h(standard deviation of normally distributed surface heights) = 0.05 m

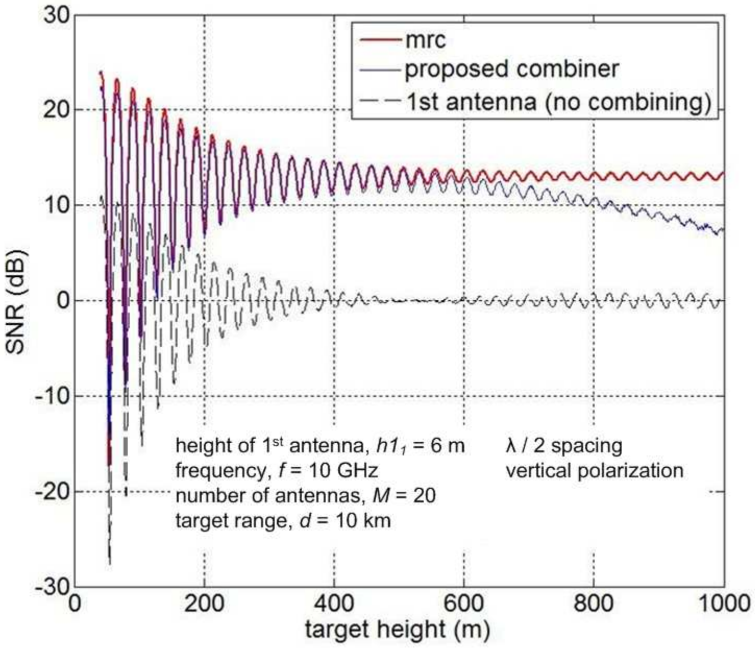

Figure 3.11: SNR versus target height for MRC, proposed combiner and 1st antenna when σ_h(standard deviation of normally distributed surface heights) = 0.2 m

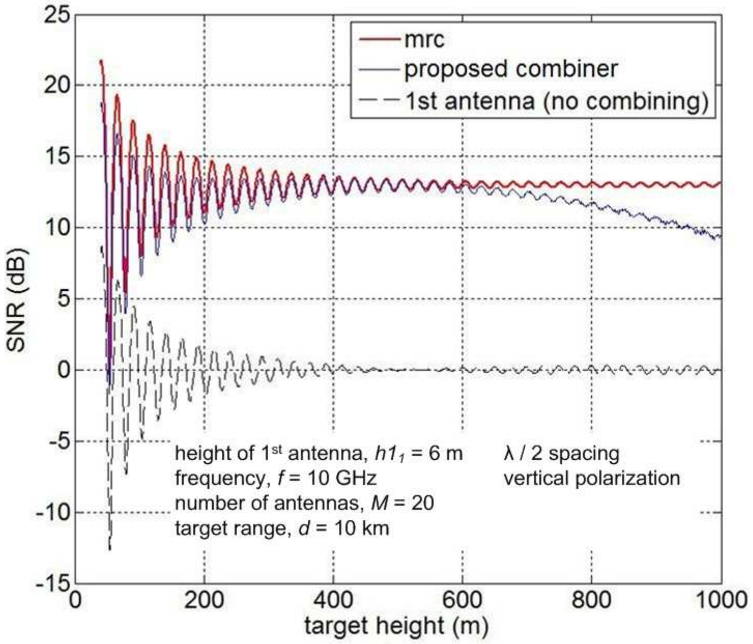

Figure 3.12: SNR versus target height for MRC, proposed combiner and 1st antenna when σ_h(standard deviation of normally distributed surface heights) = 0.5 m

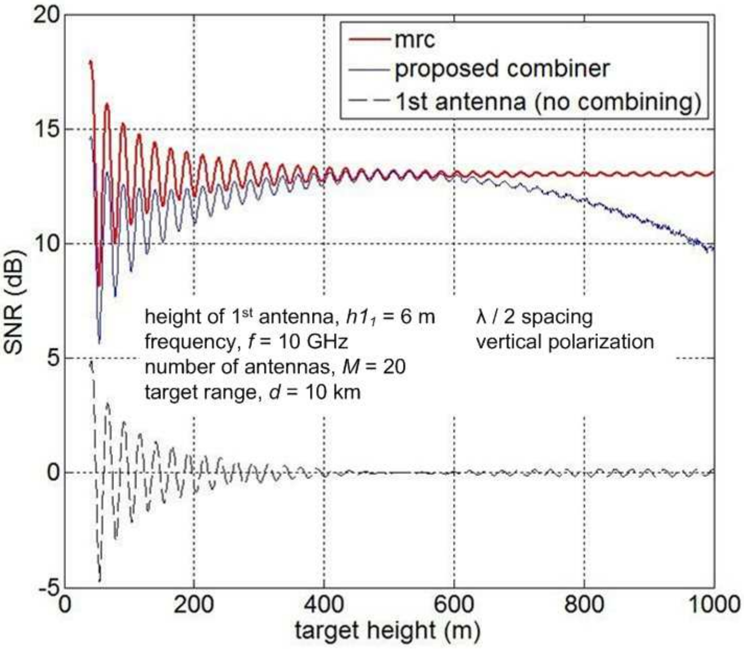

Figure 3.13: SNR versus target height for MRC, proposed combiner and 1st antenna when σ_h(standard deviation of normally distributed surface heights) = 1.0 m

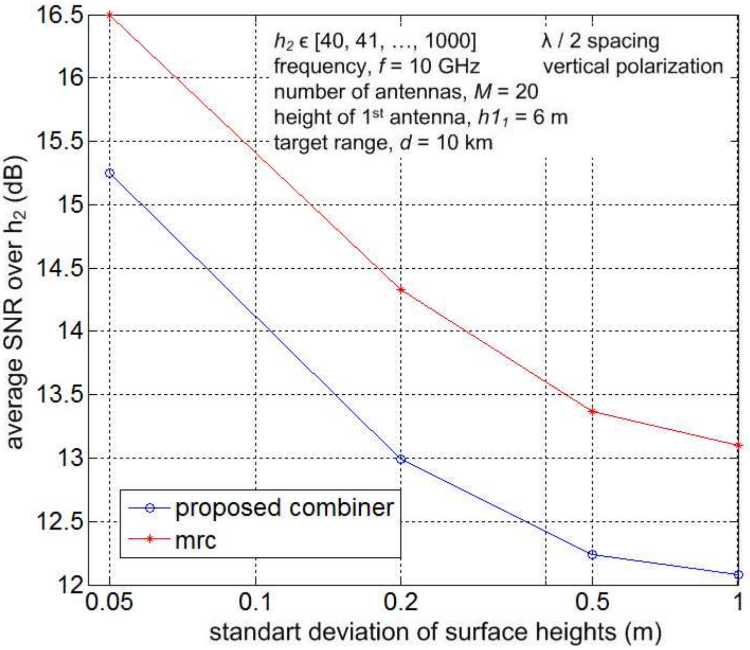

Figure 3.14: The average value of SNR versus standard deviation of normally distributed surface heights for MRC and proposed combiner

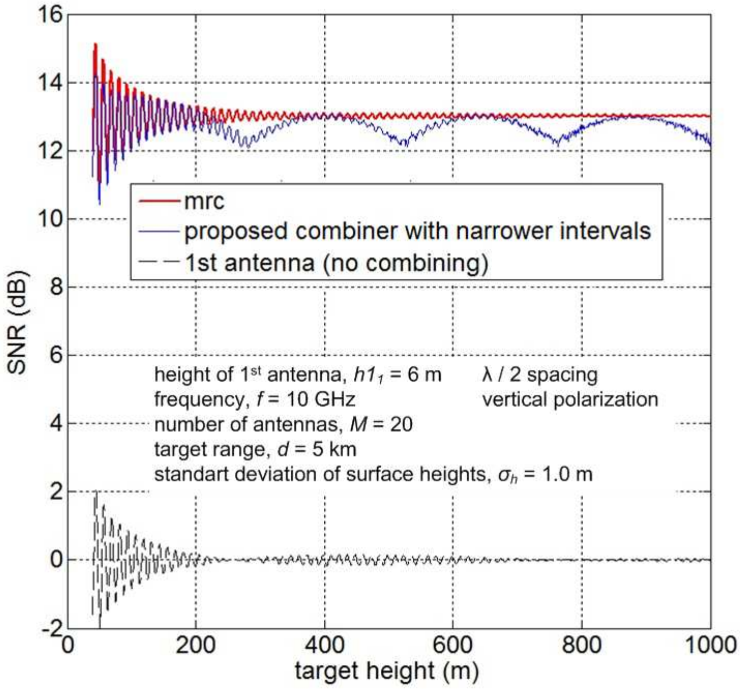

Figure 3.15: SNR versus target height for MRC, proposed combiner with narrower height intervals and 1st antenna (the situation in Fig. 3.8 but with improved combiner)

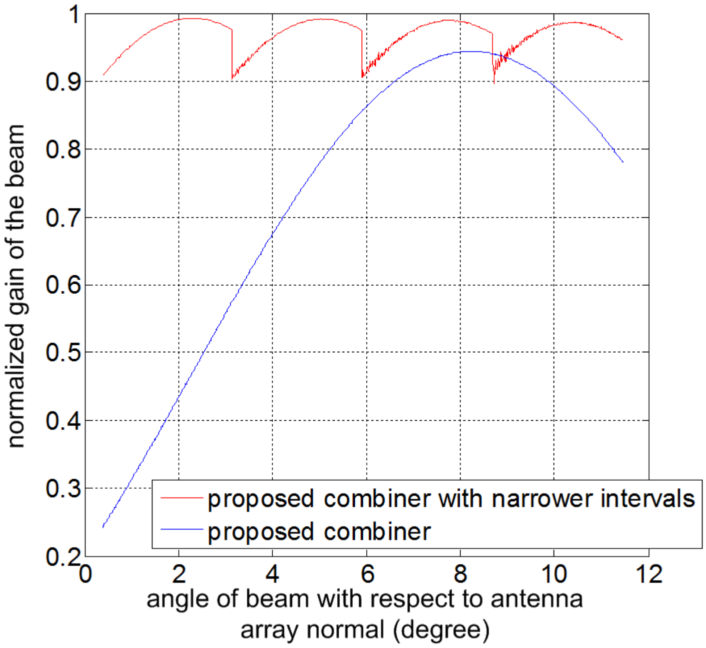

Figure 3.16: The beams formed by our combining method before and after improvement

CHAPTER 4

DIRECTION (HEIGHT) FINDING

Direction finding (DF) of targets flying at low altitudes by ground based radars is not trivial. There are numerous methods proposed in the literature and major ones have been summarized in Chapter 1. However, most of these methods suffer from the surface reflected signals. Since Maximum Likelihood Estimation (MLE) techniques are less sensitive to signal coherence, they usually offer better performance for low-angle DF [31, 30].

Refined Maximum Likelihood (RML) algorithm is one of MLE approaches in the literature and 'refined' refers to the use of a priori information of target range, radar height and surface roughness. In its multipath model, only specular component of the reflection is modeled and the diffuse scattering is excluded. Since the target range is a priori information, the direction of the target is found by estimating the target height. Therefore, by utilizing the priori information, the number of unknowns in the model are reduced and a one-dimensional search over the target height is executed. The reduced number of unknowns has a beneficial effect on estimation accuracy. The computational load is also reduced. So, RML algorithm offers better performance than other MLE techniques in the literature [26, 27]. However, RML function obtains ambiguous peaks in addition to the peak corresponding to the true target height. Therefore, frequency agility is required. By using an array radar with sufficient bandwidth and at least two different frequencies, the problem can be solved [26, 27, 28].

In this section, first, RML algorithm will be described. Then, our target height estimation technique, RML-D, which utilizes also MLE and includes the diffuse reflection in addition to the specular reflection in its multipath model will be explained. Finally, the two techniques will be compared via computer simulations.

4.1 RML Algorithm

The propagation model used in the RML is all the same with our propagation model formulated in Eq. 2.1 except the diffuse reflection since the diffuse component is not included in RML. Then, the noise-free signal received at the m_{th} element of an array of M sensors is

$$v_m = b\, f_m(h2), \quad m = 1, 2, ..., M \tag{4.1}$$

where $h2$ is the target height and

$$b = Q\Big[exp\Big\{-j\,k\,rd_{tr}\Big\} + \rho_s\, exp\Big\{-j\,k\,(r1_{tr} + r2_{tr})\Big\}\Big] \tag{4.2a}$$

$$f_m(h2) = exp\Big\{-j\,k\,rd_m\Big\} + \rho_s\, exp\Big\{-j\,k\,(r1_m + r2_m)\Big\}. \tag{4.2b}$$

In 4.2a, Q is an unknown complex amplitude due to target RCS. Q and $h2$ are treated as nonrandom parameters. The variables, $rd_{tr}, r1_{tr}, r2_{tr}, rd_m, r1_m, r2_m$ and ρ_s, are functions of $h2$ but we do not explicitly show the dependence here. Therefore, $f_m(h2)$ is a function of $h2$ as it can be inferred from its name and b is a function of $h2$ and Q. The idea is that b is defined by grouping the variables that are nonrandom and does not have an antenna number subscript, and $f_m(h2)$ is defined by grouping the variables that are nonrandom and have an antenna number subscript. By making such a grouping, it is aimed to simplify the analysis. Then, the total observation vector, **s**, is given by

$$\mathbf{s} = b\,\mathbf{f}(h2) + \mathbf{n}, \tag{4.3}$$

where the vectors (**s, f, n**) $\in C^{Mx1}$ and $b \in C^{1x1}$.

In Eq. 4.2a and 4.2b, the total number of unknowns is three: $h2$, real part of Q and imaginary part of Q. After making this grouping, the total number of unknowns is still three: $h2$, real part of b and imaginary part of b.

Since the additive noise vector, **n**, has components that are zero-mean, circularly symmetric complex Gaussian, independent and assumed to have same variances, σ_n^2, the conditional joint density, p(**s** | $b, h2$), of the observations, or the likelihood function L is given as

$$\begin{aligned} p(\mathbf{s} \mid \theta) &= \prod_{m=1}^{M} C\, exp\Big\{\frac{-(s_m - b\, f_m(h2))^*\ (s_m - b\, f_m(h2))}{2\,\sigma_n^2}\Big\} \\ &= C^M\, exp\Big\{-\sum_{m=1}^{M} \frac{(s_m - b\, f_m(h2))^*\ (s_m - b\, f_m(h2))}{2\,\sigma_n^2}\Big\} \\ &= C^M\, exp\Big\{-\frac{(\mathbf{s} - b\,\mathbf{f}(h2))^H\, (\mathbf{s} - b\,\mathbf{f}(h2))}{2\,\sigma_n^2}\Big\}, \end{aligned} \tag{4.4}$$

where $\theta = [b, h2]$ and C does not depend upon the parameters b or $h2$.

Then, the log-likelihood function for this case, after dropping the constants that are independent of the parameters, b or $h2$, becomes

$$L(\theta) = -\frac{(\mathbf{s} - b\,\mathbf{f}(h2))^H\,(\mathbf{s} - b\,\mathbf{f}(h2))}{\sigma_n^2} = -\frac{\|\mathbf{s} - b\,\mathbf{f}(h2)\|^2}{\sigma_n^2}. \tag{4.5}$$

We treat b and $h2$ as nonrandom parameters. Then, the partial derivative of L with respect to b must be zero for L to be maximized. Therefore,

$$\frac{\partial L}{\partial b} = \frac{2}{\sigma_n^2}\,\mathbf{f}(h2)^H\,(\mathbf{s} - b\,\mathbf{f}(h2)) = 0. \tag{4.6}$$

From Eq. 4.6,

$$b = \frac{\mathbf{f}(h2)^H\,\mathbf{s}}{\mathbf{f}(h2)^H\,\mathbf{f}(h2)}. \tag{4.7}$$

Combining Eq. 4.7 and Eq. 4.5, the log-likelihood function as a function of $h2$ is obtained as

$$L(h2) = \frac{\left\|\mathbf{s}^H\,\mathbf{f}(h2)\right\|^2}{\sigma_n^2\,\|\mathbf{f}(h2)\|^2} - \frac{\|\mathbf{s}\|^2}{\sigma_n^2}. \tag{4.8}$$

After placing plus signed terms to the nominator and negative signed terms to the denominator, the log-likelihood function in Eq. 4.8 is expressed as

$$L(h2) = \frac{1}{\|\mathbf{s}\|^2/\sigma_n^2}\,\frac{\left\|\mathbf{s}^H\,\mathbf{f}(h2)\right\|^2}{\sigma_n^2\,\|\mathbf{f}(h2)\|^2}. \tag{4.9}$$

Frequency agility is necessary for proper functioning of RML [26, 27]. We assume that the observation vectors at different frequencies are statistically independent from snapshot to snapshot. The noise levels may be different on each frequency since the receiver noise figure generally depends on the frequency. Then, the observation model is given by

$$\mathbf{s}_p = b_p\,\mathbf{f}_p(h2) + \mathbf{n}_p, \quad p = 1, 2, ..., P, \tag{4.10}$$

where P is the number of snapshots at different frequencies. The conditional joint density, p($\mathbf{s}_1, \mathbf{s}_2, ..., \mathbf{s}_P \mid b_1, b_2, ..., b_P, h2$), of the observations, or the likelihood function, L, is given as

$$p(\mathbf{s}_1, \mathbf{s}_2, ..., \mathbf{s}_P \mid \theta) = \prod_{p=1}^{P} C\,exp\left\{ -\frac{\left\|\mathbf{s}_p - b_p\,\mathbf{f}_p(h2)\right\|^2}{2\,\sigma_{n,p}^2} \right\}, \tag{4.11}$$

where $\theta = [b_1, b_2, ..., b_P, h2]$ and C does not depend upon the parameters in θ.

Then, the log-likelihood function, after dropping the constants that are independent of θ, becomes

$$L(\theta) = -\sum_{p=1}^{P} \frac{\left\|\mathbf{s}_p - b_p\,\mathbf{f}_p(h2)\right\|^2}{\sigma_{n,p}^2}. \tag{4.12}$$

L is desired to be maximized, therefore, the partial derivative of L with respect to b_p must be zero. This is expressed as

$$\frac{\partial L}{\partial b_p} = \frac{2}{\sigma_{n,p}^2} \mathbf{f}_p(h2)^H \left(\mathbf{s}_p - b_p \mathbf{f}_p(h2)\right) = 0. \tag{4.13}$$

From Eq. 4.13,

$$b_p = \frac{\mathbf{f}_p(h2)^H \mathbf{s}_p}{\mathbf{f}_p(h2)^H \mathbf{f}_p(h2)}. \tag{4.14}$$

Substituting Eq. 4.14 in Eq. 4.12, the log-likelihood function as a function of $h2$ is obtained as

$$L(h2) = \sum_{p=1}^{P} \frac{\left\|\mathbf{s}_p^H \mathbf{f}_p(h2)\right\|^2}{\sigma_{n,p}^2 \left\|\mathbf{f}_p(h2)\right\|^2} - \sum_{p=1}^{P} \frac{\left\|\mathbf{s}_p\right\|^2}{\sigma_{n,p}^2}. \tag{4.15}$$

After placing plus signed terms to the nominator and negative signed terms to the denominator, RML estimator of the target height with frequency agility becomes

$$L(h2) = \frac{1}{\sum_{p=1}^{P} \left\|\mathbf{s}_p\right\|^2 / \sigma_{n,p}^2} \sum_{p=1}^{P} \frac{\left\|\mathbf{s}_p^H \mathbf{f}_p(h2)\right\|^2}{\sigma_{n,p}^2 \left\|\mathbf{f}_p(h2)\right\|^2}, \tag{4.16}$$

It can be shown that $0 \leq L \leq 1$ by using the Cauchy-Schwarz inequality. The derivation can be found in APPENDIX A.

4.2 The Proposed ML Based Algorithm (RML-D)

The propagation model used here is the same with the propagation model formulated in Eq. 2.1, in which the diffuse component is included. Therefore, we named this model as RML with Diffuse (RML-D). In this model, the noise-free signal received at the m_{th} element of an array of M sensors is

$$\begin{aligned}
v_m &= Q\Big[exp\{-j\,k\,rd_{tr}\} + (\rho_s + \rho_d)\,exp\{-j\,k\,(r1_{tr} + r2_{tr})\}\Big] \times \\
&\quad \Big[exp\{-j\,k\,rd_m\} + (\rho_s + \rho_d)\,exp\{-j\,k\,(r1_m + r2_m)\}\Big] \\
&= \Big[\underbrace{Q\Big[exp\{-j\,k\,rd_{tr}\} + \rho_s\,exp\{-j\,k\,(r1_{tr} + r2_{tr})\}\Big]}_{b} + \rho_d\ \underbrace{Q\,exp\{-j\,k\,(r1_{tr} + r2_{tr})\}}_{c}\Big] \times \\
&\quad \Big[\underbrace{exp\{-j\,k\,rd_m\} + \rho_s\,exp\{-j\,k\,(r1_m + r2_m)}_{f_m(h2)} + \rho_d\ \underbrace{exp\{-j\,k\,(r1_m + r2_m)\}}_{g_m(h2)}\Big] \\
&= (b + c\,\rho_d)(f_m(h2) + \rho_d\ g_m(h2))
\end{aligned} \tag{4.17}$$

In Eq. 4.17, Q is an unknown deterministic complex amplitude as in the case of RML. The variables, $rd_{tr}, r1_{tr}, r2_{tr}, rd_m, r1_m, r2_m$ and ρ_s, are functions of $h2$ but it is not indicated explicitly here. The diffuse reflection coefficient, ρ_d, is distributed as circularly symmetric complex Gaussian. Therefore, $f_m(h2)$ and $g_m(h2)$ are functions of $h2$ as it can be inferred from their names and, b and c are both functions of $h2$ and Q. Following the same procedure, we grouped the parameters that are nonrandom and does not have an antenna number subscript and, defined b and c. We also grouped the parameters that are nonrandom and have an antenna number subscript and, defined $f_m(h2)$ and $g_m(h2)$. Then, the total observation vector becomes

$$\mathbf{s} = (b + c\rho_d)(\mathbf{f}(h2) + \rho_d\ \mathbf{g}(h2)) + \mathbf{n}, \tag{4.18}$$

where vectors $(\mathbf{s, f, g, n}) \in C^{Mx1}$ and $(b, c, \rho_d) \in C^{1x1}$.

In Eq. 4.17, the total number of unknowns is five: real and imaginary part of Q, real and imaginary part of ρ_d and $h2$. After grouping, the total number of unknowns in Eq. 4.18 is seven: b, c, ρ_d and $h2$ since $(b, c, \rho_d) \in C^{1x1}$. The increase in unknowns is not a mistake since b and c are dependent on the same parameters and one of them is a dependent parameter.

The noise properties are taken identical to that of RML. Therefore, the likelihood function, L, is given by

$$p(\mathbf{s} \mid \theta) = E\ exp\left\{ \frac{-\left(\mathbf{s} - (b + c\rho_d)(\mathbf{f}(h2) + \rho_d\,\mathbf{g}(h2))\right)^H \left(\mathbf{s} - (b + c\rho_d)(\mathbf{f}(h2) + \rho_d\,\mathbf{g}(h2))\right)}{2\,\sigma_n^2} \right\}, \tag{4.19}$$

where $\theta = [b, c, \rho_d, h2]$ and E does not depend upon the parameter vector θ.

Then, after dropping the constants independent of the parameter vector θ, the log-likelihood function to be maximized becomes

$$\begin{aligned} L(\theta) &= -\frac{\left(\mathbf{s} - (b + c\rho_d)(\mathbf{f}(h2) + \rho_d\,\mathbf{g}(h2))\right)^H \left(\mathbf{s} - (b + c\rho_d)(\mathbf{f}(h2) + \rho_d\,\mathbf{g}(h2))\right)}{\sigma_n^2} \\ &= -\frac{\left\|\mathbf{s} - (b + c\rho_d)(\mathbf{f}(h2) + \rho_d\,\mathbf{g}(h2))\right\|^2}{\sigma_n^2}. \end{aligned} \tag{4.20}$$

The partial derivative of L with respect to b must be zero for L to be maximized. Therefore,

$$\frac{\partial L}{\partial b} = \frac{2}{\sigma_n^2}\left(\mathbf{f}(h2) + \rho_d\,\mathbf{g}(h2)\right)^H \left(\mathbf{s} - (b + c\rho_d)(\mathbf{f}(h2) + \rho_d\,\mathbf{g}(h2))\right) = 0. \tag{4.21}$$

From Eq. 4.21,

$$b = \frac{\left(\mathbf{f}(h2) + \rho_d\,\mathbf{g}(h2)\right)^H \left(\mathbf{s} - c\rho_d\left(\mathbf{f}(h2) + \rho_d\,\mathbf{g}(h2)\right)\right)}{\left(\mathbf{f}(h2) + \rho_d\,\mathbf{g}(h2)\right)^H \left(\mathbf{f}(h2) + \rho_d\,\mathbf{g}(h2)\right)}. \tag{4.22}$$

Combining Eq. 4.22 and Eq. 4.20, the unknown and dependent parameter, c, disappears mathematically. This is expected since b and c are dependent on the same parameters: Q and $h2$. Then, the log-likelihood function becomes

$$L(\rho_d, h2) = \frac{\left\|\mathbf{s}^H\left(\mathbf{f}(h2) + \rho_d\,\mathbf{g}(h2)\right)\right\|^2}{\sigma_n^2\,\left\|\left(\mathbf{f}(h2) + \rho_d\,\mathbf{g}(h2)\right)\right\|^2} - \frac{\|\mathbf{s}\|^2}{\sigma_n^2}. \tag{4.23}$$

The log-likelihood function in Eq. 4.23 can also be expressed as

$$L(\rho_d, h2) = \frac{1}{\|\mathbf{s}\|^2/\sigma_n^2}\,\frac{\left\|\mathbf{s}^H\left(\mathbf{f}(h2) + \rho_d\,\mathbf{g}(h2)\right)\right\|^2}{\sigma_n^2\,\left\|\left(\mathbf{f}(h2) + \rho_d\,\mathbf{g}(h2)\right)\right\|^2}. \tag{4.24}$$

If the frequency agility is used, the observation vector, $\mathbf{s}_p$, is given by

$$\mathbf{s}_p = (b_p + c_p\,\rho_{d,p})(\mathbf{f}_p(h2) + \rho_{d,p}\ \mathbf{g}_p(h2)) + \mathbf{n}_p, \quad p = 1, 2, ..., P \tag{4.25}$$

where P is the number of frequencies.

Then, assuming that the observation vectors at different frequencies are statistically independent from snapshot to snapshot, the likelihood function, L, becomes

$$p(\mathbf{s}_1, \mathbf{s}_2, ..., \mathbf{s}_P \mid \theta) = \prod_{p=1}^{P} E\ exp\left\{\frac{-\left\|\mathbf{s}_p - (b_p + c_p\,\rho_{d,p})(\mathbf{f}_p(h2) + \rho_{d,p}\,\mathbf{g}_p(h2))\right\|^2}{2\,\sigma_{n,p}^2}\right\}, \tag{4.26}$$

where $\theta = [b_1, b_2, ..., b_P, c_1, c_2, ..., c_P, \rho_{d,1}, \rho_{d,2}, ..., \rho_{d,P}, h2]$ and E does not depend upon the parameter vector θ.

After dropping the constants independent of the parameter vector θ, the log-likelihood function becomes

$$L(\theta) \ = \ -\sum_{p=1}^{P} \frac{\left\|\mathbf{s}_p - (b_p + c_p\rho_{d,p})(\mathbf{f}_p(h2) + \rho_{d,p}\,\mathbf{g}_p(h2))\right\|^2}{\sigma_{n,p}^2}. \tag{4.27}$$

The partial derivative of L with respect to b_p must be zero for L to be maximized. Therefore,

$$\frac{\partial L}{\partial b_p} = \frac{2}{\sigma_{n,p}^2}\left(\mathbf{f}_p(h2) + \rho_{d,p}\,\mathbf{g}_p(h2)\right)^H\left(\mathbf{s}_p - (b_p + c_p\,\rho_{d,p})(\mathbf{f}_p(h2) + \rho_{d,p}\,\mathbf{g}_p(h2))\right) = 0. \tag{4.28}$$

From Eq. 4.28,

$$b_p = \frac{\left(\mathbf{f}_p(h2) + \rho_{d,p}\,\mathbf{g}_p(h2)\right)^H\left(\mathbf{s}_p - c_p\,\rho_{d,p}\left(\mathbf{f}_p(h2) + \rho_{d,p}\,\mathbf{g}_p(h2)\right)\right)}{\left(\mathbf{f}_p(h2) + \rho_{d,p}\,\mathbf{g}_p(h2)\right)^H\left(\mathbf{f}_p(h2) + \rho_{d,p}\,\mathbf{g}_p(h2)\right)}. \tag{4.29}$$

Substituting Eq. 4.29 in Eq. 4.27, the unknown parameter, c_p, disappears mathematically as expected. Then, the log-likelihood function becomes

$$L(\rho_{d,1}, ..., \rho_{d,P}, h2) = \sum_{p=1}^{P} \frac{\left\|\mathbf{s}_p^H\left(\mathbf{f}_p(h2) + \rho_{d,p}\ \mathbf{g}_p(h2)\right)\right\|^2}{\sigma_{n,p}^2\,\left\|\left(\mathbf{f}_p(h2) + \rho_{d,p}\ \mathbf{g}_p(h2)\right)\right\|^2} - \sum_{p=1}^{P} \frac{\left\|\mathbf{s}_p\right\|^2}{\sigma_{n,p}^2}, \tag{4.30}$$

Eq. 4.30 can also be expressed as

$$L(\rho_{d,1},...,\rho_{d,P},h2) = \frac{1}{\sum_{p=1}^{P}\left\|\mathbf{s}_p\right\|^2/\sigma_{n,p}^2}\sum_{p=1}^{P}\frac{\left\|\mathbf{s}_p^H\left(\mathbf{f}_p(h2)+\rho_{d,p}\ \mathbf{g}_p(h2)\right)\right\|^2}{\sigma_{n,p}^2\ \left\|\left(\mathbf{f}_p(h2)+\rho_{d,p}\ \mathbf{g}_p(h2)\right)\right\|^2}, \tag{4.31}$$

By using the Cauchy-Schwarz inequality, we can show that $0 \leq L \leq 1$. The derivation is in APPENDIX A.

In Eq. 4.31, there are (1 + 2P) unknowns: $[\rho_{d,1},\rho_{d,2},...,\rho_{d,P},h2]$ since $[\rho_{d,1},\rho_{d,2},...,\rho_{d,P}] \in C^{1x1}$. What we desire is to obtain the likelihood function as a function of only $h2$. It is known that real and imaginary parts of $\rho_{d,p}$, for $p = 1,2,...,P$, are zero mean independent Gaussian random variables whose variances are the same and determined by the surface roughness (Eq. 2.31). The variance is maximum when roughness factor is equal to 0.1. When the variance is maximum, the real and imaginary parts of $\rho_{d,p}$ take values essentially between -2.5 and 2.5 according to Gaussian distribution. For a particular $h2$, we find $[\rho_{d,1},\rho_{d,2},...,\rho_{d,P}]$ values maximizing the likelihood function among mentioned possible values. Therefore, the estimated $[\rho_{d,1},\rho_{d,2},...,\rho_{d,P}]$ values are different for every $h2$. So, we obtain likelihood function as a function of only $h2$ by this way. The target height estimate becomes the value maximizing the likelihood function and the estimated diffuse reflection coefficient values at different frequencies becomes $[\rho_{d,1},\rho_{d,2},...,\rho_{d,P}]$ values belonging to the estimated target height value. To make it more clear, this is not a Maximum A Priori (MAP) estimation. If MAP estimation were utilized, there would be a term, $\ln p(\rho_{d,1},\rho_{d,2},...,\rho_{d,P})$, in Eq. 4.31.

It is important to see that when the diffuse reflection coefficient, $\rho_{d,p}$, in Eq. 4.31 is equated to zero, the likelihood function is transformed to the likelihood function of RML algorithm in Eq. 4.16.

In Fig. 4.1, the likelihood functions of both the RML algorithm and the proposed RML-D algorithm are calculated for a target range of 5 km, a target height of 30 m, a vertical array of vertically polarized 20 elements starting at 10 m above the surface with 0.0625 m spacing, two transmitted radar frequencies of 9 and 10 GHz, a rough surface with $\sigma_h = 0.5$ m, $R_{eq} =$ 8500 km and an SNR of nearly 12 dB. It is seen that the multiple peaks of the RML function leads to height ambiguity problem. On the other hand, the proposed RML-D algorithm does not show such a multiple peak behavior. This is because the diffuse reflection coefficient is constant and always equal to zero in RML algorithm while in RML-D algorithm, the diffuse

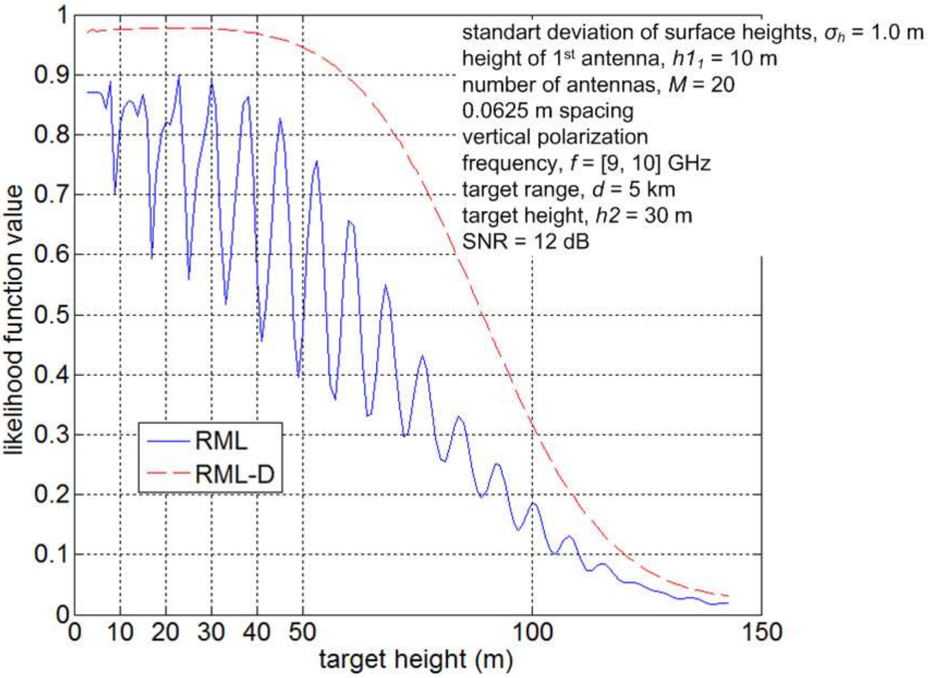

Figure 4.1: Example of RML algorithm and proposed RML-D algorithm

reflection coefficients at a particular $h2$ are the ones maximizing the likelihood function at this particular $h2$ and the diffuse reflection coefficients for different $h2$ are different. This also leads to that the likelihood function of RML-D algorithm is always greater or at least equal to that of RML algorithm.

4.3 Simulation Results

In this section, we compare the performance of the RML algorithm and the proposed RML-D algorithm by determining the root-mean-square-error (RMSE) of the target height estimation from 100 Monte-Carlo trials for different situations. In all simulations, the electromagnetic properties of the reflecting surface, ϵ_{1r} and σ_s, are set to 4 and 1×10^{-3} S respectively. The earth equivalent radius, R_{eq}, is set to 8500 km to include refraction. Since the frequency agility is necessary for proper functioning of presented ML solutions, three transmitted radar frequencies of 8, 10 and 12 GHz are used.

In Fig. 4.2-4.11, the number of antennas in the receiver array is equal to 20. They are vertically polarized and placed with 0.0625 m spacing. The standard deviation of normally distributed surface height, σ_h, is set to 1.0 m. SNR is not constant due to surface reflection. It varies with the target height, $h2$, target range, d, and the height of the first array element, $h1_1$, and fluctuates around 12 dB. This SNR is a per-element signal-to-noise ratio. It is calculated for a single snapshot at each frequency and is summed over the number of frequencies [26, 27, 28]:

$$SNR_{dB} = 10\,log\left\{\sum_{p=1}^{P}\frac{\left\|b_p\,\mathbf{f}(h2)\right\|^2}{2\,M\,\sigma_n^2}\right\}, \tag{4.32}$$

where P is the number of frequencies, σ_n^2 is the noise power and is assumed to be the same for all frequencies, and b_p is the complex signal amplitude at the element.

In Fig. 4.2, the target range, d, is set to 5 km and the target height, $h2$, versus RMSE is presented for various values of first array element height, $h1_1$. Fig. 4.2(a) shows the results of the RML algorithm. As it can be observed, the RML algorithm works well for the targets flying at nearly 5-10 m. However, RMSE peaks at the target height of nearly 25 m for all antenna height values. Then, as the target height increases further from 25 m, RMSE decreases and RMSE stabilizes to nearly 2 m for the targets flying higher than nearly 80 m. This behavior of RML algorithm is similar to the behavior of the diffuse reflection (Fig. 2.10). As the target height, $h2$, increases, the roughness factor increases due to the increasing grazing angle (Eq. 2.29). The mean of the magnitude of the diffuse scattering reflection coefficient increases with increasing roughness factor and, after reaching at a peak, it decreases for greater roughness. Finally, it becomes stable. This is what we expected since RML algorithm excludes the diffuse scattering while calculating the likelihood function. In other words, RML algorithm assumes that the diffuse reflection coefficient is equal to zero. Therefore, it is adversely affected by strong diffuse reflection and its error is mainly governed by the diffuse scattering. Fig. 4.2(b) shows the results of the proposed RML-D algorithm in which we included the diffuse reflection. Here, it is seen that RMSE peaks for the targets flying at an altitude of nearly 5-10 m. Then, RMSE decreases with increasing target height and stabilizes to nearly 2 m for the targets flying higher than nearly 80 m. From this behavior, we can say that RML-D algorithm achieves to suppress the errors caused by the diffuse scattering when the target is at an altitude around 25 m. However, RML-D algorithm can not find the height of the target as accurately as the RML algorithm when the target is at 5-10 m height. In fact, at 5-10 m height, the diffuse component is very near to zero, and when the diffuse component is zero, RML algorithm and the proposed RML-D algorithm are equal mathematically. Therefore, it can be deduced that the performance of RML algorithm is better than that of RML-D algorithm at 5-10 m due to poor performance of the diffuse reflection coefficient, ρ_d, estimation algorithm of RML-D algorithm. A better ρ_d estimation algorithm can fix this situation.

In Fig. 4.3 and Fig. 4.4, the target range, d, is set to 10 km and 20 km, respectively. It is seen that as the target range increases, the peak of the errors of both algorithms generally increase as expected since the reflections become more comparable with the direct wave at greater ranges and lead to greater errors. In Fig. 4.3(a) and Fig. 4.4(a), it is again seen that RML algorithm performs poorly where the diffuse reflection is strong and its RMSE characteristic is mainly governed by the diffuse scattering. On the other hand, RML-D algorithm can suppress the effects of diffuse scattering but, as Fig. 4.3(b) and Fig. 4.4(b) indicate, our method shows higher errors at very low altitudes where the RML algorithm works well. This is due to poor performance of diffuse reflection coefficient estimation algorithm of RML-D algorithm at these very low altitudes.

The data in Fig. 4.2 - 4.4 are presented in different ways in Fig. 4.5 - 4.7 and Fig. 4.8 - 4.11. In Fig. 4.5 - 4.7, the first array element height, $h1_1$, versus RMSE for various target height, $h2$, values are shown at different target ranges. In Fig. 4.5, the target range, d, is set to 5 km. In Fig. 4.5(a), it is easier to see that the RML algorithm shows the most RMSE at the target height of 25 m. This is where the diffuse scattering is very strong. This happens at the target height of 50 m when the range is 10 km as seen in Fig. 4.6(a) and at the target height between 80 m and 150 m when the range is 20 km as seen in Fig. 4.7(a). In Fig. 4.5(b) - 4.7(b), it is again observed that the offset in RMSE of RML-D algorithm occurs at very low altitudes due to poor performance of diffuse reflection coefficient estimation algorithm and this error generally decreases with increasing target height. Also, in Fig. 4.5 - 4.7, it is easily seen that RMSE of our method shows less variation with the antenna height.

In Fig. 4.8 - 4.11, the target range, d, versus RMSE for various target height, $h2$, values are shown at different first array element heights. In Fig. 4.8(a) - 4.11(a), it can be again observed that RML algorithm is adversely affected by the diffuse scattering and the target locations where the diffuse reflection is strong are where the error of RML algorithm peaks. In Fig. 4.8(b) - 4.11(b), it is seen that as the target range increases, this leads to more offset error in RML-D algorithm.

In Fig. 4.12 and Fig. 4.13, the effect of SNR on RMSE of both algorithms are shown. The number of the antennas in the receiver array is equal to 20. They are vertically polarized and placed with 0.0625 m spacing. The standard deviation of normally distributed surface height, σ_h, is set to 1.0 m. In Fig. 4.12, the target range, d, is set to 10 km and the target height, $h2$, is set to 50 m. As it is observed in the previous figures, this is one of the geometries where the diffuse scattering is strong. In Fig. 4.12(a), it is observed that RML algorithm is affected negatively by the diffuse reflection. When the antenna height is 50 m, the performance of RML algorithm improves partly with increasing SNR since the roughness is higher and the diffuse scattering is weaker. However, the increase in SNR has almost no effect on RMSE for the antenna heights smaller than 25 m. In Fig. 4.12(b), our algorithm shows also high errors at low SNR, but it can improve its performance as the SNR increases unlike the RML algorithm. In Fig. 4.13, the target height, $h2$, is varied to 150 m. In this geometry, the diffuse scattering is not strong and the target is high enough that our algorithm does not exhibit offset errors. Therefore, it is seen that the errors are not as high as the errors in Fig. 4.12. Also, for this case, it is seen that the performance of the RML algorithm improves, as expected, as the SNR increases since the diffuse scattering is weak.

In Fig. 4.14 and Fig. 4.15, SNR is around 12 dB. The number of the antennas in the receiver array is equal to 20. They are vertically polarized and placed with 0.0625 m spacing. In these figures, the effect of the surface irregularity on RMSE of both algorithms are explored by changing the standard deviation of normally distributed surface height, σ_h. In Fig. 4.14, the target range, d, is set to 10 km and the target height, $h2$, is set to 50 m. By varying σ_h, the roughness factor is changed (Eq. 2.29), therefore, the diffuse reflection characteristic is again observed in Fig. 4.14(a) as expected. In Fig. 4.14(a), for this position of the target, it is seen that the diffuse scattering is strong for σ_h values between 0.5 and 1.0 m. We already know from the previous figures that the diffuse scattering is strong for σ_h value of 1.0 m when target is at that position. In Fig. 4.15, the target height, $h2$, is varied to 150 m. From the previous figures, it is expected that the diffuse scattering is not strong for this target location when σ_h is equal to 1.0 m. This is what we observe in Fig. 4.15(a). It is also seen that the diffuse scattering is strong for σ_h values between 0.2 and 0.5 m. In Fig. 4.14(b) and Fig. 4.15(b), it is observed that RML-D algorithm is more robust to variation of σ_h. Moreover, it can be concluded that it is not the roughness factor determining RMSE of RML-D algorithm, but it is the grazing angle.

In Fig. 4.16 and Fig. 4.17, the effect of the number of antennas on RMSE of both algorithms are shown. The standard deviation of normally distributed surface height, σ_h, is set to 1.0 m and SNR is kept around 12 dB. The antennas are vertically polarized and placed with 0.0625 m spacing. In Fig. 4.16, the target range, d, is set to 10 km and the target height, $h2$, is set to 50 m. In Fig. 4.16(a), it is seen that it is impossible to drop RMSE of the RML algorithm considerably by increasing the number of antennas when the diffuse scattering is strong. On the other hand, in Fig. 4.16(b), it is observed that RML-D algorithm shows very high errors for the number of antennas smaller than 10. However, RMSE of RML-D algorithm can be adjusted to below 10 m by making the number of antennas greater than or equal to 20. In Fig. 4.17, the target height, $h2$, is changed to 150 m. RML-D algorithm again performs poorly for the number of antennas smaller than 10. For this case, the two algorithms perform nearly the same for the number of antennas larger than or equal to 10 and result in RMSE below 10 m. The poor performance of RML-D algorithm for the number of antennas smaller than 10 is due to the diffuse reflection coefficient estimation algorithm of RML-D algorithm. As it is previously mentioned, the likelihood function of RML algorithm contains multiple peaks whereas that of RML-D algorithm is smooth and always greater than or equal to the likelihood function of RML algorithm (4.1) due to the diffuse reflection coefficient estimation algorithm. When the number of the antennas becomes smaller than 10, the likelihood function of RML-D algorithm becomes very smooth such that its peak becomes nearly unrecognizable. Therefore, high error is observed in RML-D algorithm for small number of antennas. If the distribution of the diffuse reflection coefficient is used in Eq. 4.31 and a MAP estimation is utilized, a better performance can be achieved in RML-D algorithm.

In Fig. 4.18, the effect of the antenna polarization on both algorithms are shown. The standard deviation of normally distributed surface height, σ_h, is set to 1.0 m and SNR is kept around 8 dB. The number of antennas is 20 and they are placed with 0.0625 m spacing. The target range, d, is set to 10 km and the first antenna height, $h1_1$, is set to 10 m. It is seen that the performances of both algorithms are nearly independent of antenna polarization.

From the simulations, we note that the RML algorithm is adversely affected by the diffuse scattering and its error is mainly governed by the diffuse reflection. On the other hand, the RML-D algorithm succeeds to suppress the errors caused by diffuse scattering. However, the RML-D algorithm performs poorly at very low altitudes where the RML algorithm works well. This is because of that the RML algorithm assumes that the diffuse reflection coefficient is zero, which becomes a valid assumption at very shallow elevation angle. On the other hand, the RML-D algorithm employs an estimation procedure for the diffuse reflection coefficients, hence, it is prone to estimation error. MAP formulation, instead of ML, can fix performance of RML-D at very low elevations.

If it is desired to design a ground based radar that is capable of finding the direction of the targets that are at a range between 5 and 10 km and at an altitude between 5 and 500 m with an RMSE below 10 m, according to our simulations, the RML algorithm can not be used since RMSE of the RML algorithm will definitely be greater than 10 m where the diffuse scattering is strong. RML-D algorithm can be used under the conditions that

- first array element height, $h1_1$, can be between 6 and 25 m,
- SNR must be larger than nearly 15 dB,
- number of antennas must be equal to at least 20.

The proposed RML-D algorithm is almost independent of surface irregularity, and the algorithm can be expected to be useful for all σ_h values. Also, the algorithm is expected to work for both vertical and horizontal algorithms.

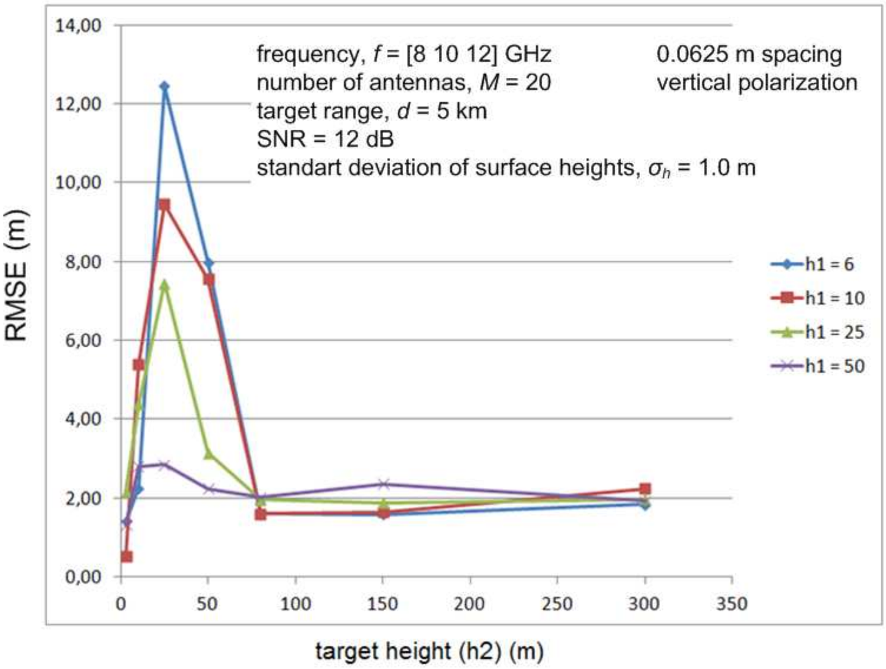

(a) RML algorithm

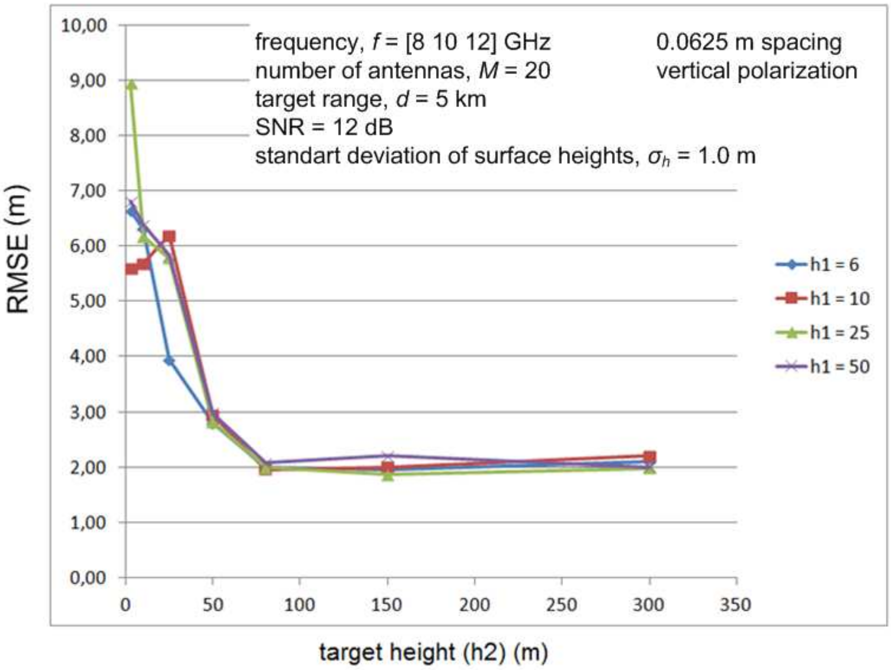

(b) RML-D algorithm

Figure 4.2: Target height vs RMSE at a range of $d = 5$ km a) RML and b) RML-D

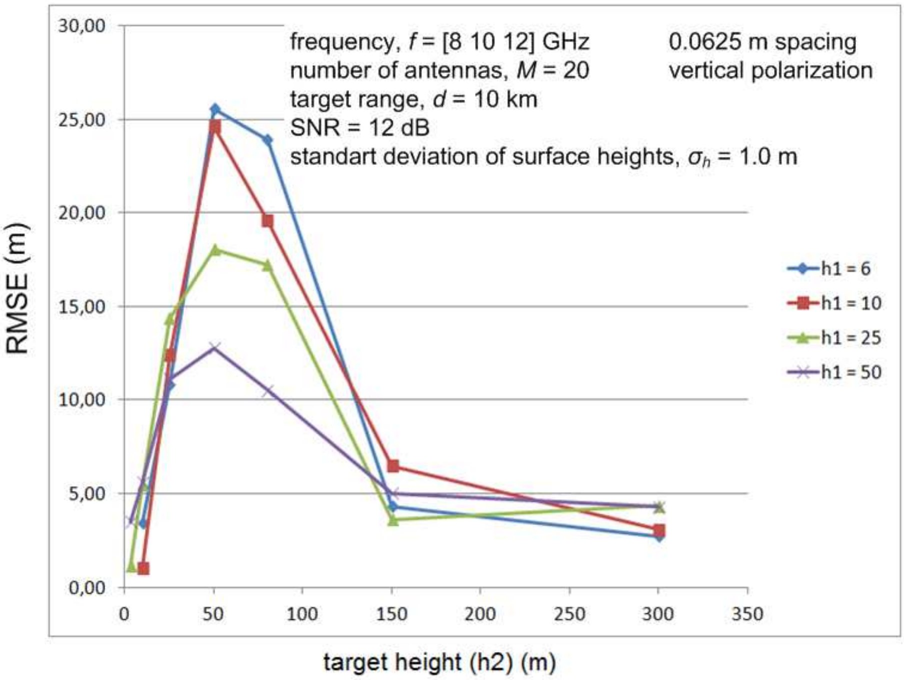

(a) RML algorithm

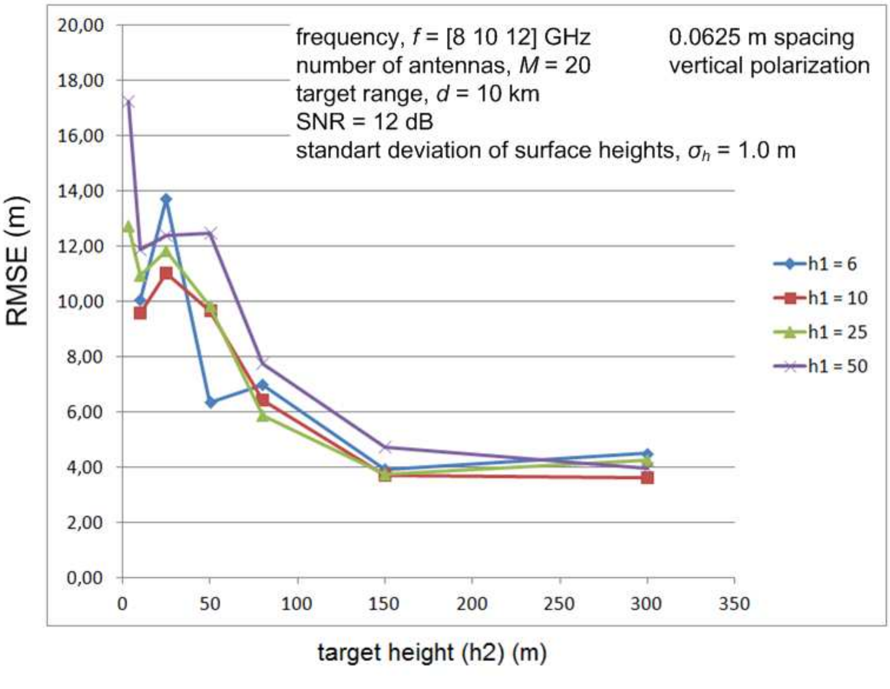

(b) RML-D algorithm

Figure 4.3: Target height vs RMSE at a range of d = 10 km a) RML and b) RML-D

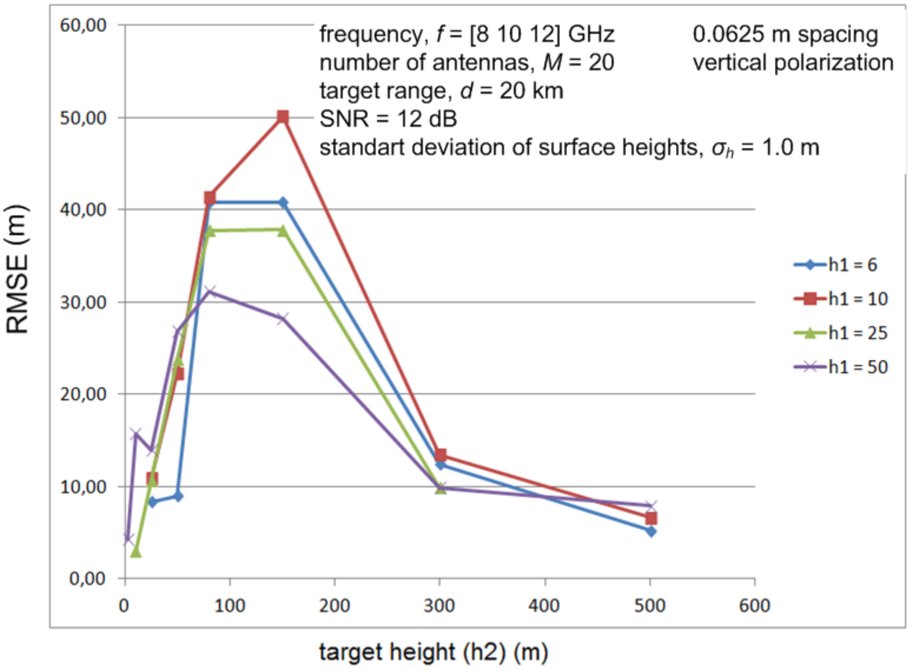

(a) RML algorithm

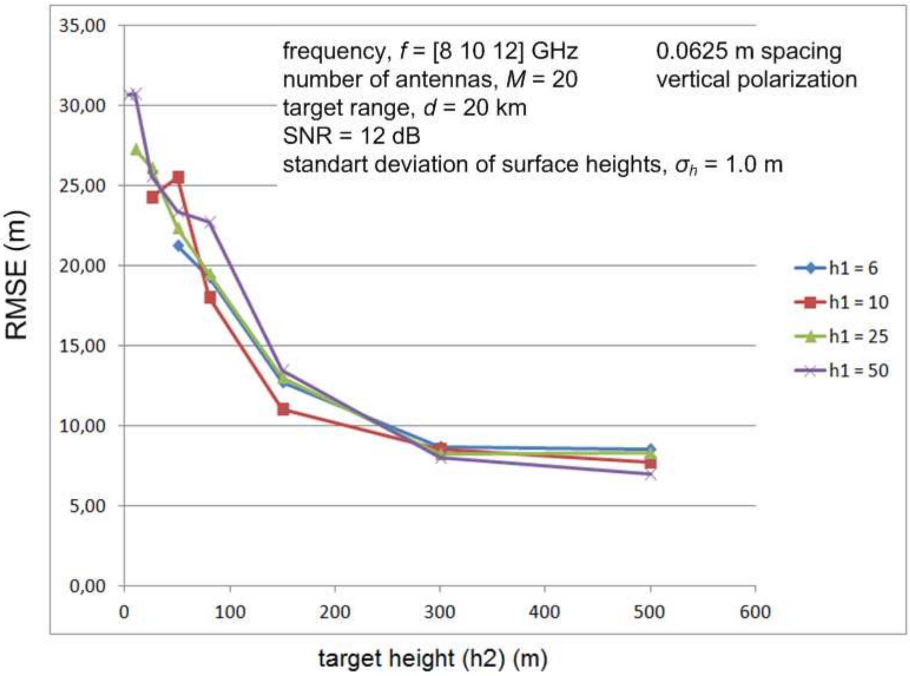

(b) RML-D algorithm

Figure 4.4: Target height vs RMSE at a range of d = 20 km a) RML and b) RML-D

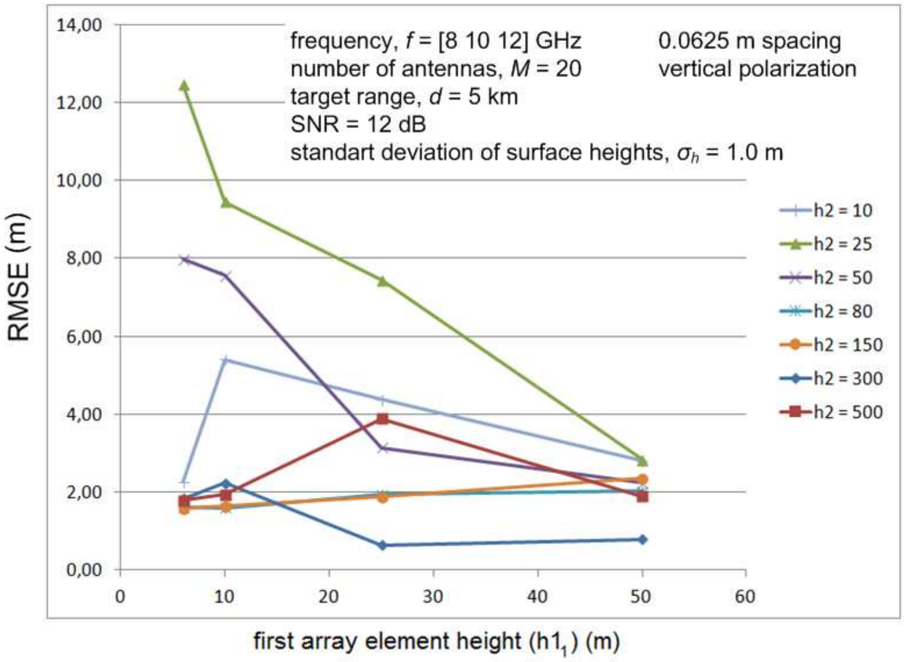

(a) RML algorithm

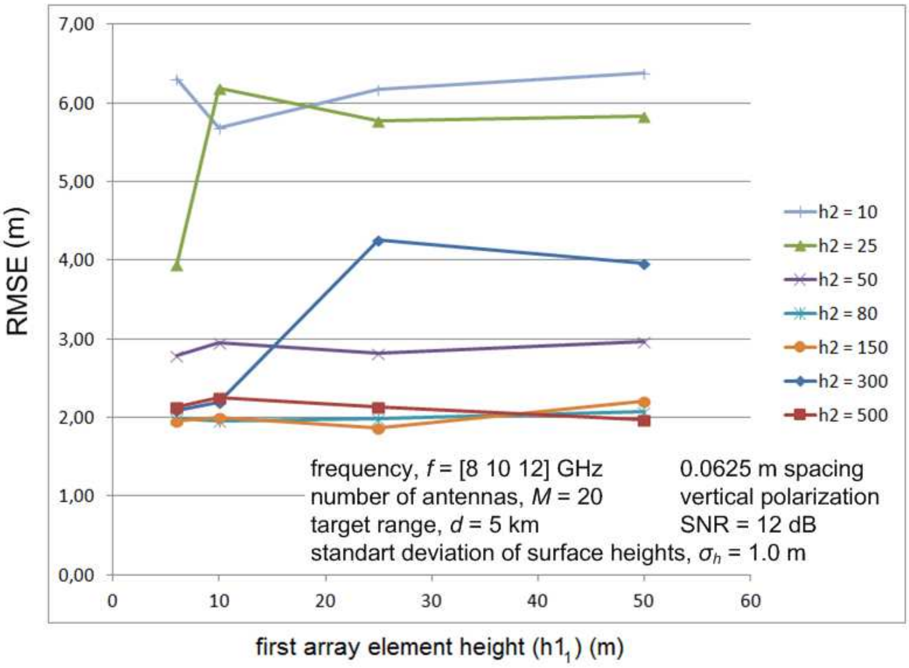

(b) RML-D

Figure 4.5: Antenna height vs RMSE at a range of d = 5 km a) RML and b) RML-D

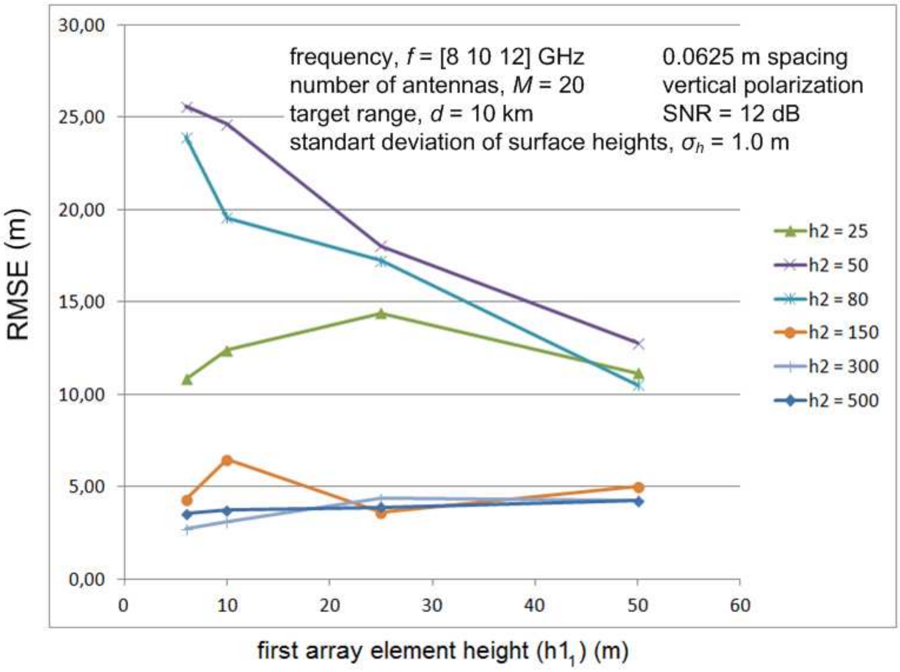

(a) RML algorithm

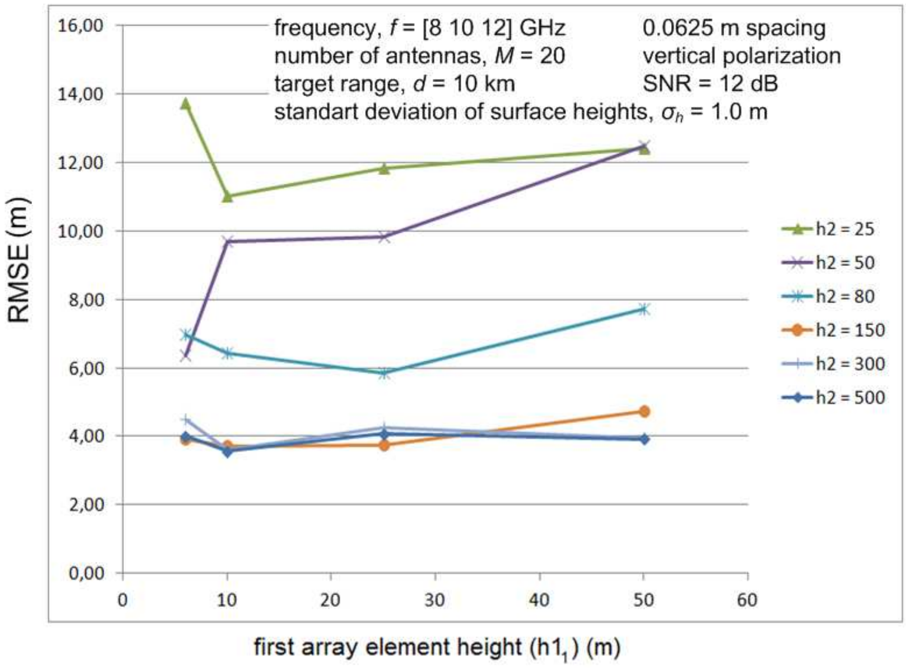

(b) RML-D algorithm

Figure 4.6: Antenna height vs RMSE at a range of d = 10 km a) RML and b) RML-D

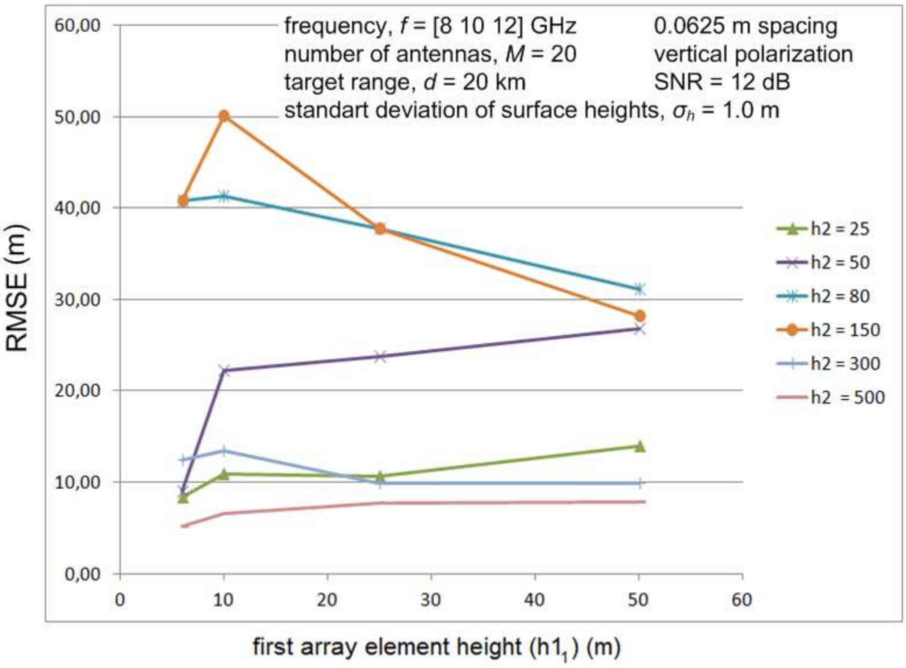

(a) RML algorithm

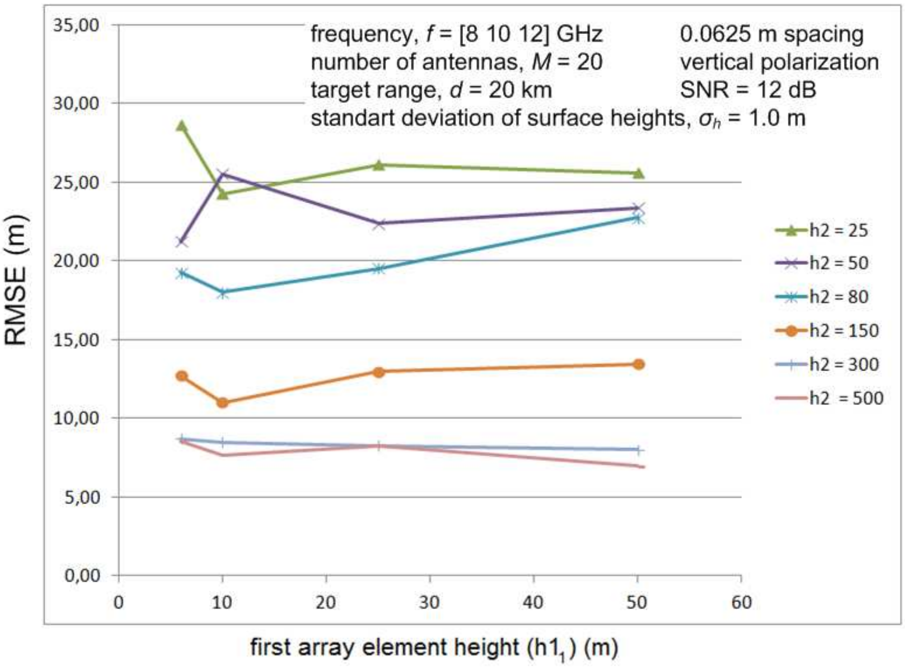

(b) RML-D algorithm

Figure 4.7: Antenna height vs RMSE at a range of d = 20 km a) RML and b) RML-D

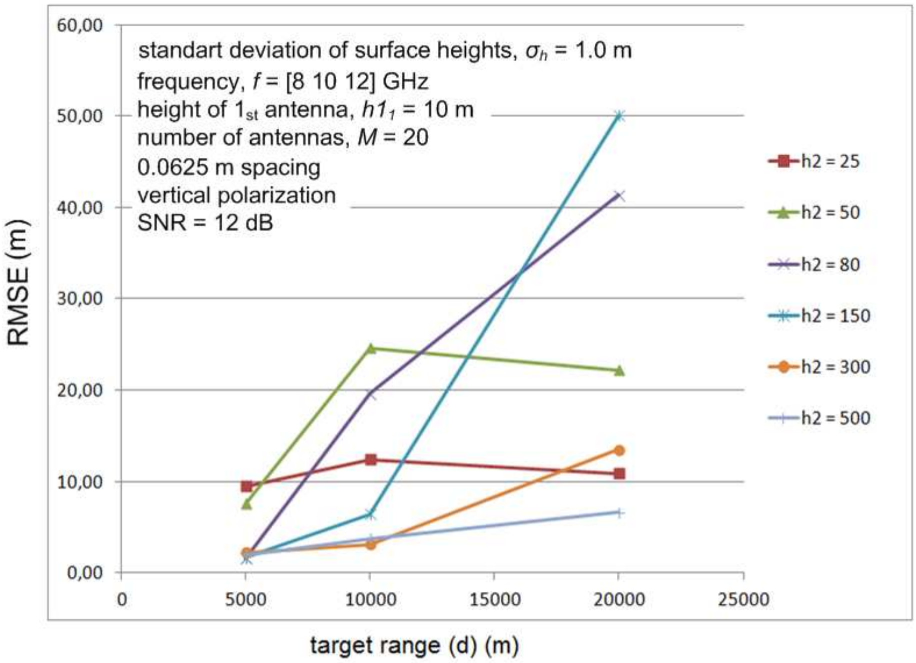

(a) RML algorithm

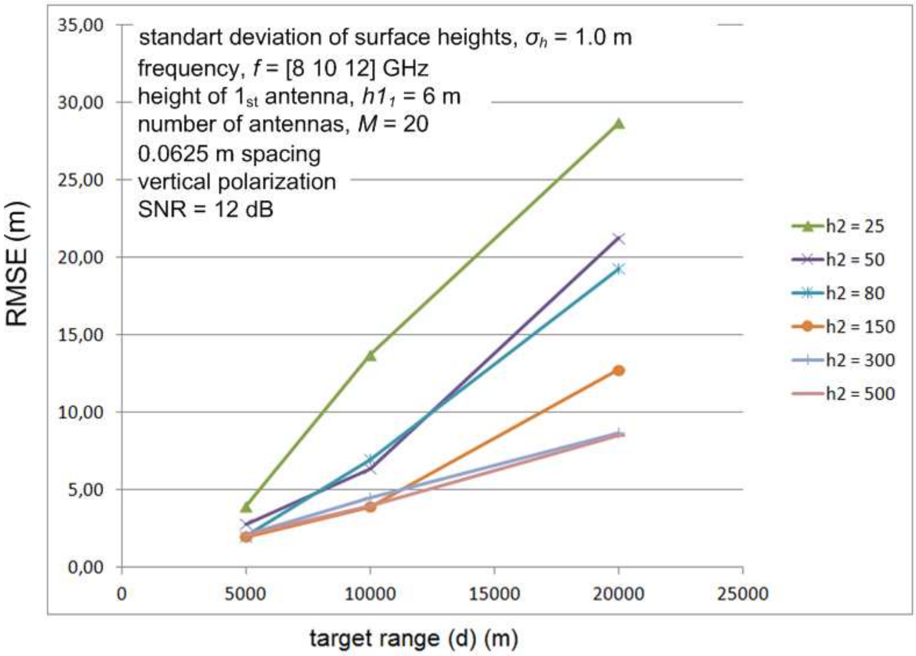

(b) RML-D algorithm

Figure 4.8: Target range vs RMSE when $h1_1 = 6$ m a) RML and b) RML-D

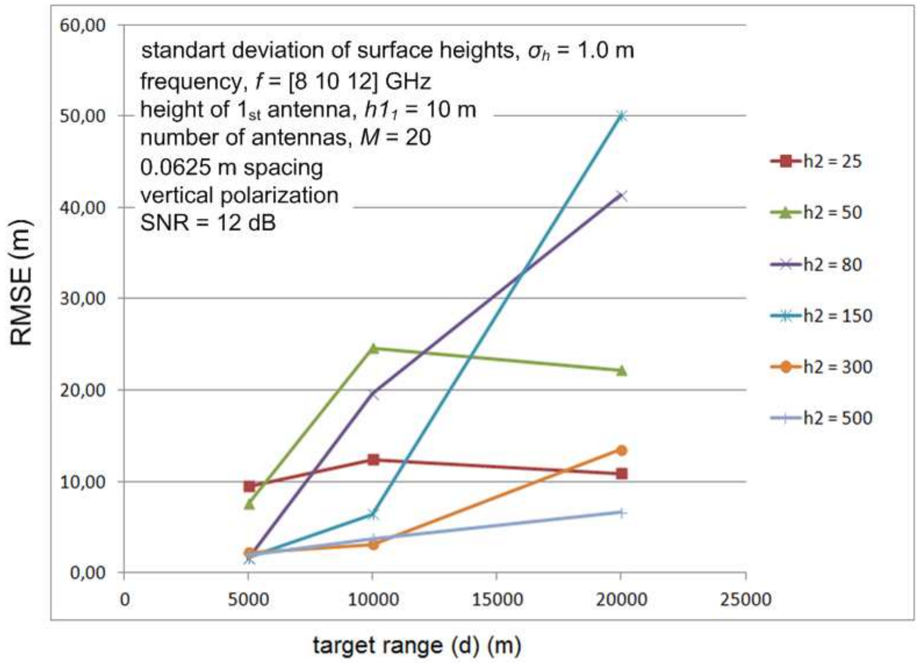

(a) RML algorithm

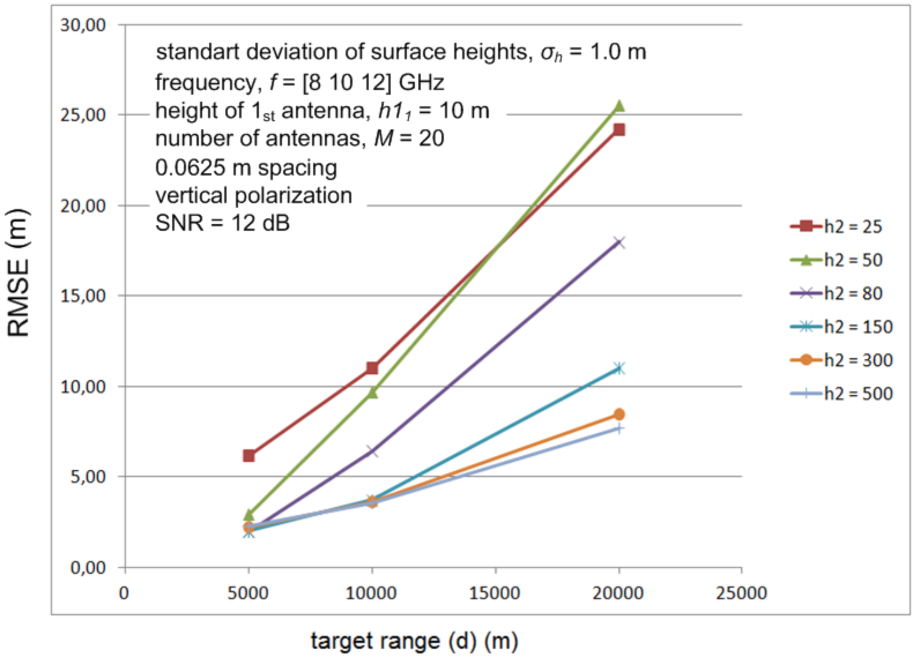

(b) RML-D algorithm

Figure 4.9: Target range vs RMSE when $h1_1$ = 10 m a) RML and b) RML-D

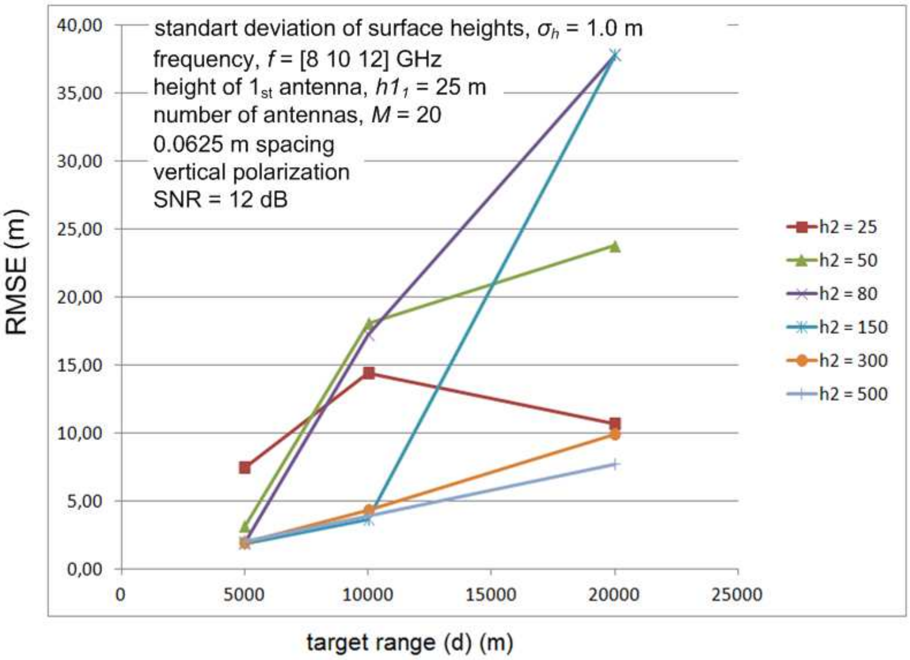

(a) RML algorithm

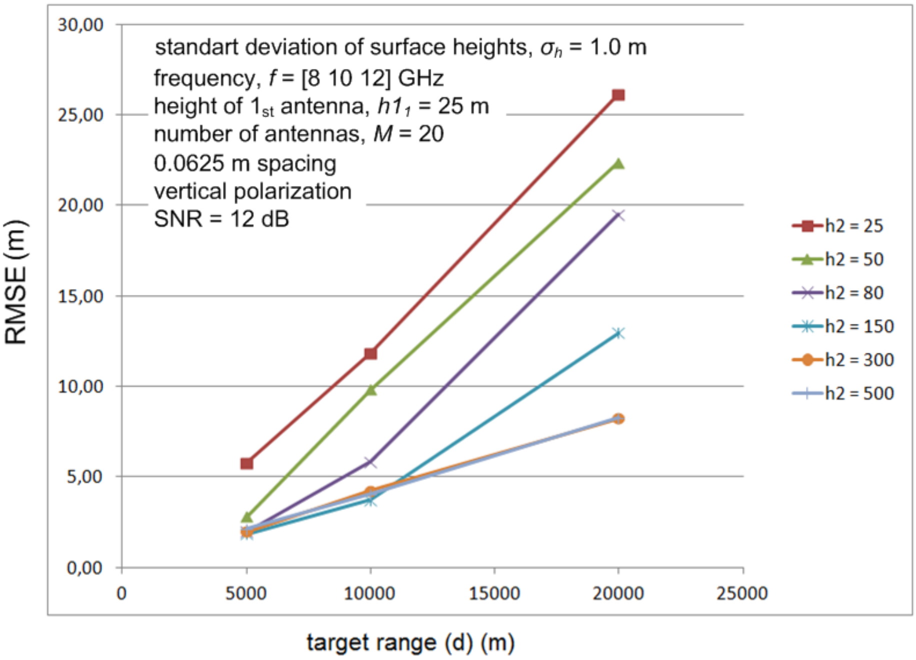

(b) RML-D algorithm

Figure 4.10: Target range vs RMSE when $h1_1$ = 25 m a) RML and b) RML-D

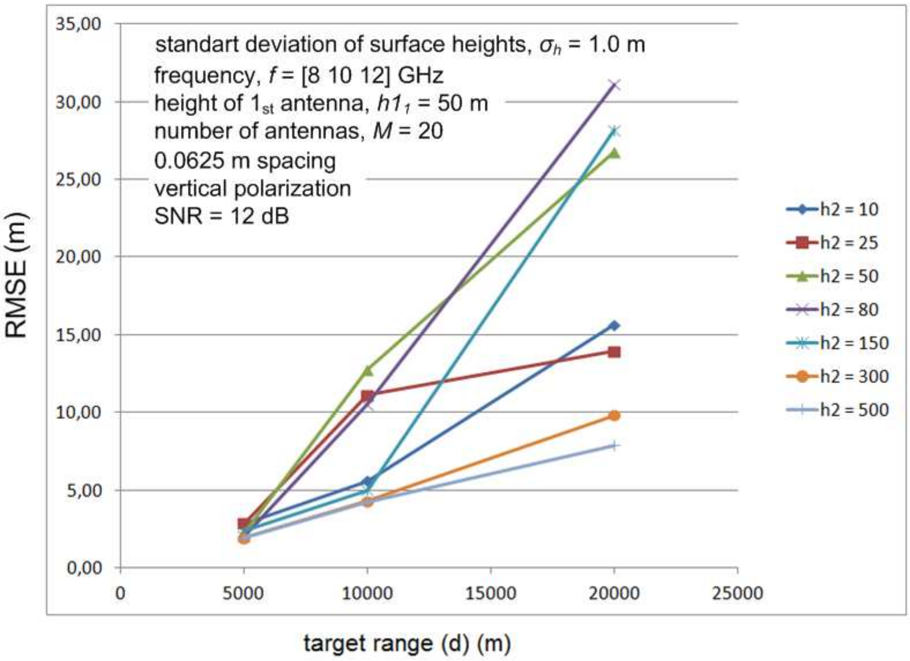

(a) RML algorithm

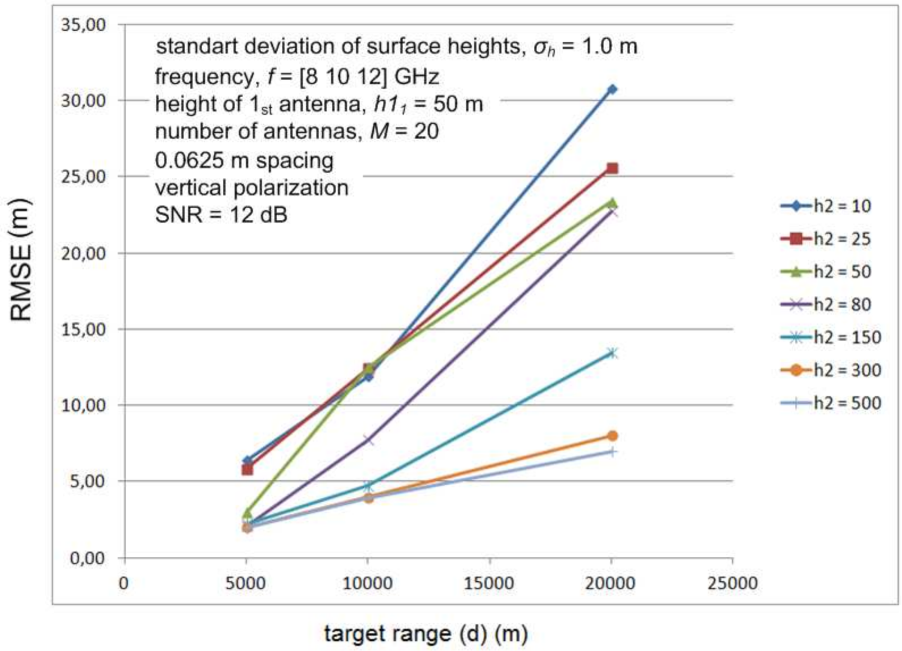

(b) RML-D algorithm

Figure 4.11: Target range vs RMSE when $h1_1$ = 50 m a) RML and b) RML-D

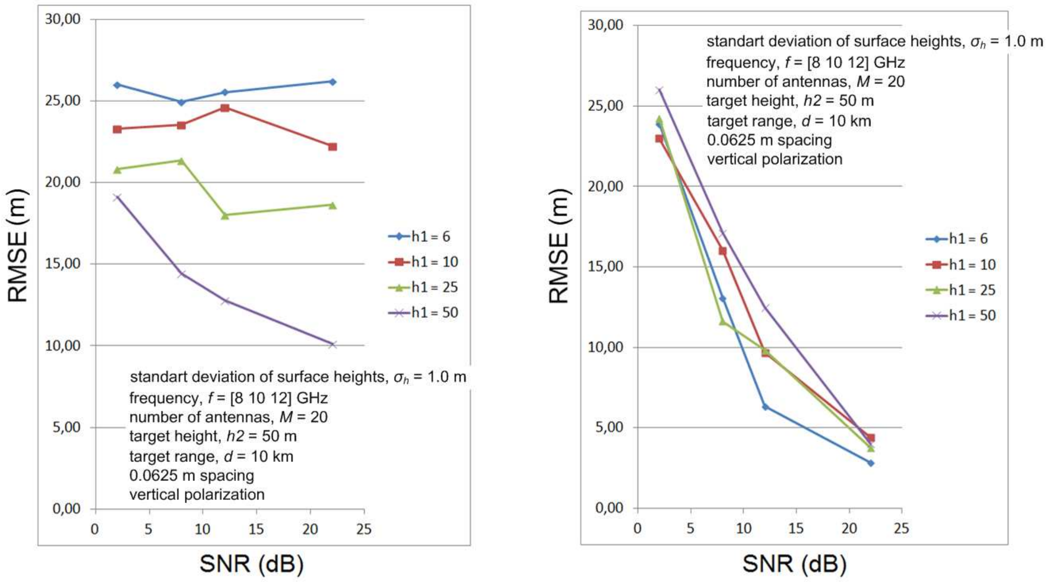

(a) RML algorithm

(b) RML-D algorithm

Figure 4.12: SNR vs RMSE when d = 10 km and $h2$ = 50 m a) RML and b) RML-D

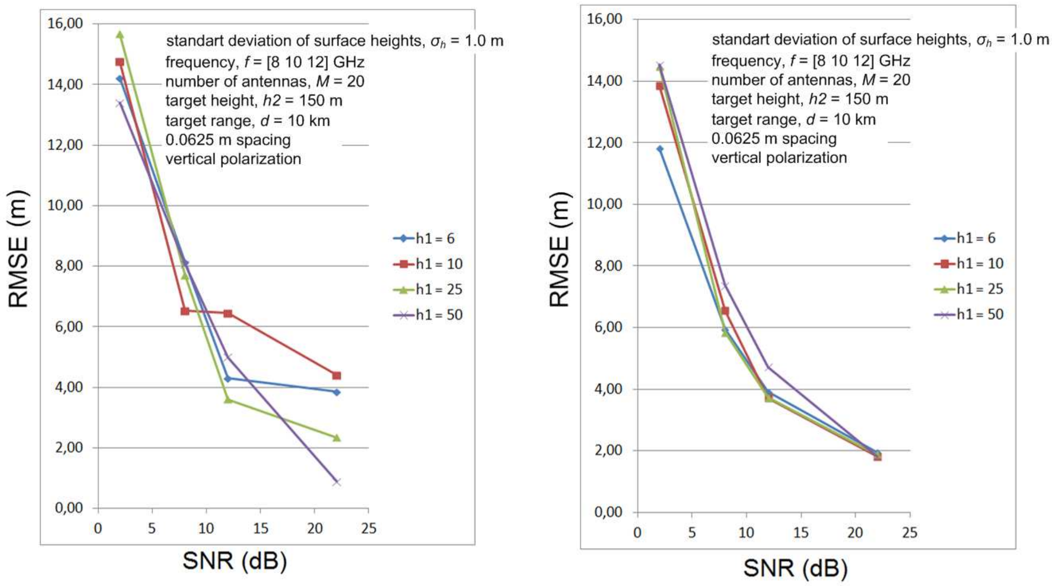

(a) RML algorithm

(b) RML-D algorithm

Figure 4.13: SNR vs RMSE when d = 10 km and $h2$ = 150 m a) RML and b) RML-D

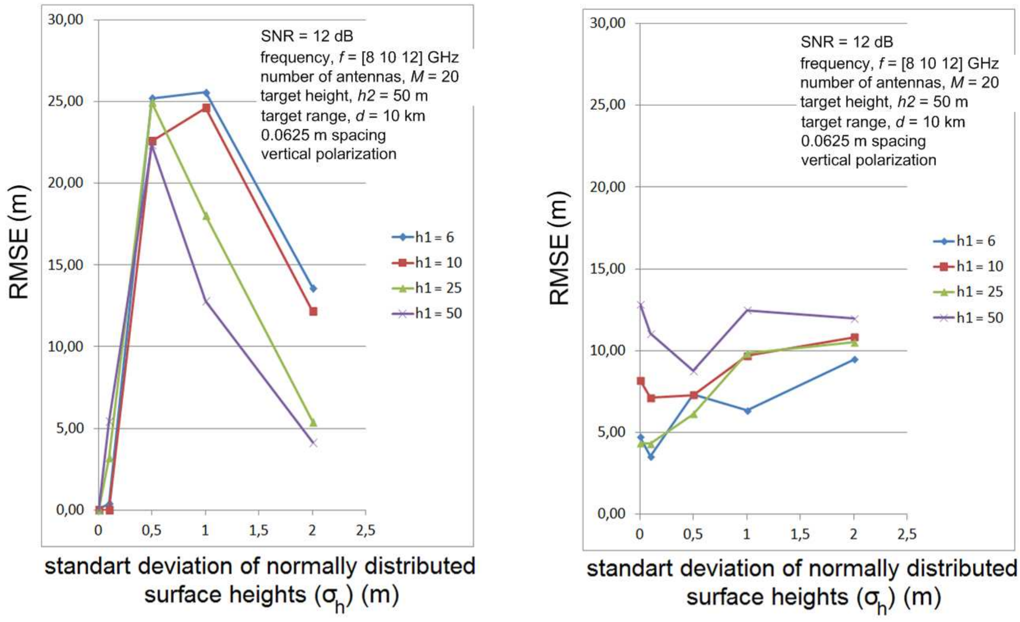

(a) RML algorithm

(b) RML-D algorithm

Figure 4.14: Standard deviation of normally distributed surface heights vs RMSE when d = 10 km and $h2$ = 50 m a) RML and b) RML-D

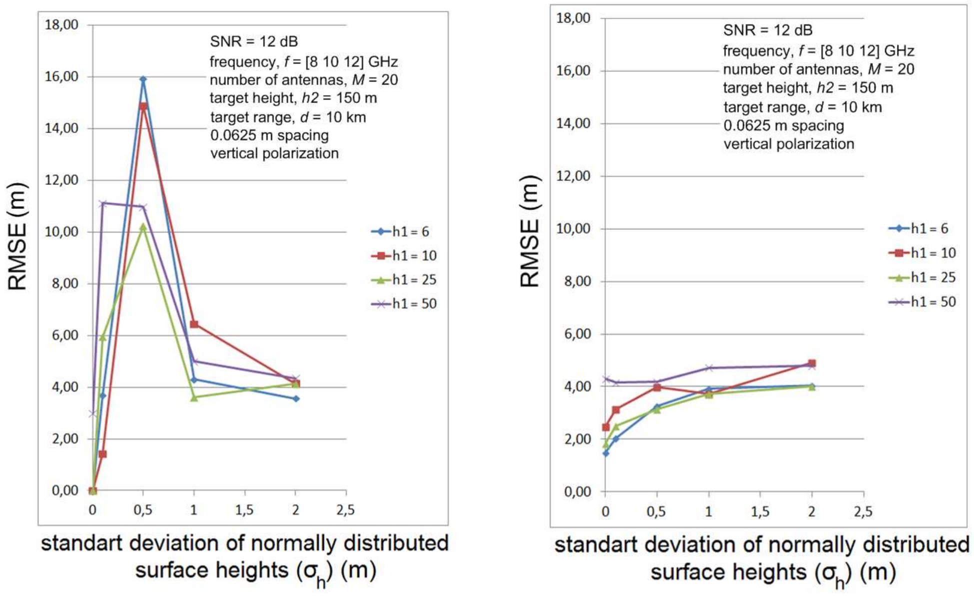

(a) RML algorithm

(b) RML-D algorithm

Figure 4.15: Standard deviation of normally distributed surface heights vs RMSE when d = 10 km and $h2$ = 150 m a) RML and b) RML-D

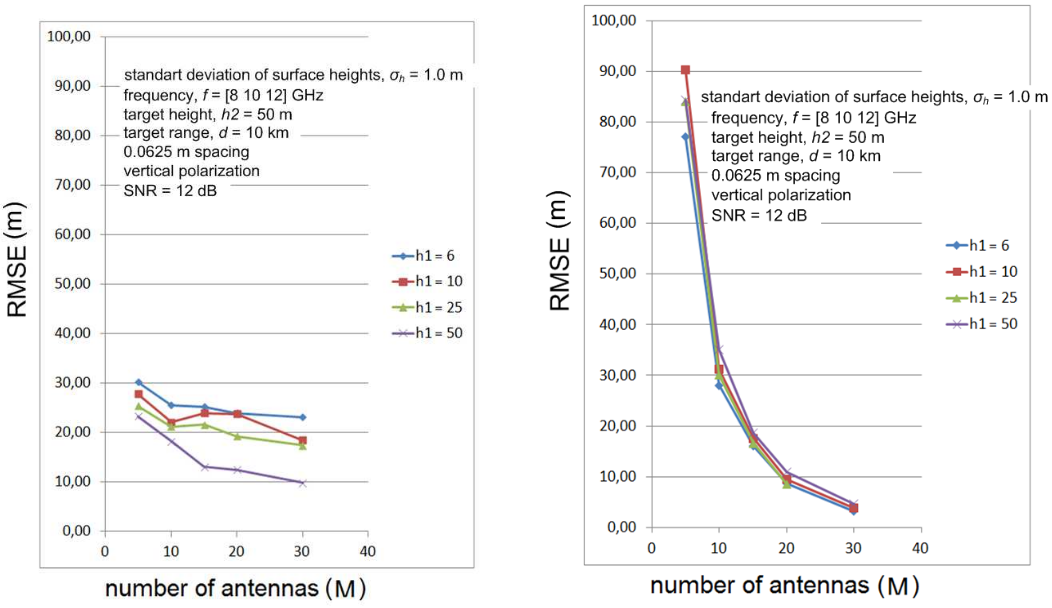

(a) RML algorithm

(b) RML-D algorithm

Figure 4.16: Number of antennas vs RMSE when d = 10 km and $h2$ = 50 m a) RML and b) RML-D

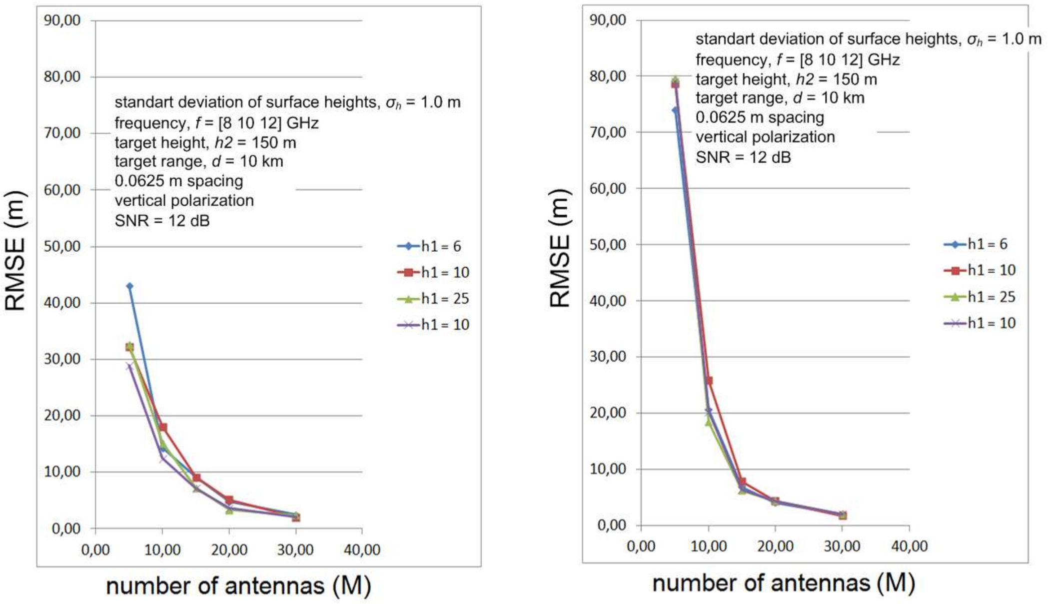

(a) RML algorithm

(b) RML-D algorithm

Figure 4.17: Number of antennas vs RMSE when d = 10 km and $h2$ = 150 m a) RML and b) RML-D

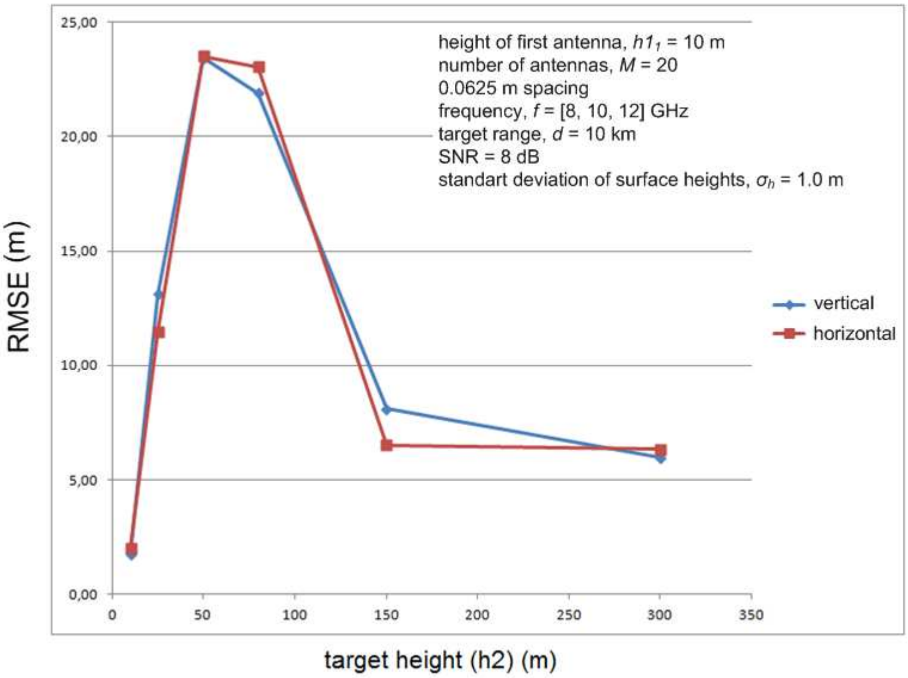

(a) RML algorithm

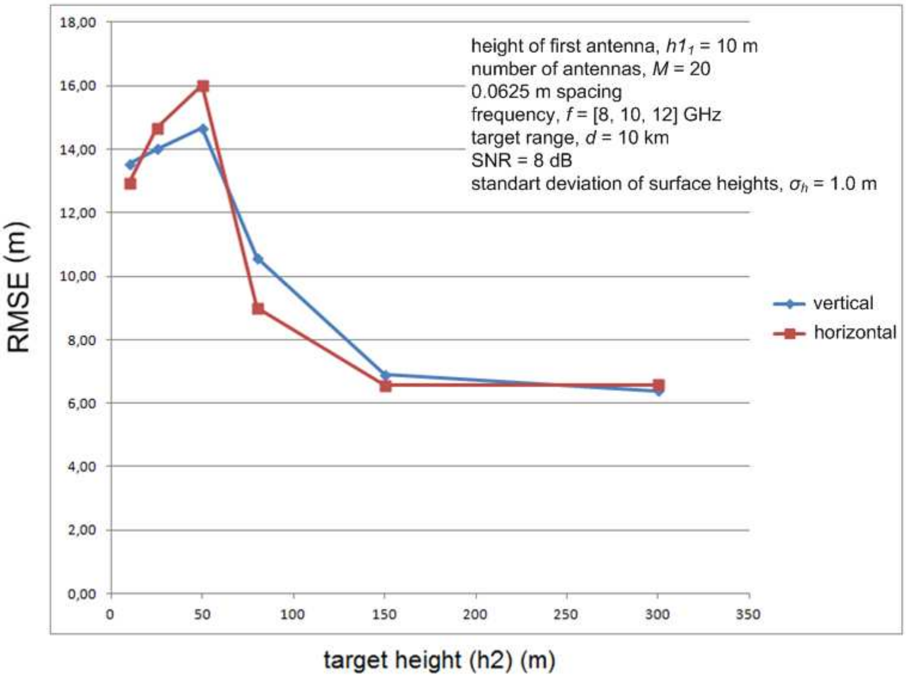

(b) RML-D algorithm

Figure 4.18: Target height vs RMSE for both vertical and horizontal polarization a) RML and b) RML-D

CHAPTER 5

CONCLUSIONS

In target detection, we aimed to increase SNR by diversity combining to hinder missed detection due to fading caused by surface reflection. Maximum Ratio Combining (MRC) is optimal in terms of SNR, however, it can not be applied to our problem since the target height is unknown. We proposed a combiner whose weights are found by maximizing the average value of SNR over target height values. We compared the proposed combining technique with MRC via simulations. It is observed that the gain in SNR that the proposed method provides is generally very close to that of MRC. However, the deviation of our combiner from MRC in terms of the gain in the SNR increases in some scenarios and may even reach to 10-15 dB. However, we can control the deviation amount from the optimum MRC method by providing sufficiently narrow elevation angle intervals. For example, in order to have a maximum 1 dB deviation at 5 km range, the height intervals can be chosen as [40-280], [280-520], [520-760] and [760-1000].

For height estimation, RML algorithm works well at very low altitudes where diffuse scattering is not strong. However, RMSE of RML algorithm shows peak where the diffuse scattering is felt significantly. This is what we expected since RML algorithm does not include the diffuse reflection while calculating its likelihood function. On the other hand, proposed RML-D algorithm succeeds to suppress the errors caused by the diffuse scattering. However, RMSE of RML-D algorithm peaks at very low altitudes where RML algorithm works well since diffuse reflection coefficient estimation algorithm of RML-D algorithm performs poorly at these very low altitudes.

It is seen that RMSE of both algorithms increase with increasing target range since the reflections become more comparable with the direct wave and angular resolution demand is obviously higher for higher ranges. It is also observed that although the increase in antenna height decreases the error caused by the diffuse scattering in RML algorithm, RML-D algorithm generally exhibits less errors than RML algorithm even if the antenna height is increased to 50 m.

When SNR is increased, the error of RML algorithm due to diffuse scattering decreases partly for the antenna height of 50 m. However, for the antenna heights below 25 m, the RMSE of the RML algorithm remains nearly constant. In contrast to RML algorithm, the performance of RML-D algorithm gets better as SNR increases. The errors due to poor performance of diffuse reflection coefficient estimation algorithm of RML-D decreases as the SNR increases.

The effect of the standard deviation of normally distributed surface heights, σ_h, on both algorithms has also been investigated. It is seen that RML algorithm is not robust to σ_h variation, as expected, since the diffuse scattering is controlled by the roughness factor which is a function of σ_h. However, RML-D algorithm is quite robust to changes in σ_h.

When the number of antennas is increased, the error of RML algorithm due to diffuse scattering decreases partly for the antenna height of 50 m. However, for the antenna heights below 25 m, RMSE of RML algorithm is nearly constant. RML-D algorithm shows higher errors compared to RML algorithm for the number of antennas below 15 due to the diffuse reflection coefficient estimation algorithm. However, for the number of antennas of 20 or above, RML-D algorithm outperforms RML algorithm.

It is also observed that the performances of both algorithms are nearly independent of antenna polarization.

We propose the following topics for future research on this subject:

- The frequency diversity can be utilized in target detection to improve the performance further.
- MAP formulation, instead of ML, can improve the performance of RML-D algorithm especially for very low target heights.
- The radar architecture can be extended to MIMO radar architecture.
- The target RCS fluctuations can be included in the multipath model.

REFERENCES

[1] M. L. Meeks, "*Radar Propagation at Low Altitudes*", Dedham, MA: Artech House, 1982.

[2] M. I. Skolnik, "*Radar Handbook*", 3rd Ed., New York: McGraw-Hill, 2008.

[3] W. S. Ament, "Toward a Theory of Reflection by a Rough Surface", *Proceedings of the IRE,* On page(s): 142-146, Volume: 41 Issue: 1, Jan. 1953.

[4] C. I. Beard, "Coherent and Incoherent Scattering of Microwaves from the Ocean", *Antennas and Propagation, IRE Transactions on,* On page(s): 470-483, Volume: 9 Issue: 5, 1961.

[5] P. Beckmann, A. Spizzichino, "*The Scattering of Electromagnetic Waves from Rough Surfaces*", New York: Pergamon, 1963.

[6] D. K. Barton, "Low-Angle Radar Tracking", *Proceedings of the IEEE,* On page(s): 687-704, Volume: 62 Issue: 6, 1974.

[7] D. K. Barton, "Forward Scatter at Low Grazing Angles", *Conf. Rec., Radar '77,* London, Oct. 25-28, 1977, IEE Conf. Publ. 155, pp. 308-312.

[8] A. V. Mrstik, P. G. Smith, "Multipath Limitations on Low-Angle Radar Tracking", *Aerospace and Electronic Systems, IEEE Transactions on,* On page(s): 85-102, Volume: AES-14 Issue: 1, 1978.

[9] D. K. Barton, "Multipath Fluctuation Effects in Track-While-Scan Radar", *Aerospace and Electronic Systems, IEEE Transactions on,* On page(s): 754-764, Volume: AES-15 Issue: 6, 1979.

[10] A. R. Miller, R. M. Brown, "Geometric-Optics Theory for Coherent Scattering of Microwaves from the Ocean Surface", NRL Report 7705, 1974.

[11] A. R. Miller, R. M. Brown, E. Vegh, "New Derivation for the Rough Surface Reflection Coefficient and for the Distribution of Sea-Wave Elevations", *Microwaves, Optics and Antennas, IEE Proceedings H,* On page(s): 114-116, Volume: 131 Issue: 2, 1984.

[12] A. R. Miller, E. Vegh, "A Family of curves for the rough surface reflection coefficient", *Microwaves, Antennas and Propagation, IEE Proceedings H,* On page(s): 483-489, Volume: 133 Issue: 6, 1986.

[13] T. Griesser, C. A. Balanis, "Oceanic Low-Angle Monopulse Radar Tracking Errors", *Oceanic Engineering, IEEE Journal of,* On page(s): 289-295, Volume: 12 Issue: 1, 1987.

[14] S. Ahn, E. Yang, J. Chun, J. Kim, "Low Angle Tracking Using Iterative Multipath Cancellation in Sea Surface Environment", *Radar Conference, 2010 IEEE,* On page(s): 1156-1160, 2010.

[15] A. Ephrath, “Using Vertical and Horizantal Multipath Models in Radar Simulations”, *Microwave Conference, 2008. EuMC 2008. 38th European,* On page(s): 971-974, 2008.

[16] Y. Takabayahsi, T. Matsuzaki, H. Kameda, “Altitude Estimation Method Using Assumed Altitude Reliability Based on Multipath Propagation Model”, *SICE Annual Conference 2010, Proceedings of,* On page(s): 2196 - 2201, 2010.

[17] H. Xiao-qin ,C. Jian-wen, W. Yong-liang, “Use of a Multipath Model in the Meter-wave Radar Height Finding Applications”, *Aerospace Conference, 2008 IEEE,* On page(s): 1-7, 2008.

[18] L. C. Godara, “*Handbook of Antennas for Wireless Communications*”, CRC Press, 2002.

[19] D. G. Brennan, “Linear Diversity Combining Techniques”, *Proceedings of the IEEE,* On page(s): 331-356, Volume: 91 Issue: 2, 2003.

[20] J. H. Zhao, J. Y. Yang, “Frequency Diversity to Low-Angle Detecting Using a Highly Deterministic Multipath Signal Model”, *Radar, 2006. CIE ’06. International Conference on,* On page(s): 1-5, 2006.

[21] J. G. Teti, Jr, “Wide-Band Airborne Radar Operating Considerations for Low-Altitude Surveillance in the Presence of Specular Multipath”, *Antennas and Propagation, IEEE Transactions on,* On page(s): 176-191, Volume: 48 Issue: 2, 2000.

[22] T. Inaba, K. Araki, “Space-Frequency Maximal Ratio Combining for Low-Elevation Radar Target”, *Electronics and Communications in Japan,* Volume: 87 , 2004.

[23] S. Ayaslı, “SEKE: A Computer Model for Low Altitude Radar Propagation Over Irregular Terrain”, *Antennas and Propagation, IEEE Transactions on,* On page(s): 1013-1023, Volume: 34 Issue: 8, 1986.

[24] A. Sinha, Y. B. Shalom, W. D. Blair, T. Kirubarajan, “Radar Measurement Extraction in the Presence of Sea-Surface Multipath”, *Aerospace and Electronic Systems, IEEE Transactions on,* On page(s): 550-567, Volume: 39 Issue: 2, 2003.

[25] R. Takahashi, K. Hirata, H. Maniwa, “Altitude Estimation of Low Elevation Target over the Sea for Surface Based Phased Array Radar”, *Radar Conference, 2010 IEEE,* Page(s): On page(s): 123-128, 2010.

[26] E. Bosse, R. M. Turner, E. S. Riseborough, “Model-Based Multifrequency Array Signal Processing for Low-Angle Tracking”, *Aerospace and Electronic Systems, IEEE Transactions on,* On page(s): 194-210, Volume: 31 Issue: 1, 1995.

[27] E. Bosse, R. M. Turner, M. Lecours, “Tracking Swerling Fluctuating Targets at Low Altitude over the Sea”, *Aerospace and Electronic Systems, IEEE Transactions on,* On page(s): 806-822, Volume: 27 Issue: 5, 1991.

[28] E. Bosse, R. M. Turner, “Height Ambiguities in Maximum Likelihood Estimation with a Multipath Propagation Model”, *Signals, Systems and Computers, 1988. Twenty-Second Asilomar Conference on*, On page(s): 690-695, Volume: 2, 1988.

[29] E. Bosse, R. M. Turner, D. Brookes, “Improved Radar Tracking Using a Multipath Model: Maximum Likelihood Compared with Eigenvector Analysis”, *Radar, Sonar and Navigation, IEE Proceedings,* On page(s): 213-222, Volume: 141 Issue: 4, 1994.

[30] M. Djeddou, A. Belouchrani, S. Aouada, “Maximum Likelihood Angle-Frequency Estimation in Partially Known Correlated Noise for Low-Elevation Targets”, *Signal Processing, IEEE Transactions on,* On page(s): 3057 - 3064, Volume: 53 Issue: 8, 2005.

[31] T. Lo, J. Litva, “Use of a Highly Deterministic Multipath Signal Model in Low-Angle Tracking”, *Radar and Signal Processing, IEE Proceedings F,* On page(s): 163-171, Volume: 138 Issue: 2, 1991.

[32] A. A. Ksienski, R. B. McGhee, “A Decision Theoretic Approach to the Angular Resolution and Parameter Estimation Problem for Multiple Targets”, *Aerospace and Electronic Systems, IEEE Transactions on,* On page(s): 443-455, Volume: AES-4 Issue: 3, 1968.

[33] J. E. Howard, “A Low Angle Tracking System for Fire Control Radars”, *Proceedings IEEE International Conference on Radar,* On page(s): 412-417, 1975.

[34] S. Haykin, J. P. Reilly, “Maximum Likelihood Receiver for Low-Angle Tracking Radar, Part 1: The Symmetric Case”, *Communications, Radar and Signal Processing, IEE Proceedings F,* On page(s): 261-272, Volume: 129 Issue: 4, 1982.

[35] J. P. Reilly, S. Haykin, “Maximum Likelihood Receiver for Low-Angle Tracking Radar, Part 2: The Nonsymmetric Case”, *Communications, Radar and Signal Processing, IEE Proceedings F,* On page(s): 331-340, Volume: 129 Issue: 5, 1982.

[36] J. P. Reilly,, “Nonlinear Array Processing Techniques with Applications to Correlated Multipath”, Ph.D. dissertation, McMaster University, Hamilton, Ontario, March 1981.

[37] W. Ballance, A. G. Jaffer, “Low-Angle Direction Finding Based on Maximum Likelihood: An Unification”, *Presented at the 21st Asilomar Conference on Signals, Systems and Computers,* Pacific Grove, CA, Nov. 1987.

[38] White, W. D., “Low-Angle Radar Tracking in the Presence of Multipath”, *Aerospace and Electronic Systems, IEEE Transactions on,* On page(s): 835-852, Volume: AES-10 Issue: 6, 1974.

[39] Sherman, S. M., “Complex Indicated Angles Applied to Unresolved Radar Targets and Multipath”, *Aerospace and Electronic Systems, IEEE Transactions on,* On page(s): 160-170, Volume: AES-7 Issue: 1, 1971.

[40] R. O. Schmidt, “Multiple Emitter Location and Signal Parameter Estimation”, *Antennas and Propagation, IEEE Transactions on,* On page(s): 276-280, Volume: 34 Issue: 3, 1986.

APPENDIX A

BOUNDRIES OF ML FUNCTIONS IN SEC. 4.1 AND SEC. 4.2

The Cauchy-Schwarz inequality states that for all vectors $\mathbf{x} \in C^{Mx1}$ and $\mathbf{y} \in C^{Mx1}$,

$$\left\|\mathbf{x}^H \mathbf{y}\right\|^2 \leq \|\mathbf{x}\|^2 \ \|\mathbf{y}\|^2 . \tag{A.1}$$

Let $(\mathbf{x_1}, \mathbf{x_2}, ..., \mathbf{x_P}) \in C^{Mx1}$, $(\mathbf{y_1}, \mathbf{y_2}, ..., \mathbf{y_P}) \in C^{Mx1}$ and $(z_1^2, z_2^2, ..., z_P^2) \in R^{+,\ 1x1}$ be given and P is a positive integer. Then,

$$\begin{aligned}
\frac{1}{\sum_{p=1}^{P} \left\|\mathbf{x}_p\right\|^2 / z_p^2} \sum_{p=1}^{P} \frac{\left\|\mathbf{x}_p^H \mathbf{y}_p\right\|^2}{z_p^2 \left\|\mathbf{y}_p\right\|^2} &= \frac{1}{\sum_{p=1}^{P} \left\|\mathbf{x}_p\right\|^2 / z_p^2} \sum_{p=1}^{P} \frac{\left\|\mathbf{x}_p\right\|^2}{z_p^2} \frac{\left\|\mathbf{x}_p^H \mathbf{y}_p\right\|^2}{\left\|\mathbf{x}_p\right\|^2 \left\|\mathbf{y}_p\right\|^2} \\
&\leq \frac{1}{\sum_{p=1}^{P} \left\|\mathbf{x}_p\right\|^2 / z_p^2} \sum_{p=1}^{P} \frac{\left\|\mathbf{x}_p\right\|^2}{z_p^2} \\
&= 1, \qquad (A.2)
\end{aligned}$$

since

$$\frac{\left\|\mathbf{x}_p^H \mathbf{y}_p\right\|^2}{\left\|\mathbf{x}_p\right\|^2 \left\|\mathbf{y}_p\right\|^2} \leq 1, \tag{A.3}$$

from the Cauchy-Schwarz inequality in Eq. A.1.

It is also obvious that

$$\frac{1}{\sum_{p=1}^{P} \left\|\mathbf{x}_p\right\|^2 / z_p^2} \sum_{p=1}^{P} \frac{\left\|\mathbf{x}_p^H \mathbf{y}_p\right\|^2}{z_p^2 \left\|\mathbf{y}_p\right\|^2} \geq 0, \tag{A.4}$$

since the first multiplier is greater than zero and the second multiplier is greater than or equal to zero.

Then, if $\mathbf{x}$ is replaced by $\mathbf{s}$, $\mathbf{y}$ is replaced by $\mathbf{f}$(h2) and z is replaced by σ_n, then, it is demonstrated that

$$0 \leq \frac{1}{\sum_{p=1}^{P} \left\|\mathbf{s}_p\right\|^2 / \sigma_{n,p}^2} \sum_{p=1}^{P} \frac{\left\|\mathbf{s}_p^H \mathbf{f}_p(h2)\right\|^2}{\sigma_{n,p}^2 \left\|\mathbf{f}_p(h2)\right\|^2} \leq 1. \tag{A.5}$$

In addition, if $\mathbf{x}$ is replaced by $\mathbf{s}$, $\mathbf{y}$ is replaced by $(\mathbf{f}(\mathrm{h2}) + \rho_d\ \mathbf{g}(\mathrm{h2}))$ and z is replaced by σ_n, then, it is demonstrated that

$$0 \leq \frac{1}{\sum_{p=1}^{P} \left\|\mathbf{s}_p\right\|^2 / \sigma_{n,p}^2} \sum_{p=1}^{P} \frac{\left\|\mathbf{s}_p^H \left(\mathbf{f}_p(h2) + \rho_{d,p}\ \mathbf{g}_p(h2)\right)\right\|^2}{\sigma_{n,p}^2 \left\|\left(\mathbf{f}_p(h2) + \rho_{d,p}\ \mathbf{g}_p(h2)\right)\right\|^2} \leq 1. \tag{A.6}$$